

FASJS

Faculty of Arts and Science Journal of Science



SÜLEYMAN DEMİREL
UNİVERSİTY



Süleyman Demirel University
Faculty of Arts and Sciences
Journal of Science

Volume

19

Issue

2

Year

2024

e-ISSN

1306-7575

Journal Boards

Privilege Owner

Prof. Dr. Nevzat Özgü YİĞİT

Editor-in-Chief

Assoc. Prof. Dr. Raşit ÇALIŞKAN

Section Editors

Prof. Dr. Duygu ARUĞASLAN ÇİNÇİN Prof. Dr. Fatih UCUN Assoc. Prof. Dr. Raşit ÇALIŞKAN Prof. Dr. Melek ZEYBEK YÜNLÜ

Advisory Board

Prof. Dr. Abdullah AYDIN

Prof. Dr. Alexander VASİN

Prof. Dr. Bayram ŞAHİN

Prof. Dr. Ekrem SAVAŞ

Prof. Dr. Gerhard WEBER

Prof. Dr. İzzet ŞENER

Prof. Dr. Nazan ÜZÜM

Prof. Dr. Mohamed BELGAID

Prof. Dr. Orhan KARABULUT

Prof. Dr. Oscar J. GARAY

Prof. Dr. Selma ÖZÇAĞ

Prof. Dr. Yogesh Chandra SHARMA

Prof. Dr. Hasan GENÇ

Prof. Dr. Özgür EMİROĞLU

Dr. Diogo PINHEIRO

Dr. Anna FARKAS

Dr. Julia Puseletso MOFOKENG

Dr. Zohra BEN SALEM

Technical Editors

Prof. Dr. Rağbet Ezgi DURAN

Assist. Prof. Dr. Mehmet Akif YETİM

Layout Editors

Assoc. Prof. Dr. Durmuş Ali ALDEMİR

Assist. Prof. Dr. Nurullah YILMAZ

Assist. Prof. Dr. Kader POTURCU

Assist. Prof. Dr. Zekiye ÇİLOĞLU ŞAHİN

Res Asst. Dr. İsmail ERKAYA

Res Asst. Dr. Yunus Emre BÜLBÜL

Res Asst. Özgecan TIRYAKI

Res Asst. Yiğit ANTEPLİOĞLU

Res Asst. Elif MUSLU

Res Asst. Saime KOLANCI

Language Editors

Assist. Prof. Dr. Ali Osman YALKIN

Assist. Prof. Dr. Yeşim Sultan AKBAY

Süleyman Demirel University Faculty of Arts and Science Journal of Science is a peer-reviewed scientific journal published semi-annually, in May and November.

Original scientific research articles submitted in English in the fields of Biology, Physics, Chemistry and Mathematics are continued in the scientific review process after the preliminary evaluation stage, where similarity and layout checks are made.

No fee is charged from the author or institution under any name.

Special numbers/issues can be published without changing the periodic publication frequency during the year.

Since 2017; technical notes, letters to the editor, discussions, case reports and reviews are not accepted.

As of 01.01.2023, Süleyman Demirel University Faculty of Arts and Sciences Journal of Science only accepts studies submitted in English.

Süleyman Demirel University Faculty of Arts and Science Journal of Science (SDUFASJS) takes into account the principles published by the Higher Education Institutions Scientific Research and Publication Ethics Directive and “Committee on Publication Ethics” (COPE). In this context, the issues that are important for the authors, referees and editors are specified in the “Ethical Principles and Publication Policy” page of the journal website.

Süleyman Demirel University Faculty of Arts and Science Journal of Science is indexed in the following databases.

- ULAKBIM TR – Dizin
- Bielefeld Academic Search Engine (BASE)
- Centre for Agriculture and Bioscience International (CABI) - CAB Direct
- China National Knowledge Infrastructure (CNKI)
- Crossref
- Directory of Open Access Journals (DOAJ)
- Directory of Open Access Scholarly Resources (ROAD)
- EBSCO host
- Elektronische Zeitschriftenbibliothek (EZB)
- German Union Catalogue of Serials (ZDB)
- Google Academic
- Index Copernicus
- Information Matrix for the Analysis of Journals (MIAR)
- MathSciNet
- ResearchBib
- WorldCat

CONTENTS

Further Results on (A_s^j, f)-Lacunary Statistical Convergence of Double Sequences of order α	86
Ömer Kişi, Rümeyza Akbıyık, Mehmet Gürdal	
Genotoxicity and Oxidative Stress of Water Concentrates from Recreation Pools After Various Disinfection Methods	98
Zafer Bektaş, Melda Şahin, Vehbi Atahan Toğay, Uğur Şahin, Mustafa Calapoğlu	
Investigation of the Structural, Morphological, and Optical Properties of ZnBr₂-Added MAPbI₃ Perovskite Thin Films	108
Havva Elif Lapa	
Effectiveness of a Novel CTGF LNA GapmeR Sequence in Gastric Cancer Cells	117
Deniz Sezlev Bilecen	
Electric Field Responsive Smart Fluids from Olive Pulp Powder	127
Özlem Erol	
Experimental and Theoretical Monitoring of the Adsorption of 2,4-Dimethylphenol on <i>Coturnix Japonica</i> Eggshell	144
Belgin Tunalı, Deniz Türköz Altuğ, Taner Kalaycı, Neslihan Kaya Kınaytürk	
Cytogenetic and Morphophysiological Effects of Exogenous Triacantanol against Drought in Barley	161
Selma Tabur, Serkan Özmen, Ahmet Yiğit	
Energy Loss and Range Calculations for Alpha Particles in B-100 Bone and C-552 Air-Equivalent Plastic Materials	175
Metin Usta	

Further Results on (Δ_s^j, f) -Lacunary Statistical Convergence of Double Sequences of order α

Ömer Kişi¹, Rümeysa Akbıyık², Mehmet Gürdal^{3,*}

¹Department of Mathematics, Faculty of Science, Bartın University, 74100, Bartın, TURKEY

<https://orcid.org/0000-0001-6844-3092>

² Department of Mathematics, Faculty of Science, Bartın University, 74100, Bartın, TURKEY

<https://orcid.org/0009-0004-8751-0325>

³Department of Mathematics, Suleyman Demirel University, 32260, Isparta, TURKEY

<https://orcid.org/0000-0003-0866-1869>

*corresponding author: gurdalmehmet@sdu.edu.tr

(Received: 17.04.2024, Accepted: 10.06.2024, Published: 25.11.2024)

Abstract: This paper defines the space $S_{\theta_{uv}}^\alpha(\Delta_s^j, f)$, encompassing all sequences that are (Δ_s^j, f) -lacunary statistically convergent of order α , utilizing an unbounded modulus function f , a double lacunary sequence $\theta_{uv} = \{(k_u, l_v)\}$, a generalized difference operator Δ_s^j , and a real number $\alpha \in (0, 1]$. Additionally, the space $\omega_{\theta_{uv}}^\alpha(\Delta_s^j, f)$ is introduced to include all sequences that are strongly (Δ_s^j, f) -lacunary summable of order α . The paper investigates properties associated with these spaces, and under specific conditions, inclusion relations between the spaces $S_{\theta_{uv}}^\alpha(\Delta_s^j, f)$ and $\omega_{\theta_{uv}}^\alpha(\Delta_s^j, f)$ are established.

Key words: Lacunary sequences, Lacunary statistical convergence, Modulus function

1. Introduction

The extension of the notion of convergence for real sequences to statistical convergence was undertaken by Fast [1]. In [2], the connection between the space $|\sigma_1|$ of strongly Cesàro summable sequences and the space N_θ of strongly lacunary summable sequences, defined by a lacunary sequence θ , was established by Freedman et al.

For single sequences, Çolak [3] proposed the concepts of statistical convergence of order α and strongly p -Cesàro summability of order α . Lacunary statistical convergence was presented by Fridy and Orhan [4]. Recently, Şengül and Et [5] studied the concepts of lacunary statistical convergence of order α and strongly p -lacunary summability of order α .

Pringsheim introduced the idea of convergence for double sequences in [6]. Mursaleen and Edely [7] went on to expand this idea to statistical convergence. Patterson and Savaş [8] studied the concept of lacunary statistical convergence using the double lacunary sequence concept.

The double sequence $\theta_2 = \{(k_r, l_s)\}$ is termed double lacunary if there exist two increasing sequences of integers such that:

$$k_0 = 0, h_r = k_r - k_{r-1} \rightarrow \infty \text{ as } r \rightarrow \infty$$

and

$$l_0 = 0, \bar{h}_s = l_s - l_{s-1} \rightarrow \infty \text{ as } s \rightarrow \infty.$$

Notations: $k_{r,s} = k_r l_s, h_{r,s} = h_r \bar{h}_s$, the intervals determined by θ_2 are denoted as,

$$I_r = \{(k): k_{r-1} < k \leq k_r\},$$

$$I_s = \{(l): l_{s-1} < l \leq l_s\},$$

$$I_{r,s} = \{(k, l): k_{r-1} < k \leq k_r \& l_{s-1} < l \leq l_s\},$$

$$q_r = \frac{k_r}{k_{r-1}}, \bar{q}_s = \frac{l_s}{l_{s-1}}, \text{ and } q_{r,s} = q_r \bar{q}_s.$$

For double sequences, the notion of statistical convergence of order α was recently introduced by Çolak and Altın [9].

The difference operator Δ for ℓ_∞, c and c_0 was originally presented by Kizmaz [10]. Subsequently, the concept of the difference operator Δ was further expanded to a fixed positive integer j by Et and Çolak [11], who defined it in the following manner:

$$Y(\Delta^j) = \{w = (w_k) \in \omega: \Delta^j w \in Y\} \text{ for } Y = \ell_\infty, c \text{ and } c_0,$$

where $\Delta^j w = (\Delta^j w_k) = (\Delta^{j-1} w_k - \Delta^{j-1} w_{k+1})$ for $j \geq 1$ and $\Delta^0 w = (w_k)$.

Additionally, the expansion of this space was undertaken by Et and Esi [12], who introduced the sequence $s = (s_k)$ comprising non-zero complex numbers. The sequence space $Y(\Delta_s^j)$ was defined by them in the following manner:

$$Y(\Delta_s^j) = \{w = (w_k) \in \omega: \Delta_s^j w \in Y\} \text{ for } Y = \ell_\infty, c \text{ and } c_0,$$

where

$$\Delta_s^0 w_k = (s_k w_k)$$

and

$$\Delta_s^j w_k = \sum_{m=0}^j (-1)^m \binom{j}{m} s_{k+m} w_{k+m}$$

for $j \geq 1$.

Using the operator Δ^j , Tripathy and Et [13] proposed the notion of Δ^j -lacunary statistical convergent sequences and Δ^j -lacunary strongly summable sequences in 2005. The concept of the difference operator has been explored from diverse perspectives over the years by several authors [14-17].

Remember that a function $f: [0, \infty) \rightarrow [0, \infty)$ is considered a modulus function if and only if (a) $f(t) = 0$ iff $t = 0$, (b) $f(t+q) \leq f(t) + f(q)$, (c) f is increasing, and (d) f is continuous from the right at 0. This is in agreement with Maddox [18].

In 2014, the generalization of the concept of natural density was undertaken by Aizpuru et al. [19], who introduced the f -density of a subset K of positive integers utilizing an unbounded modulus function f . The expression for the f -density is given as

$$\delta^f(T) = \lim_{r \rightarrow \infty} \frac{f(|\{p \in T: p \leq r\}|)}{f(r)},$$

provided the limit exists.

The concepts of f -density and f -statistical convergence of order α were introduced by Bhardwaj and Dhawan [20]. Moreover, f -lacunary statistical convergence and strong f -lacunary summability of order α were defined by Şengül and Et [21]. In 2019, the $\Delta_s^j(f)$ -statistical convergence of order α was introduced by Et and Gidemem [6]. We recommend [22-26] for more recent findings on ideal convergence via modulus function and related findings.

2. Material and Method

A sequence $w = (w_{kl})$ is defined to be $\Delta_s^j(f)$ -statistical convergent of order α (sco α) to w_0 for all $\rho > 0$,

$$\lim_{m,n \rightarrow \infty} \frac{1}{f((mn)^\alpha)} f(|\{k \leq m, l \leq n: |\Delta_s^j w_{kl} - w_0| \geq \rho\}|) = 0.$$

This class of sequences, characterized by (Δ_s^j, f) -sco α is demonstrated by $S^\alpha(\Delta_s^j, f)$.

Let $\theta_{uv} = \{(k_u, l_v)\}$ be a lacunary sequence and $\alpha \in (0,1]$. A sequence $w = (w_{kl})$ is considered to be (Δ_s^j, f) -lacunary statistical convergent of order α (lsco α) to w_0 provided that for all $\rho > 0$,

$$\lim_{u,v \rightarrow \infty} \frac{1}{f(h_{uv}^\alpha)} f(|\{(k, l) \in I_{uv}: |\Delta_s^j w_{kl} - w_0| \geq \rho\}|) = 0.$$

In this scenario, we denote this convergence as $S_{\theta_{uv}}^\alpha(\Delta_s^j, f) - \lim w_{kl} = w_0$.

$S_{\theta_{uv}}^\alpha(\Delta_s^j, f)$ demonstrates the set of every sequences exhibiting (Δ_s^j, f) -lsco α .

A sequence $w = (w_{kl})$ is considered to be strongly (Δ_s^j, f) lacunary summable sequence of order α (lssco α) if there exists w_0 such that

$$\lim_{u,v \rightarrow \infty} \frac{1}{f(h_{uv}^\alpha)} \sum_{(k,l) \in I_{uv}} f(|\Delta_s^j w_{kl} - w_0|) = 0.$$

In this context, the set encompassing every strongly (Δ_s^j, f) -lssco α is indicated by $\omega_{\theta_{uv}}^\alpha(\Delta_s^j, f)$.

Furthermore, we define the space comprising all sequences that are strongly $\Delta_s^j(f)$ -Cesàro summable of order α as:

$$\omega^\alpha(\Delta_S^j, f) = \left\{ w \in \omega : \lim_{n \rightarrow \infty} \frac{1}{f((mn)^\alpha)} \sum_{k,l=1}^{m,n} f(|\Delta_S^j w_{kl} - w_0|) = 0, \text{ for some } w_0 \right\}.$$

In this paper, the objective is to generalize and consolidate well-established findings within the domain of lacunary statistical convergence and the f -statistical convergence of double sequences. In this study, the (Δ_S^j, f) -lacunary statistical convergence of order α has been defined, and the space $S_{\theta_{uv}}^\alpha(\Delta_S^j, f)$ has been introduced with the assistance of the lacunary sequence $\theta_{uv} = \{(k_u, l_v)\}$, the generalized difference operator Δ_S^j , and the unbounded modulus function (ubmf) f . The space $\omega_{\theta_{uv}}^\alpha(\Delta_S^j, f)$, encompassing every strongly (Δ_S^j, f) -lacunary summable double sequences of order α , has also been defined.

For the sake of this study, we assume that j is a constant positive integer, $\theta_{uv} = \{(k_u, l_v)\}$ is a double lacunary sequence, and $\alpha, \beta \in \mathbb{R}$ such that $0 < \alpha \leq \beta \leq 1$, (s_k) represents a fixed sequence of non-zero complex numbers, and the modulus function f is unbounded.

3. Results

Now we can start this section by giving our first result.

Theorem 3.1. Consider $w = (w_{kl})$ and $t = (t_{kl})$ as two arbitrary sequences. Then, followings hold:

1. If $S_{\theta_{uv}}^\alpha(\Delta_S^j, f) - \lim w_{kl} = w_0$ and $q \in \mathbb{C}$, then $S_{\theta_{uv}}^\alpha(\Delta_S^j, f) - \lim qw_{kl} = qw_0$.
2. If $S_{\theta_{uv}}^\alpha(\Delta_S^j, f) - \lim w_{kl} = w_0$ and $S_{\theta_{uv}}^\alpha(\Delta_S^j, f) - \lim t_{kl} = t_0$, then $S_{\theta_{uv}}^\alpha(\Delta_S^j, f) - \lim(w_{kl} + t_{kl}) = w_0 + t_0$.

Proof. Omitted.

Theorem 3.2. Subsequent inclusions are valid for any α, β with $0 < \alpha \leq \beta \leq 1$:

1. $S_{\theta_{uv}}^\alpha(\Delta_S^j, f) \subseteq S_{\theta_{uv}}^\beta(\Delta_S^j, f)$,
2. $\omega_{\theta_{uv}}^\alpha(\Delta_S^j, f) \subseteq \omega_{\theta_{uv}}^\beta(\Delta_S^j, f)$.

Proof. The demonstration for both parts is derived by observing that, due to the rising characteristic of the modulus function f . $f(h_{uv}^\alpha) \leq f(h_{uv}^\beta)$ for each $u, v \in \mathbb{N}$ if $0 < \alpha \leq \beta \leq 1$.

Theorem 3.3. Consider the lacunary sequence $\theta_{uv} = \{(k_u, l_v)\}$ such that $\liminf q_u > 1$ and $\liminf q_v > 1$. Let f be an ubmf, and there exists a positive constant c such that for each $\geq 0, z \geq 0, f(yz) \geq cf(y)f(z)$. Then, followings hold:

1. $S^\alpha(\Delta_S^j, f) \subseteq S_{\theta_{uv}}^\beta(\Delta_S^j, f)$,
2. $\omega^\alpha(\Delta_S^j, f) \subseteq \omega_{\theta_{uv}}^\beta(\Delta_S^j, f)$.

Proof. Presume that $\liminf q_u > 1$ and $\liminf q_v > 1$. So, there are $\kappa > 0$ and $\zeta > 0$ such that $q_u > 1 + \kappa$ and $q_v > 1 + \zeta$ for all u, v , which gives that

$$\frac{h_{uv}}{k_{uv}} \geq \frac{\kappa\zeta}{(1+\kappa)(1+\zeta)},$$

where $k_{uv} = k_u l_v$. Then, we obtain

$$h_{uv}^\alpha \geq \frac{(\kappa\zeta)^\alpha}{(1+\kappa)^\alpha(1+\zeta)^\alpha} (k_u l_v)^\alpha \Rightarrow f(h_{uv}^\alpha) \geq f\left(\frac{(\kappa\zeta)^\alpha}{(1+\kappa)^\alpha(1+\zeta)^\alpha} (k_u l_v)^\alpha\right),$$

as f is increasing.

This means

$$f(h_{uv}^\alpha) \geq cf\left(\frac{(\kappa\zeta)^\alpha}{(1+\kappa)^\alpha(1+\zeta)^\alpha}\right) f((k_u l_v)^\alpha),$$

due to assumption $f(yz) \geq cf(y)f(z)$.

Due to the increasing nature of the modulus function f and the fact that $\alpha \leq \beta$, it follows that $f(h_{uv}^\beta) \geq f(h_{uv}^\alpha)$. This implies

$$f(h_{uv}^\beta) \geq cf\left(\frac{(\kappa\zeta)^\alpha}{(1+\kappa)^\alpha(1+\zeta)^\alpha}\right) f((k_u l_v)^\alpha). \quad (1)$$

1. Let $w \in S^\alpha(\Delta_s^j, f)$. By leveraging the monotonically increasing nature of the modulus function f and inequality (1), we can derive the following conclusion:

$$\begin{aligned} & \frac{1}{f((k_u l_v)^\alpha)} f(|\{k \leq k_u, l \leq l_v: |\Delta_s^j w_{kl} - w_0| \geq \rho\}|) \\ & \geq \frac{1}{f((k_u l_v)^\alpha)} f(|\{(k, l) \in I_{uv}: |\Delta_s^j w_{kl} - w_0| \geq \rho\}|) \\ & \geq cf\left(\frac{(\kappa\zeta)^\alpha}{(1+\kappa)^\alpha(1+\zeta)^\alpha}\right) \frac{1}{f(h_{uv}^\beta)} f(|\{(k, l) \in I_{uv}: |\Delta_s^j w_{kl} - w_0| \geq \rho\}|). \end{aligned}$$

We find $w \in S_{\theta_{uv}}^\alpha(\Delta_s^j, f)$ when we take the limit as $u, v \rightarrow \infty$, which results in the inclusion.

2. Let $w \in \omega^\alpha(\Delta_s^j, f)$. Then, according to the inequality (1), we get

$$\begin{aligned} & \frac{1}{f((k_u l_v)^\alpha)} \sum_{k \leq k_u, l \leq l_v} f(|\Delta_s^j w_{kl} - w_0|) \\ & \geq cf\left(\frac{(\kappa\zeta)^\alpha}{(1+\kappa)^\alpha(1+\zeta)^\alpha}\right) \frac{1}{f(h_{uv}^\beta)} \sum_{(k,l) \in I_{uv}} f(|\Delta_s^j w_{kl} - w_0|). \end{aligned}$$

The required inclusion can be obtained by taking the limit as $u, v \rightarrow \infty$ on both sides.

Theorem 3.4. Consider the lacunary sequence $\theta_{uv} = \{(k_u, l_v)\}$ such that $\limsup_u q_u^\alpha < \infty$, $\limsup_v q_v^\alpha < \infty$, and an ubmf f such that for $c > 0$, $f(r) \leq cr$ for all $r \geq 0$. Then, followings hold:

1. $S_{\theta_{uv}}^\alpha(\Delta_s^j, f) \subseteq S^\beta(\Delta_s^j, f)$,
2. $\omega_{\theta_{uv}}^\alpha(\Delta_s^j, f) \subseteq \omega^\beta(\Delta_s^j, f)$.

Proof. (i) Suppose that $\limsup_u q_u^\alpha < \infty$, $\limsup_v q_v^\alpha < \infty$. So, there exists $T > 0$ so that $q_u^\alpha < T$ and $q_v^\alpha < T$ for $\forall u, v \in \mathbb{N}$. Let $w \in S_{\theta_{uv}}^\alpha(\Delta_S^j, f)$. For any $\rho > 0$, there are $u_0, v_0 \in \mathbb{N}$ so that

$$\frac{1}{f(h_{uv}^\alpha)} f(\{(k, l) \in I_{uv} : |\Delta_S^j w_{kl} - w_0| \geq \rho\}) < \rho$$

for all $u > u_0, v > v_0$,

$$\Rightarrow \frac{N_{uv}}{f(h_{uv}^\alpha)} < \rho \text{ for all } u > u_0, v > v_0,$$

where

$$N_{uv} = f(\{(k, l) \in I_{uv} : |\Delta_S^j w_{kl} - w_0| \geq \rho\}).$$

Let

$$M := \max\{N_{uv} : 1 \leq u \leq u_0 \text{ and } 1 \leq v \leq v_0\}.$$

Let n and m be such that $k_{u-1} < m \leq k_u$ and $l_{v-1} < n \leq l_v$. Therefore, we deduce the following:

$$\begin{aligned} \frac{1}{f((mn)^\beta)} f(\{k \leq m \text{ and } l \leq n : |\Delta_S^j w_{kl} - w_0| \geq \rho\}) &\leq \frac{1}{f((k_{u-1}l_{v-1})^\alpha)} \{k \leq k_u \text{ and } l \\ &\leq l_v : |\Delta_S^j w_{kl} - w_0| \geq \rho\} = \frac{1}{f((k_{u-1}l_{v-1})^\alpha)} \left\{ \sum_{i,j=1,1}^{r,s} N_{i,j} \right\} \\ &\leq \frac{Mu_0v_0}{f((k_{u-1}l_{v-1})^\alpha)} + \frac{1}{f((k_{u-1}l_{v-1})^\alpha)} \left\{ \sum_{i,j=u_0+1,v_0+1}^{u,v} N_{i,j} \right\} \\ &\leq \frac{Mu_0v_0}{f((k_{u-1}l_{v-1})^\alpha)} + \frac{1}{f((k_{u-1}l_{v-1})^\alpha)} \left\{ \sum_{i,j=u_0+1,v_0+1}^{u,v} \frac{N_{i,j} f(h_{i,j}^\alpha)}{f(h_{i,j}^\alpha)} \right\} \\ &\leq \frac{Mu_0v_0}{f((k_{u-1}l_{v-1})^\alpha)} + \frac{1}{f((k_{u-1}l_{v-1})^\alpha)} \left(\sup_{i,j \geq u_0, v_0} \frac{N_{i,j}}{f(h_{i,j}^\alpha)} \right) c \cdot \left\{ \sum_{i,j=u_0+1,v_0+1}^{u,v} h_{i,j}^\alpha \right\} \\ &\leq \frac{Mu_0v_0}{f((k_{u-1}l_{v-1})^\alpha)} + \rho \cdot c \cdot \left\{ \sum_{i,j=u_0+1,v_0+1}^{u,v} h_{i,j}^\alpha \right\} \leq \frac{Mu_0v_0}{f((k_{u-1}l_{v-1})^\alpha)} + \rho \cdot c \cdot T^2. \end{aligned}$$

The inclusion follows by taking the limit in the above inequality.

(ii) Since the evidence is identical to part (i), it is omitted.

Theorem 3.5. Let $\theta_{uv} = \{(k_u, l_v)\}$ be a double lacunary sequence such that $\lim_{u,v \rightarrow \infty} \frac{f(h_{uv}^\beta)}{f((k_u l_v)^\alpha)} > 0$ and $\alpha, \beta \in \mathbb{R}$ such that $0 < \alpha \leq \beta \leq 1$. Then, followings hold:

- i. $S^\alpha(\Delta_S^j, f) \subseteq S_{\theta_{uv}}^\beta(\Delta_S^j, f)$,
- ii. $\omega^\alpha(\Delta_S^j, f) \subseteq \omega_{\theta_{uv}}^\beta(\Delta_S^j, f)$.

Proof. (i) Let $w \in S^\alpha(\Delta_S^j, f)$. Then

$$\lim_{m,n \rightarrow \infty} \frac{1}{f((mn)^\alpha)} f(|\{k \leq m, l \leq n: |\Delta_s^j w_{kl} - w_0| \geq \rho\}|) = 0,$$

which implies

$$\lim_{u,v \rightarrow \infty} \frac{1}{f((k_u l_v)^\alpha)} f(|\{k \leq k_u, l \leq l_v: |\Delta_s^j w_{kl} - w_0| \geq \rho\}|) = 0.$$

Take $\rho > 0$. Then, for all u, v ,

$$\{(k, l) \in I_{uv}: |\Delta_s^j w_{kl} - w_0| \geq \rho\} \subseteq \{k \leq k_u \text{ and } l \leq l_v: |\Delta_s^j w_{kl} - w_0| \geq \rho\}.$$

Through the increasing property of the modulus function, it is obtained that

$$\begin{aligned} f(|\{(k, l) \in I_{uv}: |\Delta_s^j w_{kl} - w_0| \geq \rho\}|) &\leq f(|\{k \leq k_u \text{ and } l \leq l_v: |\Delta_s^j w_{kl} - w_0| \geq \rho\}|) \\ &\Rightarrow \frac{f(h_{uv}^\beta)}{f((k_u l_v)^\alpha)} \frac{1}{f(h_{uv}^\beta)} f(|\{(k, l) \in I_{uv}: |\Delta_s^j w_{kl} - w_0| \geq \rho\}|) \\ &\leq \frac{1}{f((k_u l_v)^\alpha)} f(|\{k \leq k_u \text{ and } l \leq l_v: |\Delta_s^j w_{kl} - w_0| \geq \rho\}|). \end{aligned}$$

By taking the limit as $u, v \rightarrow \infty$ on both sides and utilizing the given assumption, the inclusion is established.

(ii) The inclusion is followed in the same manner as in part (i) by being aware that

$$\sum_{(k,l) \in I_{uv}} f(|\Delta_s^j w_{kl} - w_0|) \leq \sum_{k \leq k_u \text{ and } l \leq l_v} f(|\Delta_s^j w_{kl} - w_0|),$$

holds for any $u, v \in \mathbb{N}$.

Theorem 3.6. For real numbers α and β with $0 < \alpha \leq \beta \leq 1$, the inclusion

$$S_{\theta_{uv}}^\alpha(\Delta_s^j, f) \subseteq S_{\theta_{uv}}^\beta(\Delta_s^j)$$

holds.

Proof. Let $w \in S_{\theta_{uv}}^\alpha(\Delta_s^j, f)$. For all $r \in \mathbb{N}$, there is a $n_0 \in \mathbb{N}$ such that whenever $n \geq n_0$, we have

$$\begin{aligned} \frac{1}{f(h_{uv}^\alpha)} f(|\{(k, l) \in I_{uv}: |\Delta_s^j w_{kl} - w_0| \geq \rho\}|) &\leq \frac{1}{r} \\ &\Rightarrow f(|\{(k, l) \in I_{uv}: |\Delta_s^j w_{kl} - w_0| \geq \rho\}|) \leq \frac{1}{r} f\left(\frac{r \cdot h_{uv}^\alpha}{r}\right). \end{aligned}$$

Utilizing the subadditive property of the modulus function f , we obtain

$$\begin{aligned}
f(|\{(k, l) \in I_{uv} : |\Delta_s^j w_{kl} - w_0| \geq \rho\}|) &\leq \frac{1}{r} r f\left(\frac{h_{uv}^\alpha}{r}\right) \\
&\Rightarrow |\{(k, l) \in I_{uv} : |\Delta_s^j w_{kl} - w_0| \geq \rho\}| \\
&\leq \frac{h_{uv}^\alpha}{r}, \text{ as } f \text{ is an increasing function} \\
&\Rightarrow \frac{1}{h_{uv}^\beta} |\{(k, l) \in I_{uv} : |\Delta_s^j w_{kl} - w_0| \geq \rho\}| \leq \frac{1}{r}.
\end{aligned}$$

Taking the limit as $u, v \rightarrow \infty$, we get $w \in S_{\theta_{uv}}^\beta(\Delta_s^j)$.

Lemma 3.1. [18] For any modulus function f , $\lim_{q \rightarrow \infty} \frac{f(q)}{q} = \inf\left\{\frac{f(q)}{q} : q > 0\right\}$.

Theorem 3.7. Let's suppose there exists a modulus function f so that $\lim_{q \rightarrow \infty} \frac{f(q)}{q} > 0$. Then,

$$\omega_{\theta_{uv}}^\alpha(\Delta_s^j, f) \subseteq \omega_{\theta_{uv}}^\beta(\Delta_s^j).$$

Proof. Let $w \in \omega_{\theta_{uv}}^\alpha(\Delta_s^j, f)$ and $\lim_{q \rightarrow \infty} \frac{f(q)}{q} = \sigma$. Then, according to Lemma 3.1 $\sigma = \inf\left\{\frac{f(q)}{q} : q > 0\right\}$. This implies $q \leq \sigma^{-1}f(q)$ for $\forall q \geq 0$. Now,

$$\begin{aligned}
\frac{1}{f(h_{uv}^\beta)} \sum_{(k,l) \in I_{uv}} |\Delta_s^j w_{kl} - w_0| &\leq \frac{1}{f(h_{uv}^\beta)} \sum_{(k,l) \in I_{uv}} \sigma^{-1} f(|\Delta_s^j w_{kl} - w_0|) \\
&\leq \frac{\sigma^{-1}}{f(h_{uv}^\alpha)} \sum_{(k,l) \in I_{uv}} f(|\Delta_s^j w_{kl} - w_0|).
\end{aligned}$$

Taking the limit as $u, v \rightarrow \infty$, results in the inclusion.

Theorem 3.8. Given an unbounded modulus function, denoted as f , and assuming it satisfies the inequality $f(yz) \geq cf(y)f(z)$ for some positive fixed c . Then,

$$\omega_{\theta_{uv}}^\alpha(\Delta_s^j, f) \subseteq S_{\theta_{uv}}^\beta(\Delta_s^j, f).$$

Proof. Assume $w \in \omega_{\theta_{uv}}^\alpha(\Delta_s^j, f)$ and $\rho > 0$. Using the modulus function's increasing and subadditive properties, we arrive at

$$\begin{aligned}
\frac{1}{f(h_{uv}^\alpha)} \sum_{(k,l) \in I_{uv}} f(|\Delta_s^j w_{kl} - w_0|) &\geq \frac{1}{f(h_{uv}^\alpha)} f\left(\sum_{(k,l) \in I_{uv}} |\Delta_s^j w_{kl} - w_0|\right) \\
&\geq \frac{1}{f(h_{uv}^\beta)} f\left(\sum_{(k,l) \in I_{uv} \& |\Delta_s^j w_{kl} - w_0| \geq \rho} |\Delta_s^j w_{kl} - w_0|\right) \\
&\geq \frac{1}{f(h_{uv}^\beta)} f(|\{(k, l) \in I_{uv} : |\Delta_s^j w_{kl} - w_0| \geq \rho\}| \rho) \\
&\geq \frac{c}{f(h_{uv}^\beta)} f(|\{(k, l) \in I_{uv} : |\Delta_s^j w_{kl} - w_0| \geq \rho\}|) f(\rho),
\end{aligned}$$

utilizing $f(yz) \geq cf(y)f(z)$.

Taking the limit as $u, v \rightarrow \infty$, we get $w \in S_{\theta_{uv}}^\beta(\Delta_S^j, f)$.

Theorem 3.9. Assume that the modulus function f and the lacunary sequence $\theta_{uv} = \{(k_u, l_v)\}$ satisfy $\lim_{q \rightarrow \infty} \frac{f(q)}{q} > 0$ and $\lim_{u, v \rightarrow \infty} \frac{f(h_{uv})}{f(h_{uv}^\alpha)} = 1$. Then, the inclusion

$$S_{\theta_{uv}}^\alpha(\Delta_S^j, f) \cap \ell_\infty(\Delta_S^j) \subseteq \omega_{\theta_{uv}}^\beta(\Delta_S^j, f) \cap \ell_\infty(\Delta_S^j),$$

holds.

Proof. Suppose $\lim_{q \rightarrow \infty} \frac{f(q)}{q} = \sigma$. According to Lemma 3.1 $\sigma = \inf\{\frac{f(q)}{q} : q > 0\}$, which implies $q \leq \sigma^{-1}f(q)$ for all $q \geq 0$. Now, let $w \in S_{\theta_{uv}}^\alpha(\Delta_S^j, f) \cap \ell_\infty(\Delta_S^j)$, meaning there exists $U > 0$ such that $|\Delta_S^j w_{kl} - w_0| \leq U$ for all $k, l \in \mathbb{N}$. For all $\varepsilon > 0$, consider Σ_1 and Σ_2 as the sums over $(k, l) \in I_{uv}$ $|\Delta_S^j w_{kl} - w_0| \geq \rho$ and $(k, l) \in I_{uv}$, $|\Delta_S^j w_{kl} - w_0| < \rho$, respectively. Now,

$$\begin{aligned} & \frac{1}{f(h_{uv}^\beta)} \sum_{(k,l) \in I_{uv}} f(|\Delta_S^j w_{kl} - w_0|) \\ & \leq \frac{1}{f(h_{uv}^\alpha)} \left(\sum_1 f(|\Delta_S^j w_{kl} - w_0|) + \sum_2 f(|\Delta_S^j w_{kl} - w_0|) \right) \\ & \leq \frac{1}{f(h_{uv}^\alpha)} \sum_1 f(U) + \frac{1}{f(h_{uv}^\alpha)} \sum_2 f(\rho) \\ & \leq \frac{1}{f(h_{uv}^\alpha)} |\{(k, l) \in I_{uv} : |\Delta_S^j w_{kl} - w_0| \geq \rho\}| f(U) + \frac{h_{uv}}{f(h_{uv}^\alpha)} f(\rho) \\ & \leq \frac{\sigma^{-1}}{f(h_{uv}^\alpha)} f(|\{(k, l) \in I_{uv} : |\Delta_S^j w_{kl} - w_0| \geq \rho\}|) f(U) + \frac{\sigma^{-1} f(h_{uv})}{f(h_{uv}^\alpha)} f(\rho). \end{aligned}$$

By taking the limit as $u, v \rightarrow \infty$ and utilizing $\lim_{u, v \rightarrow \infty} \frac{f(h_{uv})}{f(h_{uv}^\alpha)} = 1$, the inclusion is established.

The lacunary sequence $\theta'_{uv} = \{k'_u, l'_v\}$ is known as lacunary refinement of lacunary sequence $\theta_{uv} = \{k_u, l_v\}$ if $\{k_u, l_v\} \subseteq \{k'_u, l'_v\}$. In this case $I_{uv} \subseteq I'_{uv}$ where $I'_{uv} = \{(k', l') : k'_{u-1} < k' \leq k'_u, l'_{v-1} < l' \leq l'_v\}$.

Theorem 3.10. Let $\theta'_{uv} = \{k'_u, l'_v\}$ be lacunary refinement of $\theta_{uv} = \{k_u, l_v\}$ and $0 < \alpha \leq \beta \leq 1$. Additionally, suppose lacunary sequences $\theta_{uv} = \{(k_u, l_v)\}$, $\theta'_{uv} = \{(k'_u, l'_v)\}$ and a modulus function f satisfy $\liminf \frac{f(h_{uv}^\beta)}{f(l_{uv}^\alpha)} > 0$. Then, followings hold:

1. $S_{\theta'_{uv}}^\alpha(\Delta_S^j, f) \subseteq S_{\theta_{uv}}^\beta(\Delta_S^j, f)$,
2. $\omega_{\theta'_{uv}}^\alpha(\Delta_S^j, f) \subseteq \omega_{\theta_{uv}}^\beta(\Delta_S^j, f)$.

Proof. (i) Consider $w \in S_{\theta'_{uv}}^\alpha(\Delta_S^j, f)$. As $I_{uv} \subseteq I'_{uv}$ for all $u, v \in \mathbb{N}$, so for any $\rho > 0$, we can conclude that

$$\begin{aligned} & \{(k, l) \in I_{uv}, |\Delta_s^j w_{kl} - w_0| \geq \rho\} \subseteq \{(k, l) \in I'_{uv}: |\Delta_s^j w_{kl} - w_0| \geq \rho\}, \\ \Rightarrow & f(|\{(k, l) \in I_{uv}: |\Delta_s^j w_{kl} - w_0| \geq \rho\}|) \leq f(|\{(k, l) \in I'_{uv}: |\Delta_s^j w_{kl} - w_0| \geq \rho\}|), \end{aligned}$$

as f is increasing

$$\begin{aligned} \Rightarrow & \frac{f(h_{uv}^\beta)}{f(l_{uv}^\alpha)} \frac{1}{f(h_{uv}^\beta)} f(|\{(k, l) \in I_{uv}, |\Delta_s^j w_{kl} - w_0| \geq \rho\}|) \\ & \leq \frac{1}{f(l_{uv}^\alpha)} f(|\{(k, l) \in I'_{uv}: |\Delta_s^j w_{kl} - w_0| \geq \rho\}|) \end{aligned}$$

for all $u, v \in \mathbb{N}$.

By letting $u, v \rightarrow \infty$ and utilizing $\liminf \frac{f(h_{uv}^\beta)}{f(l_{uv}^\alpha)} > 0$, the desired inclusion follows.

(ii) Take $w \in \omega_{\theta_{uv}}^\alpha(\Delta_s^j, f)$. Inclusion ensues through taking the limit and employing the provided assumption in the subsequent inequality

$$\frac{1}{f(l_{uv}^\alpha)} \sum_{(k,l) \in I'_{uv}} f(|\Delta_s^j w_{kl} - w_0|) \geq \frac{f(h_{uv}^\beta)}{f(l_{uv}^\alpha)} \frac{1}{f(h_{uv}^\beta)} \sum_{(k,l) \in I_{uv}} f(|\Delta_s^j w_{kl} - w_0|).$$

4. Conclusion

In conclusion, this paper has introduced and explored the spaces $S_{\theta_{uv}}^\alpha(\Delta_s^j, f)$ and $\omega_{\theta_{uv}}^\alpha(\Delta_s^j, f)$, which respectively encompass sequences that exhibit (Δ_s^j, f) -lacunary statistical convergence of order α and strong (Δ_s^j, f) -lacunary summability of order α . The definitions of these spaces involved the use of an unbounded modulus function f , a lacunary sequence $\theta_{uv} = \{(k_u, l_v)\}$, a generalized difference operator Δ_s^j , and a real number $\alpha \in (0, 1]$. The properties of these spaces were thoroughly examined, including the establishment of inclusion relations under specific conditions.

The significance of this work lies in the extension and unification of concepts in the realm of statistical convergence. By introducing and studying these spaces, we provide a comprehensive framework for understanding the behavior of sequences that exhibit certain convergence properties. The spaces $S_{\theta_{uv}}^\alpha(\Delta_s^j, f)$ and $\omega_{\theta_{uv}}^\alpha(\Delta_s^j, f)$ offer valuable insights into the convergence patterns of sequences, facilitating a deeper understanding of their statistical and summability characteristics. This research contributes to the broader field of mathematical analysis, providing new tools and perspectives for studying the convergence behavior of sequences in various contexts.

Authorship contribution statement

Ö. Kişi: Conceptualization, Methodology; **R. Akbiyık:** Data Curation, Original Draft Writing; **M. Gürdal:** Visualization, Supervision/Observation/Advice.

Declaration of competing interest

The authors declare that they have no known competing financial interests or personal relationships that could have appeared to influence the work reported in this paper.

Ethics Committee Approval and/or Informed Consent Information

As the authors of this study, we declare that we do not have any ethics committee approval and/or informed consent statement.

References

- [1] H. Fast, “Sur la convergence statistique”, *Colloquium Mathematicum*, 2, 241-244, 1951.
- [2] A. R. Freedman, J. J. Sember and M. Raphael, “Some Cesàro type summability spaces”, *Proceedings of the London Mathematical Society*, 37, 508-520, 1978.
- [3] R. Çolak, “Statistical convergence of order α ”, *Modern Methods in Analysis and Its Applications*, 1, 2010, pp. 121-129.
- [4] J. A. Fridy and C. Orhan, “Lacunary statistical convergent”, *Pacific Journal of Mathematics*, 160, 43-51, 1993.
- [5] H. Şengül and M. Et, “On lacunary statistical convergence of order α ”, *Acta Mathematica Scientia*, 34(2), 473-482, 2014.
- [6] A. Pringsheim, “Zur theorie der zweifach unendlichen Zahlenfolgen”, *Mathematische Annalen*, 53, 289-321, 1900.
- [7] M. Mursaleen and O. H. H. Edely, “Statistical convergence of double sequences”, *Journal of Mathematical Analysis and Applications*, 288, 223-231, 2003.
- [8] R. F. Patterson and E. Savaş, “Lacunary statistical convergence of double sequences”, *Mathematical Communications*, 10, 55-61, 2005.
- [9] R. Çolak and Y. Altın, “Statistical convergence of double sequences of order α ”, *Journal of Function Spaces*, 2013, 1-5, 2013.
- [10] H. Kizmaz, “On certain sequence spaces”, *Canadian Mathematical Bulletin*, 24(2), 169-176, 1981.
- [11] M. Et and R. Çolak, “On some generalized difference sequence spaces”, *Soochow Journal of Mathematics*, 21(4), 377-386, 1995.
- [12] M. Et and A. Esi, “On Köthe-Toeplitz duals of generalized difference sequence spaces”, *Bulletin of the Malaysian Mathematical Sciences Society*, 23(1), 25-32, 2000.
- [13] B. C. Tripathy and M. Et, “On generalized difference lacunary statistical convergence”, *Studia Universitatis Babeş-Bolyai Mathematica*, 50(1), 119-130, 2005.
- [14] B. C. Tripathy and S. Mahanta, “On a class of generalized lacunary difference sequence spaces defined by Orlicz functions”, *Acta Mathematica Sinica, English Series*, 20(2), 231-238, 2004.
- [15] B. C. Tripathy and H. Dutta, “On some lacunary difference sequence spaces defined by a sequence of Orlicz functions and q -lacunary Δ_m^n -statistical convergence”, *Analele Stiintifice ale Universitatii Ovidius Constanta, Seria Mathematica*, 20(1), 417-430, 2012.
- [16] A. K. Verma and L. K. Singh, “ (Δ_V^m, f) -lacunary statistical convergence of order α ”, *Proyecciones*, 41(4), 791-804, 2022.
- [17] M. Et and H. Gidemen, “On $\Delta_V^m(f)$ -statistical convergence of order α ”, *Communications in Statistics-Theory and Methods*, 49(14), 3521-3529, 2020.
- [18] I. J. Maddox, “Sequence spaces defined by a modulus”, *Mathematical Proceedings of the Cambridge Philodophical Society*, 100, 161-166, 1986.
- [19] A. Aizpuru, M. C. Listán-García, and F. Rambla-Barreno, “Density by moduli and statistical convergence”, *Quaestiones Mathematicae*, 37(4), 525-530, 2014.
- [20] S. Gupta and V. K. Bhardwaj, “On deferred f -statistical convergence”, *Kyungpook Mathematical Journal*, 58(1), 91-103, 2018.
- [21] Ş. Şengül and M. Et, “ f -lacunary statistical convergence and strong f -lacunary summability of order α ”, *Filomat*, 32(13), 4513-4521, 2018.
- [22] E. Dündar and N. Akın, “ f -asymptotically I_2^f -equivalence of double sequences of sets”, *Afyon Kocatepe University Journal of Science and Engineering*, 19(1), 79-86, 2019.
- [23] E. Dündar and N. Akın, “ f -asymptotically $I\sigma$ -equivalence of real sequences”, *Konuralp Journal of Mathematics*, 8(1), 207-210, 2020.

-
- [24] E. Dündar and N. Akın, “ f -asymptotically $I_2^{\sigma\theta}$ -equivalence for double set sequences”, *Karaelmas Science and Engineering Journal*, 10(1), 26-31, 2020.
- [25] E. Dündar and N. Akın, “ f -asymptotically $I_{\sigma\theta}$ -equivalence of real sequences”, *Journal of Mathematical Sciences and Modelling*, 3(1), 32-37, 2020.
- [26] E. Dündar, N. Akın and U. Ulus, “Asymptotical invariant and asymptotical lacunary invariant equivalence types for double sequences via ideals using modulus functions”, *Honam Mathematical Journal*, 43(1), 100-114, 2021.

Genotoxicity and Oxidative Stress of Water Concentrates from Recreation Pools After Various Disinfection Methods

Zafer Bektaş¹, Melda Şahin^{2,*}, Vehbi Atahan Toğay³, Uğur Şahin^{1,4}, Mustafa Calapoğlu¹

¹ Department of Chemistry, Faculty of Art and Science, University of Süleyman Demirel, 32200, Isparta, TÜRKİYE

<https://orcid.org/0000-0002-4808-0068>

<https://orcid.org/0000-0002-9567-7270>

² Department of Bioengineering, Institute of Science, University of Süleyman Demirel, 32200, Isparta, TÜRKİYE

<https://orcid.org/0000-0001-9207-6931>

*corresponding author: meldasahin0510@gmail.com

³ Department of Medical Biology, Faculty of Medicine, University of Süleyman Demirel, 32200, Isparta, TÜRKİYE

<https://orcid.org/0000-0003-4722-3845>

⁴ Genetic Research Unit, Innovative Technologies Application and Research Center, University of Süleyman Demirel, 32200, Isparta, TÜRKİYE

<https://orcid.org/0000-0002-5629-3485>

(Received: 25.04.2024, Accepted: 11.06.2024, Published: 25.11.2024)

Abstract: In this study, it was aimed to evaluate the pool water quality, bacterial contamination, genotoxicity and oxidative damage parameters according to different disinfection methods in regression swimming pools in tourist facilities in Antalya, Türkiye in March 2019. For this purpose disinfected pool water samples and erythrocyte solutions and lymphocytes were incubated at two hours. At the end of the incubation, erythrocyte lipid peroxidation by thiobarbituric acid reactive substances method and peripheral blood lymphocytes DNA damage by the single cell gel electrophoresis assay were determined. It showed that all recreational pool water samples disinfected with different disinfectants caused more DNA damage and oxidative stress than mains water. Genotoxicity and oxidative stress data showed that the silver-copper ionization method was the best disinfection method compared to other disinfection methods. Our findings support the potential genotoxic and oxidative stress effects of exposure to disinfectant residues due to different disinfectant uses in regression swimming pools. The positive effects of swimming on human health, continuous monitoring of the quality of pool water and the preference of silver-copper ionization for disinfection can reduce potential health risks.

Key words: Swimming pools, Cytotoxicity, Genotoxicity, Oxidative stress

1. Introduction

While swimming pools have long been a tool for exercise and relaxation around the world, it remains one of the most popular and attractive activities due to its positive effects on health [1,2]. Unhygienic pools harbor potentially accumulated harmful microorganisms and organic matter. Pathogenic microorganisms and environmental pollutants directly or indirectly enter pools and cause water-borne infections. Microorganisms that cause infections in pool water can be transmitted to swimming pool users through saliva, blood, urine, vomit and feces [3,4]. Disinfectants (such as chlorine, chloramines, ozone and UV) used in swimming pools to neutralize microorganisms and reduce the health hazard of pool users, also provide the formation of residual disinfectant

that harm the health of people using these pools [5]. It has been determined that the residual disinfectant formed after disinfection is cytotoxic, neurotoxic and genotoxic. In addition, residual disinfectant has been found to be mutagenic, carcinogenic and/or teratogenic [6]. Since chlorine, which is widely used in the disinfection of swimming pool water, creates many organohalogenated DBPs, research on alternative methods for disinfection (such as ozone, hydrogen peroxide, copper-silver ionization and UV) of swimming pool water is increasing [7, 8].

Reactive chemicals used in pool water disinfection cause cellular damage by directly or indirectly oxidizing DNA, protein/peptide and lipids. The resulting oxidation products, together with the reactive species produced by disinfection, bind inflammatory cells, causing oxidative stress [9, 10]. The disinfectant residue formed because of disinfection used in pool water can cause a general oxidative stress in cells and tissues [11]. Exposure to residual disinfectant has been found to induce several molecular signaling pathways in the cellular response to oxidative, genotoxic, and proteotoxic stresses. Exposure to residual disinfectants created by disinfection methods (such as ozone, hydrogen peroxide, copper-silver ionization and UV) used in pool water has been found to induce various molecular signaling pathways in the cellular response to oxidative, genotoxic and proteotoxic stresses [10-13]. The formation of residual disinfectants can cause cancer, degenerative conditions, and immune system dysfunction in somatic cells, while DNA damage in germ cells is linked to reproductive dysfunction, hereditary damage, and developmental defects. Therefore, many studies have focused on the genotoxic effects of residual disinfectants after disinfection of pool water [14-17].

While previous researchers have focused on the concentrations of certain disinfectant residues in recreational waters and tried to correlate them with adverse health outcomes in humans, these efforts may fall short due to the wide variety of toxic components in these waters due to different disinfection methods. The main purpose of this study is to compare the genotoxicity and oxidative stress parameters of recreational waters obtained from a single source treated with different disinfectants (chlorine, ozone, hydrogen peroxide and copper-silver ionization), rather than trying to relate specific residual disinfectants or DBPs with genotoxicity and oxidative stress. In our study, we applied water samples collected from four regression pools with different disinfection methods to erythrocyte and lymphocyte cultures and compared genotoxicity and oxidative stress parameters with main water serving as a common source. Our results can help identify different disinfection treatments in a recreational water system and their impact on human health.

2. Material and Method

2.1. Chemical and reagents

Sodium chloride (NaCl), potassium chloride (KCl), disodium hydrogen phosphate (Na_2HPO_4), trichloroacetic acid (TCA), potassium dihydrogen phosphate (KH_2PO_4), triton-X-100 ($\text{C}_8\text{H}_{17}\text{C}_6\text{H}_4(\text{OC}_2\text{H}_4)_{9-10}\text{OH}$), thiobarbituric acid (TBA), sodium hydroxide (NaOH), hydrogen chloride (HCl) purchased from the company Merck. Sodium bicarbonate (NaHCO_3), citric acid ($\text{C}_6\text{H}_8\text{O}_7$), tris base ($\text{NH}_2\text{C}(\text{CH}_2\text{OH})_3$), acetic acid ($\text{C}_2\text{H}_4\text{O}_2$), ethanol ($\text{C}_2\text{H}_6\text{O}$), tris aminomethane ($\text{NH}_2\text{C}(\text{CH}_2\text{OH})_3$), sodium mono hydrogen phosphate ($\text{Na}_2\text{HPO}_4 \cdot 7\text{H}_2\text{O}$) were supplied by SIGMA company.

2.2. Sampling and analysis

Swimming pool samples were collected from five different regression pools using the same mains water located in the city of Antalya (Türkiye), with an estimated length of 25 m, a width of 12.5 m, and a depth of 1.5-2.5 m. Water samples were taken in March 2019. Sampling in ponds was done 15 to 30 cm below the water surface. Each of the locations

was systematically sampled on alternating days at times when it was open to the public (between 12 and 14 hours). Samples were collected in sterilized vials and immediately transported to the laboratory. All samples were kept at +4°C until the time of study. Water sample characteristics are provided in Table 1.

Table 1. Characteristics of pool samples

Pool Code	Type	Location	Temperature (°C)	Disinfection Procedure
1	cold pool	indoor	25 – 27 °C	Chlorination
2	cold pool	indoor	25 – 27 °C	Ozonation
3	cold pool	indoor	25 – 27 °C	Hydrogen peroxidation
4	cold pool	indoor	25 – 27 °C	Silver-copper ionization
5	cold pool	indoor	25 – 27 °C	Mains water

2.3. Determination of physical–chemical parameters

The main purpose of physical and chemical research was to determine the chemical composition of water, with special consideration of substances hazardous to human health. All physical and chemical laboratory tests were done on the day of sample collection, according to the Water Environmental Federation, and American Public Health Association (APHA) [18] and the findings were compared with local guidelines. Swimming pool water temperature (°C) and pH values were measured using a Testo 106 brand temperature meter and WTW pH 330i brand pH-meter, respectively. Other chemical parameters were analyzed according to APHA, and the findings were compared with local guidelines [18].

2.4. Determination of microbial factors

The main goal of the microbiological research was to assessment the time-dependent variation of *Escherichia coli* (*E. Coli*) growth, which plays a dominant role in the control process of swimming pool water quality, regardless of the degree of contamination of the pool water with DBP using different disinfectants. Microbiological analysis according to time in regression pools with four different disinfections was performed according to the TS-EN-ISO-9308-1 method.

2.5. Determination of erythrocyte MDA levels

The levels of TBARS in erythrocytes were determined as described previously by Stocks and Dormandy with some modifications [19]. Blood was collected in vials containing heparin (10 U/mL), from healthy cows slaughtered at the slaughterhouse. Erythrocytes resuspended at 3 mg/dL hemoglobin in PBS containing 2 mM sodium azide as catalase inhibitor. This suspension was incubated at 37°C for 60 min in a shaking water bath to allow inactivation of erythrocyte catalase by the sodium azide. Freshly disinfected pool waters, main waters (control), positive control (50 µM t-BHP) and negative control (50 µM resveratrol) were equilibrated with PBS puffer (50 mM, pH=7.4). The 3 mL of each sample were taken and incubated with 1 mL previously prepared red cells suspension at 37°C for 120 min in a shaking water bath. The positive control contains 1.5 mM t-butylhydroperoxide (t-BHP) volume of in the place of the samples. After the incubation, 900 µL of the erythrocytes exposed to different compounds were mixed with 600 µL of 28% TCA and centrifuged over 10 min at 4500 rpm at room temperature. Thereafter, an aliquot of 800 µL of supernatant was added to 400 µL of thiobarbituric acid (0.069 M).

The resulting samples were heated at 100 °C for 60 min. After cooling, the intensity of pink color of the end fraction product was determined at 532 and 600 nm. MDA concentrations were calculated as follows:

$$MDA = (A_{532} - A_{600}) \times 900 = nmolMDA/g Hb.$$

2.6. The comet assay analysis

Cell viability was assessed by trypan blue staining, and samples with >90% viability were used. Lymphocytes were isolated by mixing bloods with Histopaque-1077 (Sigma, Germany) at a ratio of 1:1 and centrifuged at 2000 rpm for 10 min. at 4 °C. Pool waters and unconditioned water (negative control) samples buffered with 1 mL of PBS (50 mM PBS, pH=7.4) was added to lymphocytes and lymphocyte suspensions were incubated at 37°C for 1 and 2 h. Each sample was subjected to triplicate analysis.

The comet assays analysis was carried out under alkaline conditions, basically as described by Singh et al. with minor modifications [20]. Cell suspensions were centrifuged at 2500 rpm for 10 min. after incubation, supernatant was removed and centrifuged again at 2500 rpm for 10 min by adding 1:1 phosphate buffered saline (PBS). The supernatant was removed again and diluted with PBS depending on the density of the remaining cells. Approximately 50 µl of cell suspension (approximately 5×10^4 cells) mixed with 100 µL 0.75% low-melting agarose (LMA, Fisher Scientific), spread on slides that had previously been coated with 1.0% normal-melting agarose (NMA, Serva Electrophoresis GmbH), and covered with a coverslip. 5 min later the coverslip was removed without damaging the agarose gel and the slides were held in lysis solution (freshly added 2.5 M NaCl, 100 mM Na₂-EDTA, 10 mM Tris, pH 10, 10% DMSO, and 1% Triton X-100) in the dark at 4°C for 120 min. Then, they were incubated in freshly prepared cold electrophoresis solution (300 mM NaOH, 1 mM EDTA, pH 13) for 20 min in the dark at 4 °C. Then, the slides were placed in an electrophoresis tank containing electrophoresis solution, and electrophoresis was applied at 25 V (1.02 V/cm) for 30 min. Cells were then washed three times with neutralization buffer. Samples were stained with ethidium bromide and photographed with Zeiss Axiocam Icc 1 camera under Zeiss Imager A1 fluorescence microscope. An average of 100 cells per slide were evaluated automatically using Open Comet software [21]. Tail moment, tail length and tail density parameters were used to evaluate DNA damage.

2.7. Statistical analysis

Statistical analyses were evaluated using the SPSS version 11.5 (SPSS Inc., Chicago, Illinois, USA) statistical program. Differences between groups were assessed using analysis of variance (ANOVA) followed by Tukey multiple comparisons. Data are presented as mean ± standard deviation (SD) of the mean. A p values <0.05 was regarded as significant.

3. Results

3.1. Physical–chemical quality assessments

Our research results determined that all physical-chemical parameters of the examined swimming pools compliance with the Türkiye Swimming Pool Water Standards (Decree No. 28143/2011).

The physico-chemical results and national standard values of the water disinfected with different disinfectants in the regression pools examined are shown in Table 2. The recorded temperature for the five swimming pools studied in this study was kept constant

between 36 and 37°C. The pH value in the pool was found to be within the recommended range in the Türkiye National Standard (6.5-7.8) and the World Health Organization (WHO) directive (7.2-7.8). The mean alkalinity value was within the national standard range (30-80 mg/L) in all samples. All the samples showed the hardness values recommended in the national standards. It was determined that the other physical-chemical values of the pools were within the Türkiye National Standards.

Table 2. Physical-chemical analyzes of water samples taken from the examined swimming pools

<i>Parameters</i>										
<i>Pool Code</i>	<i>Temperature (°C)</i>	<i>pH (units)</i>	<i>Total Alkalinity (mg/L)</i>	<i>Biguand (mg/L)</i>	<i>Copper (Cu) (mg/L)</i>	<i>Ammonium (NH₃) (mg/L)</i>	<i>Nitrite (NO₂) (mg/L)</i>	<i>Nitrate (NO₃) (mg/L)</i>	<i>Aluminum (Al) (mg/L)</i>	<i>Hydrogen peroxide (H₂O₂)</i>
1	26–34	7.4	56	-	<0.1	<0.023	<0.014	18.56	<0.05	-
2	25–32	7.4	60	2	<0.1	<0.023	<0.014	16.79	<0.05	-
3	26–30	7.4	65	-	<0.1	<0.017	<0.017	22.6	<0.04	55
4	25–28	7.2	58	-	<0.1	<0.023	<0.014	13.05	<0.05	-
5	25–27	≥6.5 ≤7.8	180	-	-	0.50	0.50	50	200	-
<i>National standard¹</i>	26 -28	6.5-7.8	30-180	2-30	ND-1	ND-0.5	ND-0.5	ND-50	ND-0.2	40-80
<i>Method</i>		<i>TS 3263 ISO 10523</i>	<i>SM 2320 B</i>	<i>Pool tester</i>	<i>SM 3500 Cu B</i>	<i>SM 4500 NH₃ F</i>	<i>SM 4500 NO₂ B</i>	<i>SM 4500 NO₃ (E)</i>	<i>SM 3500 Al B</i>	<i>DIN 38409-15</i>

1:Chlorination, 2:Ozonation, 3:Hydrogen peroxidation,4:Silver-copper ionization, 5:Mains water.

¹: Türkiye National Standard (NO: 28143), swimming pools—general requirement.

ND: Standard value not defined.

3.2. Microbial assessments

Table 3 shows the results obtained regarding the time dependent growth of *E. coli* in the studied pools and comparing them with the Türkiye national standards. Microbiological evaluation of pool water disinfected with different disinfectants according to time was made according to the TS-EN-ISO-9308-1 method. *E. coli* growth studied throughout the study varies over time in different disinfected pools. There was no growth in the four pool water samples that were disinfected on the first day of disinfection. At the end of the fifth day, it was found that *E. coli* growth in ozonated pool water was higher than other disinfectants.

Table 3. Time-dependent microbial quality of water samples collected from the examined swimming pools

Parameters	<i>E. coli</i> (CFU/100 mL)				
Pool Code	Time (day)				
	1	2	3	4	5
1	0/3	65/1.5	68/1.2	78/1.0	100/0.2
2	0/0.6	110/0.5	140/0.4	190/0.3	300/0.1
3	0/80	40/70	37/50	45/40	70/30
4	0/0.6	80/0.4	76/0.3	110/0.2	150/0.1
National standard ¹	< 200 CFU/ml				

CFU: colony-forming units.

¹: Türkiye National Standard (NO: 28143).

1:Chlorination/ppm, 2:Ozonation/ppm, 3:Hydrogen peroxidation/ppm,4:Silver-copper ionization/ppm, 5:Mains water.

3.3. Biochemical result

In our study, free radical-mediated oxidative damage that may occur because of *in vitro* exposure of erythrocytes to residual disinfectant consisting of different disinfectants was evaluated by MDA determination method. The findings show that disinfectants used in disinfection of pool water oxidize erythrocyte membrane lipids and cause oxidative damage in lipids. In addition, lipid damage varies according to the type of disinfectant used.

In particular, the MDA level of disinfection with ozonation was found to be statistically significantly higher than the other groups except the positive control (t-BHP) ($p < 0.05$) (Table 4).

Table 4. Effects of different disinfection agents on lipid peroxidation level of erythrocytes

Group	Erythrocyte MDA (nmol/g Hb)
Main water	8.07±0.23
Hydrogen peroxidation (g/mL)	9.83±0.27 ^{a,b,c}

<i>Ozonation (g/mL)</i>	13.14±0.39 ^{a,c}
<i>Chlorination (g/mL)</i>	11.75±0.72 ^{a,b,c}
<i>Silver-copper ionization (g/mL)</i>	9.51±0.32 ^{a,b,c}
<i>t-BHP (g/mL)</i>	14.36±0.34 ^{a,c}
<i>Resveratrol (g/mL)</i>	7.17±0.18 ^{a,b}

Data represented as mean $\bar{X} \pm SD$. Comparison between the groups analysis of variance (ANOVA) p value.

- (^a): Compared with the control group,
 (^b): Compared with the hydrogen peroxidation group,
 (^c): Compared with the ozonation group,
 (^d): Compared with the chlorination group,
 (^e): Compared with the silver-copper ionization group,
 (^f): Compared with the t-BHB group is significantly different.

Statistical differences between groups were made with the Tukey post-hoc multiple comparison test. A value of $p < 0.05$ was considered statistically significant.

3.4. Comet assay assessments

DNA damage in pool water samples was determined according to different disinfection methods (Figure 1). Our analyzes showed that all disinfected pool water samples were more genotoxic than mains water. Chlorination method revealed statistically significantly higher DNA damage when compared to other disinfection methods ($p < 0.001$). The lowest DNA damage was detected in the disinfection of silver-copper ionization.

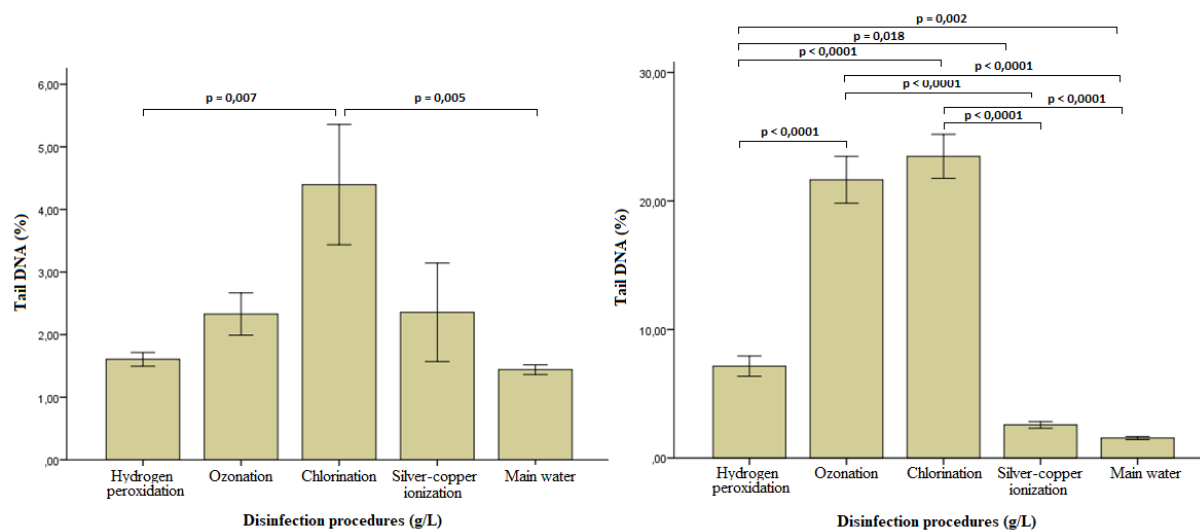


Figure 1. Comparison of time dependent genotoxicity of recreational pool water samples and mains water. First hour (A), Second hour (B). The columns in the graphs and the bars in the columns represent the mean \pm standard error ($\bar{X} \pm SD$)

4. Conclusion and Comment

In summary, the key findings in the current studies showed that the physico-chemical parameters of the regression pool water samples, in which we used different disinfection methods, were within acceptable limits recommended by national standards. Given the significant effects of regression pools on microbial safety and the health effects on users of these pools, physical-chemical parameters in regression pools should be constantly monitored. However, regression pool water samples containing *E. coli* or fecal coliform that did not meet the World Health Organization (WHO) standard indicated that pool water quality needed to be improved [22]. A comprehensive evaluation was made on the genotoxicity and oxidative stress of different disinfection types in recreational pools using the same mains water using the MDA parameter. Our data determined that all disinfected recreational pool water samples were more genotoxic than mains water. It was observed that especially disinfection with chlorination caused high genotoxicity. In our study, it was determined that the silver-copper ionization method used was the best disinfection method in terms of genotoxicity compared to other disinfection methods. It is thought that the application of different disinfection methods in the regression pool creates cytotoxicity in the cells and this causes oxidative stress. For this reason, the type of disinfection used in the pool water and the exposure time are very important. Our analyzes revealed that we should prefer silver-copper ionized pools, which have less negative effects on human health than the chemicals used in disinfection and the residual disinfectants formed by these chemicals compared to other disinfection types. In particular, our results highlighted the importance of using a combination of different bioassays to evaluate the oxidative stress and genotoxicity of water samples in different disinfection methods (chlorine, ozone, hydrogen peroxide and copper-silver ionization) commonly used in pool waters. Although swimming has anti-inflammatory, antioxidant and anti-apoptotic effects, it was concluded that the disinfectants used in regression pools and the residual disinfectants formed by them adversely affect human health.

Authorship contribution statement

Z. Bektaş: Fieldwork, Methodology, Investigation, Resource/Material Supply; **M. Şahin:** Validation, Formal Analysis, Investigation, Original Draft Writing, Review and Editing; **V. A. Toğay:** Data analysis, Formal Analysis, Investigation, Visualization; **U. Şahin:** Data Curation, Investigation, Visualization, Review and Editing; **M. Calapoğlu:** Methodology, Supervision/Observation/Advice, Project Administration.

Declaration of competing interest

The authors declare that they have no known competing financial interests or personal relationships that could have appeared to influence the work reported in this paper.

Ethics Committee Approval and/or Informed Consent Information

As the authors of this study, we declare that we do not have any ethics committee approval and/or informed consent statement.

References

- [1] J. M. Allen, M. J. Plewa, E. D. Wagner, X. Wei, G. E. Bollar, L. E. Quirk and S. D. Richardson, "Making swimming pools safer: Does copper–silver ionization with chlorine lower the toxicity and disinfection byproduct formation?," *Environmental Science & Technology*, 55(5), 2908-2918, 2021.
- [2] X. Zheng, J. Xu, Y. Gao, W. Li, Y. Chen, H. Geng and M. Xu, "Within-day variation and health risk assessment of trihalomethanes (THMs) in a chlorinated indoor swimming pool in China," *Environmental Science and Pollution Research*, 30(7), 18354-18363, 2023.

- [3] K. Yedeme, M. H. Legese, A. Gonfa, S. Girma, "Assessment of physicochemical and microbiological quality of public swimming pools in Addis Ababa, Ethiopia," *The Open Microbiology Journal*, 11, 98, 2017.
- [4] V. T. Omoni, D. N. Torjir, S. E. Okekporo, "Studies on the physicochemical and bacteriological properties of some semi-public Swimming pools in Makurdi, Nigeria," *African Journal of Microbiology Research*, 13(14), 264-272, 2019.
- [5] D. Zhang, S. Dong, L. Chen, R. Xiao, W. Chu, "Disinfection byproducts in indoor swimming pool water: Detection and human lifetime health risk assessment," *Journal of Environmental Sciences*, 126, 378-386, 2023.
- [6] R. A. Carter, S. Allard, J. P. Croué, CA. Joll, "Occurrence of disinfection by-products in swimming pools and the estimated resulting cytotoxicity," *Science of the Total Environment*, 664, 851-864, 2019.
- [7] J. De Laat, W. Feng, D. A. Freyfer, F. Dossier-Berne, "Concentration levels of urea in swimming pool water and reactivity of chlorine with urea," *Water Research*, 45(3), 1139-1146, 2011.
- [8] H. Ilyas, I. Masih, J. P. Van der Hoek, "Disinfection methods for swimming pool water: byproduct formation and control," *Water*, 10(6), 797, 2018.
- [9] V. R. Sunil, K. Patel-Vayas, J. Shen, J. D. Laskin, D. L. Laskin, "Classical and alternative macrophage activation in the lung following ozone-induced oxidative stress," *Toxicology and Applied Pharmacology*, 263(2), 195-202, 2012.
- [10] E. Procházka, B. I. Escher, M. J. Plewa, F. D. Leusch, "In vitro cytotoxicity and adaptive stress responses to selected haloacetic acid and halobenzoquinone water disinfection byproducts," *Chemical Research in Toxicology*, 28(10), 2059-2068, 2015.
- [11] J. Pals, M. S. Attene-Ramos, M. Xia, E. D. Wagner, M. J. Plewa, "Human cell toxicogenomic analysis linking reactive oxygen species to the toxicity of monohaloacetic acid drinking water disinfection byproducts," *Environmental Science & Technology*, 47(21), 12514-12523, 2013.
- [12] M. G. Muellner, M. S. Attene-Ramos, M. E. Hudson, E. D. Wagner, M. J. Plewa, "Human cell toxicogenomic analysis of bromoacetic acid: A regulated drinking water disinfection by-product," *Environmental and Molecular Mutagenesis*, 51(3), 205-214, 2010.
- [13] P. Xue, H. Wang, L. Yang, Z. Jiang, H. Li, Q. Liu, W. Qu, "NRF2-ARE signaling is responsive to haloacetonitrile-induced oxidative stress in human keratinocytes," *Toxicology and Applied Pharmacology* 450, 116163, 2022.
- [14] E. J. Daiber, D. M. DeMarini, S. A. Ravuri, H. K. Liberatore, A. A. Cuthbertson, A. Thompson-Klemish, S. D. Richardson, "Progressive increase in disinfection byproducts and mutagenicity from source to tap to swimming pool and spa water: impact of human inputs," *Environmental Science & Technology*, 50(13), 6652-6662, 2016.
- [15] T. Manasfi, M. De Meo, B. Coulomb, C. Di Giorgio, J. L. Boudenne, "Identification of disinfection by-products in freshwater and seawater swimming pools and evaluation of genotoxicity," *Environment International*, 88, 94-102, 2016.
- [16] M. Kianmehr, M. R. M. Shahri, M. Afsharnia, Z. Rohani, M. Ghorbani, "Comparison of DNA damages in blood lymphocytes of indoor swimming pool lifeguards with non-lifeguards athletes," *Mutation Research/Genetic Toxicology and Environmental Mutagenesis*, 837, 29-33, 2019.
- [17] H. K. Liberatore, E. J. Daiber, S. A. Ravuri, J. E. Schmid, S. D. Richardson, D. M. DeMarini, "Disinfection byproducts in chlorinated or brominated swimming pools and spas: Role of brominated DBPs and association with mutagenicity," *Journal of Environmental Sciences*, 117, 253-263, 2022.
- [18] Water Environmental Federation, and American Public Health Association (APHA), "Standard Methods of Water and Wastewater," American Public Health Association (APHA): Washington, DC, USA, 2005.
- [19] J. Stocks, T. L. Dormandy, "The autoxidation of human red cell lipids induced by hydrogen peroxide," *British Journal of Haematology*, 20(1), 95-111, 1971.
- [20] N. P. Singh, M. T. McCoy, R. R. Tice, E. L. Schneider, "A simple technique for quantitation of low levels of DNA damage in individual cells," *Experimental Cell Research*, 175(1), 184-191, 1988.
- [21] B. M. Gyori, G. Venkatachalam, P. S. Thiagarajan, D. Hsu, M. V. Clement, "OpenComet: an automated tool for comet assay image analysis," *Redox Biology*, 2, 457-465, 2014.
- [22] World Health Organization (WHO), "Guidelines for safe recreational water environments. Volume 2, Swimming pools and similar environments," WHO press, Switzerland, 2006, pp. 3-27.

Investigation of the Structural, Morphological, and Optical Properties of ZnBr₂-Added MAPbI₃ Perovskite Thin Films

Havva Elif Lapa^{1,*}

¹Department of Energy Systems Engineering, Graduate Education Institute, Isparta University of Applied Sciences, 32260, Isparta, TÜRKİYE

<https://orcid.org/0000-0002-5706-4641>

*corresponding author: h.eliflapa@gmail.com

(Received: 17.01.2024, Accepted: 14.06.2024, Published: 25.11.2024)

Abstract: Methylammonium lead iodide (MAPbI₃) perovskite thin films, which were pure and ZnBr₂-added at different rates (1, 3, and 5 wt%), were deposited on fluorine-doped tin oxide/titanium dioxide (FTO/TiO₂) substrates by the spin coating method. X-ray diffraction (XRD) analysis showed that the peak at ~14° was the main peak for all thin films. A shift was observed with the addition of ZnBr₂ at the main peak position. As the ZnBr₂ addition rate increased, PbI₂ peaks occurred at ~12.5°. It was seen in the scanning electron microscope (SEM) surface image that the grain sizes were larger than the others on the MAPbI₃ perovskite thin film with 5 wt% ZnBr₂ added. For MAPbI₃ perovskite thin films with 5 wt% ZnBr₂ added, the absorbance value in the visible region (from 390 to 780 nm) was higher than the others. It was observed that the band gap value (E_g) of MAPbI₃ perovskite thin films can be adjusted by adding ZnBr₂.

Key words: Advanced energy materials, Perovskite thin films, ZnBr₂ additive

1. Introduction

It is predicted that global energy consumption will reach 30 TW by 2050, and this situation reminds humanity once again of the importance of sustainable energy sources [1]. Solar energy is a sustainable and renewable energy source. Solar cells are devices that convert solar energy into electricity. The chemical formula of perovskite materials is ABX₃ (A and B are different-sized cations, and X is an anion), and these materials are used in solar cells as an active absorber layer to absorb sunlight [1, 2]. Perovskite materials have excellent optoelectronic properties, including high absorption coefficients (10^4 – 10^5 cm⁻¹), tunable band gaps (1.4–2.0 eV), long carrier diffusion lengths (\approx 175 μ m), and low exciton binding energies (<50 meV) [3–6]. Perovskite solar cells, which have a power conversion efficiency of 26.1%, are still an issue where scientists continue to work on their production and development [7].

Perovskites can easily be produced as a thin film using low-temperature solution processing methods. Methods such as dip coating, spray pyrolysis, ultrasonic spray pyrolysis, and spin coating are widely used to obtain solution-based thin films [8–13]. Although each method has advantages, researchers may prefer the spin coating method because it involves fewer complex processes and is less expensive compared to other processes. The spin coating method is a process in which the surface to be coated is covered with a thin liquid film by rotating rapidly. The liquid spreads over the substrate and forms a relatively homogeneous thin film. The viscosity and density of the fluid, rotation speed, and time have an effect on the quality, performance, and thickness of the coating. Crystallization of the structure can be achieved by applying the annealing process after the coating [14–16].

It has been reported in the literature that the crystal structure and band structure of perovskites are changed by replacing a component of ABX_3 with another ion [2]. One way to improve photovoltaic performance by reducing crystal defects and main ion migration channels at grain boundaries could be perovskite doping [17–20]. Jing et al. reported that by adding $ZnBr_2$ to $Cs_{0.05}(FA_{0.83}MA_{0.17})_{0.95}Pb_{1-x}Zn_x(I_{0.83}Br_{0.17})_3$ perovskite, grain size increased and grain boundary defects decreased. They said that with a $ZnBr_2$ additive, the perovskite film showed excellent crystallization, and the solar cell had a champion power conversion efficiency of 15.64% [17]. Zhu et al. added Zn^{2+} to $MAPbI_3$ and stated that perovskite grains increased and grain boundary defects decreased [21].

In this study, it is expected to improve both the crystal structure and grain size of the perovskite by adding $ZnBr_2$ as an additive to the $MAPbI_3$ perovskite. For this purpose, $ZnBr_2$ (1, 3, and 5 wt%) was added to $MAPbI_3$ and deposited on fluorine-doped tin oxide/titanium dioxide (FTO/ TiO_2) substrates using the spin coating method. X-ray diffraction (XRD), scanning electron microscopy (SEM), and ultraviolet-visible (UV/Vis) spectrophotometer were used to examine the effect of $ZnBr_2$ addition on the structural, morphological, and optical properties of $MAPbI_3$ perovskite thin films. There is no known study in the literature on the examination of the structural, morphological, and optical properties of $MAPbI_3$ perovskites added with $ZnBr_2$.

2. Material and Method

FTO coated substrates are commercially available. FTO substrates with dimensions of $2.0\text{ cm} \times 2.0\text{ cm} \times 0.2\text{ cm}$ were ultrasonically cleaned with detergent, distilled water, and ethanol before being coated with TiO_2 . The solution prepared for the TiO_2 layer contains 2.5 mL of titanium tetraisopropoxide (TTIP), 2 mL of acetyl acetone, and 11 mL of ethanol. The solution was stirred for 30 minutes at room temperature in a glovebox on a magnetic stirrer. TiO_2 surfaces were coated with hand spray. The spray process was repeated 15 times at 30 second intervals from a height of $\sim 15\text{ cm}$. The substrate temperature was $475\text{ }^\circ\text{C}$, and the substrates were annealed at $525\text{ }^\circ\text{C}$ for 1 hour on a magnetic heater after coating. Thus, the production of FTO/ TiO_2 substrates has been completed. The perovskite layers were deposited on the FTO/ TiO_2 substrates because they had higher adherence than the bare soda lime glass.

Methylammonium iodide (MAI, Luminescence Technology) and lead iodide (PbI_2 , Sigma-Aldrich) (1:1 M) were dissolved using dimethyl sulfoxide (DMSO) and *n,n*-dimethylformamide (DMF) (1:4). $ZnBr_2$ was added to the solution in certain proportions (1, 3, and 5 wt%). The perovskite solutions were stirred for 40 minutes at $50\text{ }^\circ\text{C}$ in a glovebox by using a magnetic stirrer. After the solutions were cooled to room temperature, $80\text{ }\mu\text{L}$ of the solution were dropped on the substrate. The perovskite solution was coated on the substrates by the spin coating method by rotating at 4000 rpm for 30 seconds. 100 mL of chlorobenzene (CB) anti-solvent was dropped at the 15th second of the coating. It is known that the key to producing efficient solar cells is the crystallization quality of the perovskite film. The crystallinity of perovskites in solar cells plays an important role in efficient carrier photo-generation, charge separation at contact, and the transfer of separated charges. During spin coating, anti-solvent can be dripped onto the perovskite film to precipitate salts in solution. Thus, smooth and compact thin films can be obtained [22]. It has been seen that CB is used as an anti-solvent in many studies in the literature in the production of $MAPbI_3$ perovskite films [12, 23-25]. Then, the substrates were annealed at $120\text{ }^\circ\text{C}$ in a nitrogen environment for 20 minutes. The schematic representation for spin coating is given in Figure 1.

XRD measurements of the thin films were taken in the range of $10^\circ \leq 2\theta \leq 60^\circ$ using the Cu K α radiation ($\lambda=1.5418 \text{ \AA}$) of a Bruker D8 Advance Twin-Twin diffractometer (40 kV, 40 mA). The surface morphologies of the films were observed by SEM (FEI Quanta FEG 250). The thickness of all thin films was determined by using cross-section SEM images. The optical absorption studies of thin films were carried out with a UV-Vis-NIR Spectrophotometer (JASCO V-770 UV-Vis-NIR) operated at room temperature.

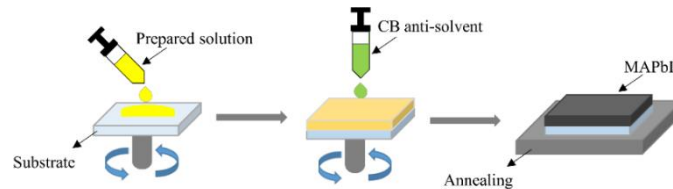


Figure 1. Schematic illustration for spin coating

3. Results

The XRD patterns of MAPbI₃ perovskite thin films in the ranges of $10^\circ \leq 2\theta \leq 60^\circ$ and $12^\circ \leq 2\theta \leq 15^\circ$ are given in Figures 2(a) and (b), respectively. According to prior research, the principle MAPbI₃ peaks at 2θ of $\sim 14^\circ$ (110), $\sim 28^\circ$ (220), and $\sim 32^\circ$ (310) (black line in Figure 2(a)) confirmed the production of the MAPbI₃ perovskite film [26, 27].

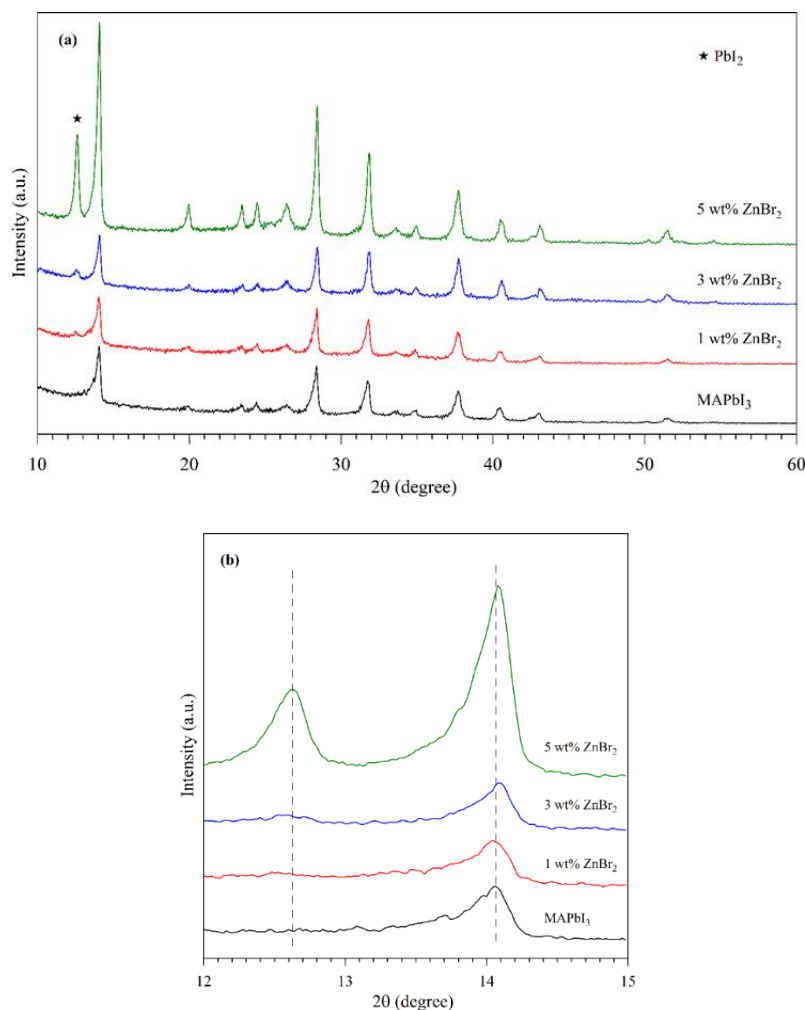


Figure 2. XRD patterns of pure, and 1, 3, and 5 wt% ZnBr₂ additive MAPbI₃ perovskite thin films (a) $10^\circ \leq 2\theta \leq 60^\circ$ (b) $12^\circ \leq 2\theta \leq 15^\circ$

It was observed that the peak intensities of pure MAPbI₃ perovskites changed with the addition of ZnBr₂ to the perovskite structure. The peak intensity of ~14° (110) in 2θ is higher than the others and is considered the main peak. The average crystallite size (*D*) of perovskite thin films can be calculated using the Scherrer equation, given below [28]:

$$D = \frac{0.94\lambda}{\beta \cos\theta} \quad (1)$$

In this equation, θ is the diffraction angle of the maximum intensity peak, β is the half peak width (in radians) of the maximum intensity peak, and λ is the X-ray wavelength. The crystal sizes of perovskite thin films were calculated using EVA software on Bruker's D8 Advance Twin-Twin device from the FWHM (full width at half maximum) values of the main peak (given in Table 1). It was observed that the crystal sizes of perovskite thin films added with 3 wt% and 5 wt% ZnBr₂ were almost the same and had higher values than the others. The (110) peak of these perovskites has a higher density and a smaller peak width than the others (given in Figure 2(b)). It has also been reported in the literature that this will cause a high degree of crystallinity [26]. With the addition of ZnBr₂ to MAPbI₃ perovskite thin films, peak formation is observed at approximately 12.5° (given in Figures 2(a) and (b)). This peak belongs to PbI₂ [27]. The number of positive metal cations increases with ZnBr₂ doping. This situation causes deviations in stoichiometry. While Zn ions enter the perovskite structure, Pb ions remain outside. These Pb ions appear as PbI₂ peaks in the XRD pattern. Similar situations were observed when MAPbI₃ was doped with Li, Sn, and Mg [29-31].

Table 1. Crystal size of pure, and 1, 3, and 5 wt% ZnBr₂ additive MAPbI₃ perovskite thin films

Perovskites	Crystallite size (Å)
MAPbI ₃	315
1 wt% ZnBr ₂	300
3 wt% ZnBr ₂	328
5 wt% ZnBr ₂	326

The addition of ZnBr₂ did not modify the original crystal phase of the MAPbI₃ perovskite, according to XRD measurements (given in Figures 2(a) and (b)). The XRD peak intensity of the perovskite film additive with 5 wt% ZnBr₂ is the highest. This may be due to the fact that the amount of material deposited on the surface is higher than the others. As shown in Figure 2(b), the XRD peak of ZnBr₂ additive perovskite (especially for 3 wt% and 5 wt%) shifted to the right when compared to perovskite without ZnBr₂ additive. The ionic radius of Zn⁺² (~74 pm) is smaller than Pb⁺² (~119 pm). The Pb substitution of Zn ions can reduce the interplanar spacing of the perovskite crystals. In this case, the Bragg angle shifts with the ZnBr₂ doping [17, 21]. Similar results have been reported in the literature [17, 21, 32].

Figures 3(a)–(d) show surface-SEM images of pure, 1, 3, and 5 wt% ZnBr₂ additive MAPbI₃ perovskite thin films (at 50.000× magnification). It can be seen from surface-SEM images that the substrate surfaces are covered with reticulated structures. Figure 3 shows that the grain size increases with the addition of ZnBr₂ to MAPbI₃ perovskites. Especially in MAPbI₃ perovskites with 5 wt% ZnBr₂ added, it is clearly seen that the grain sizes are larger than the others. It is known that by doping a small-radius metal into the perovskite lattice (e.g., In³⁺, Sb³⁺, Ca²⁺, and Sr²⁺), the crystal structure can be adjusted and its optoelectronic properties can be improved [17, 32, 33]. For thiourea and caffeine-additive MAPbI₃, the increase in grain size has been reported in previous studies [19, 20]. Moreover, it has been found in the literature that Zn⁺² is doped with MAPbI₃ in order to reduce grain boundary defects and obtain high-quality and high-performance MAPbI₃ [21].

Figures 4(a)–(d) illustrated cross-section SEM images of pure, and 1, 3, and 5 wt% ZnBr_2 additive MAPbI_3 perovskite thin films (at 100.000 \times magnification), respectively. The average thickness of commercial FTO coated substrates was determined as ~ 385 nm from the cross-section SEM image. The boundaries of the layers were drawn from the color contrasts in the cross-section SEM images. However, there is no clear boundary separating the TiO_2 layer and all the MAPbI_3 perovskite layers in Figures 4(a)–(d). The total thicknesses of pure, and 1, 3, and 5 wt% ZnBr_2 additive MAPbI_3 thin films and TiO_2 layers were found to be 254, 227, 343, and 402 nm, respectively.

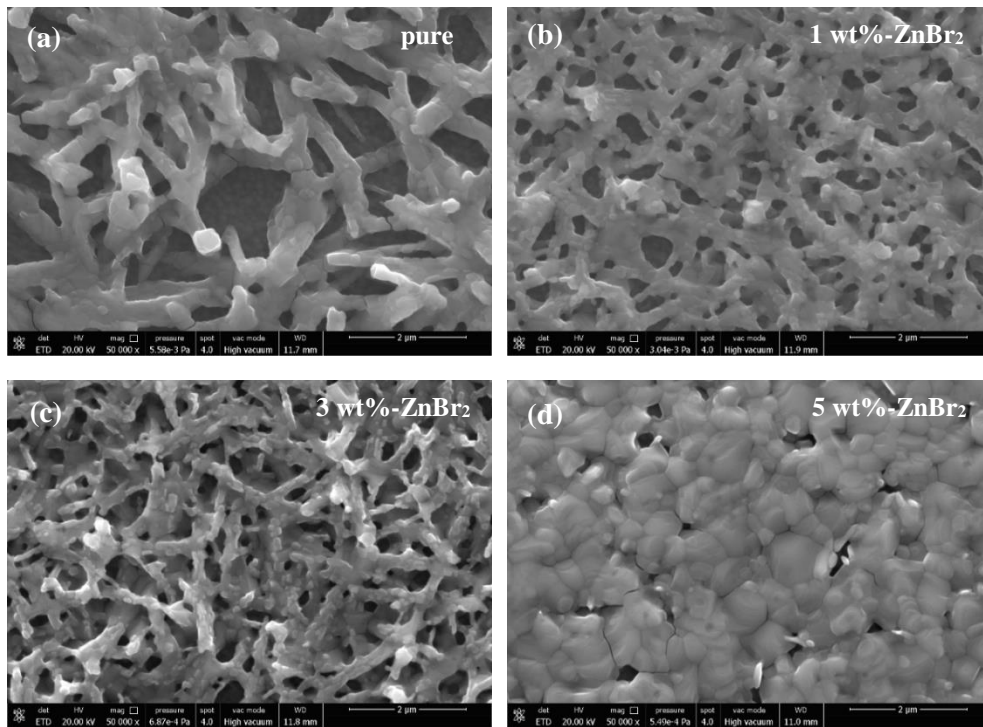


Figure 3. Surface-SEM images of (a) pure (b) 1 wt% (c) 3 wt% (d) 5 wt% ZnBr_2 additive MAPbI_3 perovskite thin films

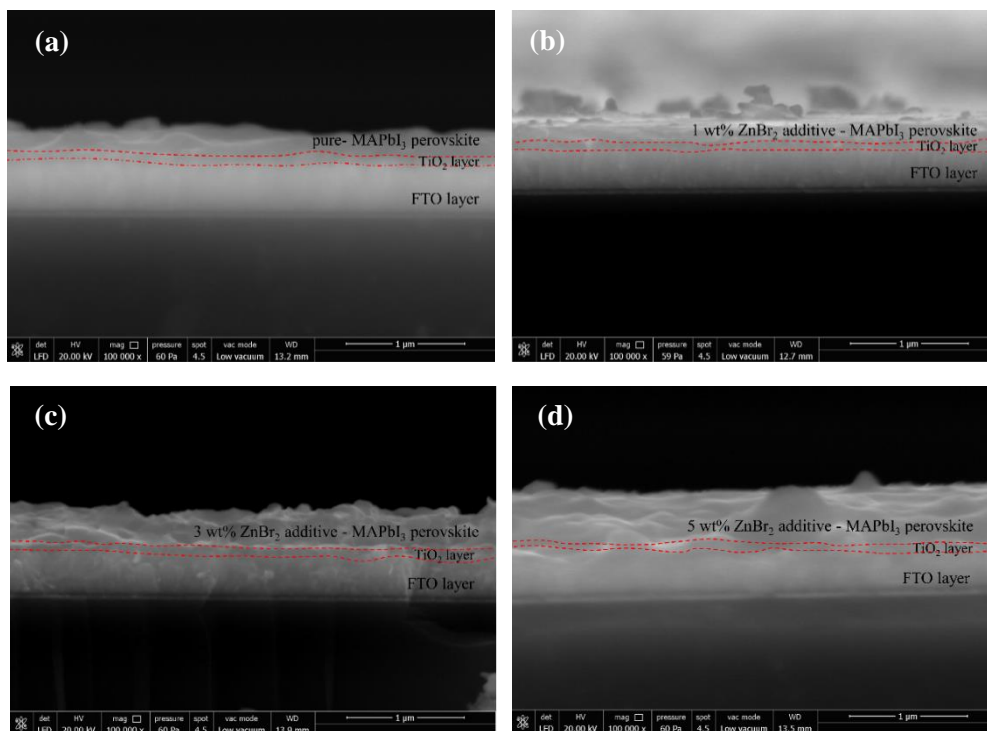


Figure 4. Cross-section SEM images of (a) pure (b) 1 wt% (c) 3 wt% (d) 5 wt% ZnBr_2 additive MAPbI_3 perovskite thin films

Optical transmittance measurements of pure MAPbI₃ and ZnBr₂ added MAPbI₃ perovskite thin films were performed in the wavelength range of 290–1100 nm. The relationship between optical transmittance (T) and absorption (A) is given in the following equation [34]:

$$A = 2 - \log(\%T) \quad (2)$$

The wavelength dependent curves of the absorbance (in the visible range (from 390 to 780 nm)) of all perovskite thin films are shown in Figure 5(a). 5 wt% ZnBr₂ additive MAPbI₃ thin films show the highest absorbance value. The increase in crystal and grain size may cause an increase in light absorption.

The relationship between the optical band gap and the absorption coefficient is given in the following equation [35]:

$$\alpha h\nu = B(h\nu - E_g)^n \quad (3)$$

Here, α is the absorption coefficient, h is the Planck's constant, ν is the frequency of the incident photon, B is an energy independent constant, and E_g is the semiconductor's forbidden band gap. The n is equal to 1/2 for semiconductors with a direct band gap. The Tauc curve is obtained by plotting $(\alpha h\nu)^2$ versus $h\nu$, and the E_g value can be calculated from the point where this curve intersects the x -axis. The Tauc curves of all produced perovskite thin films are shown in Figure 5(b).

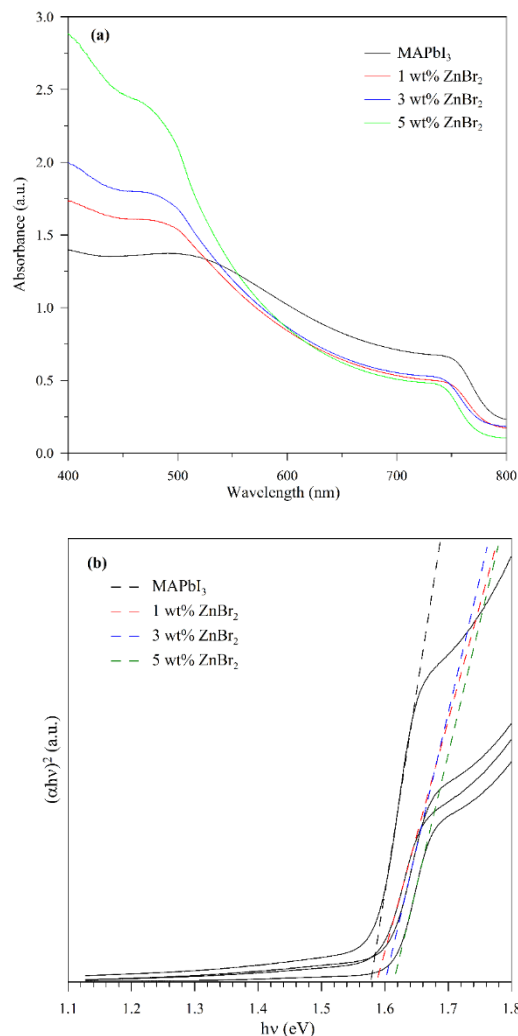


Figure 5. (a) Transmittance – wavelength plots (b) Tauc curves for pure, and 1, 3, and 5 wt% ZnBr₂ additive MAPbI₃ perovskite thin films

For MAPbI₃ perovskite thin films, E_g was obtained as 1.58 eV. This value is in agreement with the literature [36-39]. The E_g values of 1, 3, and 5 wt% ZnBr₂ added MAPbI₃ perovskite thin films were calculated as 1.59 eV, 1.60 eV, and 1.61 eV, respectively. It is seen that the band gap of MAPbI₃ perovskite thin films can be slightly changed by the addition of ZnBr₂. Such tunability of the band gap is advantageous for the development of a new material platform for optoelectronic applications of perovskite materials. However, it is not expected to observe an increase in efficiency due to the band gap alteration in applications containing ZnBr₂-additive MAPbI₃.

4. Conclusion

The spin coating method was used to deposit pure MAPbI₃ and ZnBr₂-added (1, 3, and 5 wt%) MAPbI₃ perovskite thin films on FTO/TiO₂ substrates. Thin films exhibited the characteristic XRD peaks belonging to MAPbI₃ perovskite. As the ZnBr₂ addition rate increased, a PbI₂ peak was observed at ~12.5°. The presence of these peaks was attributed to PbI₂, which is not included in the MAPbI₃ perovskite structure with the addition of ZnBr₂. The main peak position at $2\theta \cong 14^\circ$ in the XRD pattern changed with the addition of ZnBr₂. The grain sizes of MAPbI₃ perovskites grew as the ZnBr₂ addition rate increased, as seen on the surface SEM images. It was observed that both pure and ZnBr₂-added MAPbI₃ perovskites exhibited high crystal size and large grains compared to the literature [19, 20]. The E_g of MAPbI₃ perovskite thin films can be changed with the addition of ZnBr₂ (from 1.58 eV to 1.61 eV). The addition of ZnBr₂ to MAPbI₃ perovskite thin films is effective in increasing the crystal and grain sizes as well as changing the band gap. Increasing the crystal and grain sizes may be advantageous for increasing efficiency in solar cell applications. Thus, ZnBr₂ additive MAPbI₃ perovskite thin films may be preferred as the active layer for absorbing sunlight in solar cells. However, it is predicted that a small change in the band gap due to the ZnBr₂ additive will not contribute to efficiency. The emergence of the PbI₂ peak is an undesirable situation. The presence of unreacted PbI₂ negatively affects the stability of the perovskite material. In further studies, the stoichiometry can be achieved by reducing the PbI₂ ratio.

Authorship contribution statement

H.E. Lapa: Data Curation, Original Draft Writing, Methodology.

Declaration of competing interest

The author declares that they have no known competing financial interests or personal relationships that could have appeared to influence the work reported in this paper.

Acknowledgment

No financial support was received for the present study.

Ethics Committee Approval and/or Informed Consent Information

As the author of this study, I declare that I do not have any ethics committee approval and/or an informed consent statement.

References

- [1] B. Dahal and W. Li, "Configuration of methylammonium lead iodide perovskite solar cell and its effect on the device's performance: A review", *Advanced Materials Interfaces*, 9, 2200042, 2022.

- [2] S. Khatoon, S. K. Yadav, V. Chakravorty, J. Singh, R. B. Singh, M. S. Hasnain and S. M. M. Hasnain, "Perovskite solar cell's efficiency, stability and scalability: A review", *Materials Science for Energy Technologies*, 6, 437-459, 2023.
- [3] T. Baikie, Y. Fang, J. M. Kadro, M. Schreyer, F. Wei, S. G. Mhaisalkar, M. Graetzel and T. J. White, "Synthesis and crystal chemistry of the hybrid perovskite (CH₃NH₃)PbI₃ for solid-state sensitised solar cell applications", *Journal of Materials Chemistry A*, 1(18), 5628-5641, 2013.
- [4] B. Saparov and D. B. Mitzi, "Organic-inorganic perovskites: Structural versatility for functional materials design", *Chemical Reviews*, 116, 4558-4596, 2016.
- [5] S. D. Stranks, G. E. Eperon, G. Grancini, C. Menelaou, M. Alcocer, T. Leijtens, L. M. Herz, A. Petrozza and H. J. Snaith, "Electron-hole diffusion lengths exceeding 1 micrometer in an organometal trihalide perovskite absorber", *Science*, 342(6156), 341-344, 2013.
- [6] H. E. Lapa, A. Çalık, M. Kaleli and D. A. Aldemir, "Investigation of stability for Cs₂TiBr₆ perovskite materials exposed to air environment", *Physica Scripta*, 98(6), 065805, 2023.
- [7] NREL: Efficiency chart (2023). [Online]. Available: <https://www.nrel.gov/pv/cell-efficiency.html> (ie.25.08.2023)
- [8] C. A. Rico-Yuson, S. Danwittayakul, S. Kumar, G. L. Hornyak and T. Bora, "Sequential dip-coating of CsPbBr₃ perovskite films in ambient conditions and their photovoltaic performance", *Journal of Materials Science*, 57, 10285-10298, 2022.
- [9] L. H. Chou, J. M. W. Chan and C. L. Liu, "Progress in spray coated perovskite films for solar cell applications", *Solar RRL*, 6(4), 2101035, 2022.
- [10] H. E. Lapa, "The effect of illumination on p-n junction diodes based on Yb-doped CuO thin films produced by ultrasonic spray pyrolysis method", *Journal of Materials Science: Materials in Electronics*, 34(5), 425, 2023.
- [11] M. Shahiduzzaman, K. Yamamoto, Y. Furumoto, T. Kuwabara, K. Takahashi and T. Taima, "Ionic liquid-assisted growth of methylammonium lead iodide spherical nanoparticles by a simple spin-coating method and photovoltaic properties of perovskite solar cells", *Rsc Advances*, 5(95), 77495-77500, 2015.
- [12] R. Lu, Y. Liu, J. Zhang, D. Zhao, X. Guo and C. Li, "Highly efficient (200) oriented MAPbI₃ perovskite solar cells", *Chemical Engineering Journal*, 433, 133845, 2022.
- [13] M. Kaleli, E. Şen, H. E. Lapa and D. A. Aldemir, "The production route of the MASnBr₃ based perovskite solar cells with fully ultrasonic spray pyrolysis method", *Physica B: Condensed Matter*, 645, 414293, 2022.
- [14] N. Sahu, B. Parija and S. Panigrahi, "Fundamental understanding and modeling of spin coating process: A review", *Indian Journal of Physics*, 83(4), 493-502, 2009.
- [15] L. E. Scriven, "Physics and applications of DIP coating and spin coating", *MRS Online Proceedings Library (OPL)*, 121, 717729, 1988.
- [16] H. E. Lapa, "Altaş sıcaklığına bağlı olarak ultrasonik sprey piroliz yöntemi ile üretilen CuO ince filmlerin incelenmesi", *Süleyman Demirel University Faculty of Arts and Science Journal of Science*, 17(1), 195-208, 2022.
- [17] Y. Jing, Y. Lv, K. Wang, Z. Xu and X. Zhou, "Acquiring high-performance and commercially available carbon based air-stable perovskite solar cells by using ZnBr₂ additive", *Journal of Alloys and Compounds*, 930, 167445, 2023.
- [18] J. I. Kim, Q. Zeng, S. Park, H. Lee, J. Park, T. Kim and T. W. Lee, "Strategies to extend the lifetime of perovskite downconversion films for display applications", *Advanced Materials*, 2209784, 2023.
- [19] R. Wang, J. Xue, L. Meng, J. W. Lee, Z. Zhao, P. Sun, L. Cai, T. Huang, Z. Wang, Z. K. Wang, Y. Duan, J. L. Yang, S. Tan, Y. Yuan, Y. Huang and Y. Yang, "Caffeine improves the performance and thermal stability of perovskite solar cells", *Joule*, 3(6), 1464-1477, 2019.
- [20] C. Fei, B. Li, R. Zhang, H. Fu, J. Tian and G. Cao, "Highly efficient and stable perovskite solar cells based on monolithically grained CH₃NH₃PbI₃ film", *Advanced Energy Materials*, 7(9), 1602017, 2017.
- [21] X. Y. Zhu, M. W. Chen, B. Wang, N. Liu, M. Q. Ran, H. Yang and Y. P. Yang, "Improved photovoltaic properties of nominal composition CH₃NH₃Pb_{0.99}Zn_{0.01}I₃ carbon-based perovskite solar cells", *Optics Express*, 26(26), A984-A995, 2018.
- [22] M. Konstantakou, D. Perganti, P. Falaras and T. Stergiopoulos, "Anti-solvent crystallization strategies for highly efficient perovskite solar cells", *Crystals*, 7(10), 291, 2017.

- [23] M. Xiao, F. Huang, W. Huang, Y. Dkhissi, Y. Zhu, J. Etheridge, A. Gray-Weale, U. Bach, Y. B. Cheng and L. Spiccia, "A fast deposition-crystallization procedure for highly efficient lead iodide perovskite thin-film solar cells", *Angewandte Chemie International Edition*, 53(37), 9898-9903, 2014.
- [24] H. Li, Y. Xia, C. Wang, G. Wang, Y. Chen, L. Guo, D. Luo and S. Wen, "High-efficiency and stable perovskite solar cells prepared using chlorobenzene/acetonitrile antisolvent", *ACS Applied Materials & Interfaces*, 11(38), 34989-34996, 2019.
- [25] S. Bouazizi, A. Bouich, W. Tlili, M. Amlouk, A. Omri, B. M. Soucase, "Methylammonium lead triiodide perovskite-based solar cells efficiency: Insight from experimental and simulation", *Journal of Molecular Graphics and Modelling*, 122, 108458, 2023.
- [26] Z. S. Almutawah, S. C. Wathage, Z. Song, R. H. Ahangharnejhad, K. K. Subedi, N. Shrestha, A. B. Phillips, Y. Yan, R. J. Ellingson and M. J. Heben, "Enhanced grain size and crystallinity in $\text{CH}_3\text{NH}_3\text{PbI}_3$ perovskite films by metal additives to the single-step solution fabrication process", *MRS Advances*, 3, 3237-3242, 2018.
- [27] P. Basumatary and P. Agarwal, "Photocurrent transient measurements in MAPbI_3 thin films", *Journal of Materials Science: Materials in Electronics*, 31, 10047-10054, 2020.
- [28] B.D. Cullity, *Elements of X-ray diffraction*, Addison-Wesley Publishing, Boston, 1956.
- [29] Y. Li, P. Lv, C. Li, F. Xu, J. Jia and B. Cao, "Heterostructural perovskite solar cell constructed with Li-doped p- $\text{MAPbI}_3/\text{n-TiO}_2$ PN junction", *Solar Energy*, 226, 446-454, 2021.
- [30] S. Wang, K. Zhao, Y. Shao, L. Xu, Y. -P. Huang and W. Li, "Evolutions of optical constants, interband electron transitions, and bandgap of Sn-doped $\text{CH}_3\text{NH}_3\text{PbI}_3$ perovskite films", *Applied Physics Letters*, 116, 261902, 2020.
- [31] F. Yang, M. A. Kamarudin, G. Kapil, D. Hirotani, P. Zhang, C. H. Ng, T. Ma and S. Hayase, "Magnesium-doped MAPbI_3 perovskite layers for enhanced photovoltaic performance in humid air atmosphere", *ACS Applied Materials & Interfaces*, 10, 24543-24548, 2018.
- [32] B. Luo, F. Li, K. Xu, Y. Guo, Y. Liu, Z. Xia and J. Z. Zhang, "B-Site doped lead halide perovskites: synthesis, band engineering, photophysics, and light emission applications", *Journal of Materials Chemistry C*, 7(10), 2781-2808, 2019.
- [33] H. W. Qiao, S. Yang, Y. Wang, X. Chen, T. Y. Wen, L. J. Tang, Q. Cheng, Y. Hou, H. Zhao and H. G. Yang, "A gradient heterostructure based on tolerance factor in high-performance perovskite solar cells with 0.84 fill factor", *Advanced Materials*, 31(5), 1804217, 2019.
- [34] H. Ali, F. Bensaali and F. Jaber, "Novel approach to non-invasive blood glucose monitoring based on transmittance and refraction of visible laser light", *IEEE Access*, 5, 9163-9174, 2017.
- [35] J. Tauc, R. Grigorovici and A. Vancu, "Optical properties and electronic structure of amorphous germanium", *Physica Status Solidi (B)*, 15(2), 627-637, 1966.
- [36] B. A. Al-Asbahi, S. M. H. Qaid, M. Hezam, I. Bedja, H. M. Ghaithan and A. S. Aldwayyan, "Effect of deposition method on the structural and optical properties of $\text{CH}_3\text{NH}_3\text{PbI}_3$ perovskite thin films", *Optical Materials*, 103, 109836, 2020.
- [37] V. M. Caselli, Z. Wei, M. M. Ackermans, E. M. Hutter, B. Ehrler and T. J. Savenije, "Charge carrier dynamics upon sub-bandgap excitation in methylammonium lead iodide thin films: Effects of Urbach tail, deep defects, and two-photon absorption", *ACS Energy Letters*, 5(12), 3821-3827, 2020.
- [38] P. Singh, R. Mukherjee and S. Avasthi, "Acetamidinium-substituted methylammonium lead iodide perovskite solar cells with higher open-circuit voltage and improved intrinsic stability", *ACS Applied Materials & Interfaces*, 12(12), 13982-13987, 2020.
- [39] K. Dhivyaprasath and M. Ashok, "Degradation behavior of methylammonium lead iodide ($\text{CH}_3\text{NH}_3\text{PbI}_3$) perovskite film in ambient atmosphere and device", *Solar Energy*, 255, 89-98, 2023.

Effectiveness of a Novel CTGF LNA GapmeR Sequence in Gastric Cancer Cells

Deniz Sezlev Bilecen¹

¹Department of Molecular Biology and Genetics, Faculty of Agriculture and Natural Sciences, Konya Food and Agriculture University, 42080, Konya, TURKEY

<https://orcid.org/0000-0002-5708-2276>

(Received: 25.11.2023, Accepted: 04.07.2024, Published: 25.11.2024)

Abstract: Gastric cancer is the third most common cause of malignancy worldwide and the prognosis is poor due to drug resistance and molecular diversity of the disease. Therefore, development of novel therapies is required. Connective Tissue Growth Factor (CTGF) is involved in the extracellular matrix production, cell proliferation and migration which makes it a target for the treatment of disease. Nucleic acid-based therapies are used to reduce the expression of specific mRNA sequences. The purpose of this study was to reduce the migration, and proliferation of gastric cancer cells through the inhibition of CTGF expression. On this purpose, a novel locked nucleic acid GapmeR sequence was identified as an inhibitor of CTGF expression, and the effectiveness of the sequence was shown in the gastric cancer cells. The gastric adenocarcinoma cells were transfected with GapmeR and changes in gene expressions of CTGF and collagen type I (COL1A1) were studied by qRT-PCR. The CTGF protein levels and proliferation were studied by Western Blot analysis and Alamar Blue Assay. The sequence caused significant reductions in CTGF and COL1A1 mRNA levels and proliferation of cells. These results might lead to the development of delivery system towards gastric cancer cells by using this sequence.

Key words: Gastric Cancer, LNA GapmeR, CTGF

1. Introduction

Gastric cancer is the fifth most common diagnosed cancer and third most common malignancy globally. The primary cause of gastric cancer development is chronic *Helicobacter pylori* infection [1,2]. Depending on the metastatic property of the developed cancer, different treatment approaches such as chemotherapy, chemoradiation, fluoropyrimidines, platinum, taxanes, irinotecan or immunotherapy are being used [3].

However, acquired drug resistance and the molecular and phenotypic diversity within tumors [4] cause the verification of prognosis among patients [5]. Therefore, identification of new targets, therapeutic agents and effective therapies are crucial towards developing alternative treatment strategies to improve the survival rate of gastric cancer patients.

Connective tissue growth factor (CTGF) which is also known as cellular communication network factor 2 (CCN2), is a member of CCN family secretory proteins including cysteine-rich protein 61 (CCN1), nephroblastoma-overexpressed gene (CCN3), Wisp-1/elm1 (CCN4), Wisp-2/rCop1 (CCN5) and Wisp-3 (CCN6) [6,7].

Under normal physiological conditions, CTGF is involved in embryonic development, wound healing and tissue repair [8]. However, cancer research has revealed that, abnormal expression of CTGF leads to development and progression of tumors in various

tissues such as lung, prostate, and breast; through the induction of cell proliferation, migration, invasion and metastasis [9]. CTGF also supports fibrotic and inflammatory tumor microenvironment which induces malignancy and metastasis [10]. In the literature it is stated that the overexpression of CTGF in gastric cancer patients, led to a higher incidence of lymph node metastasis and lower cumulative 5-year survival rate [11].

ECM proteins in tissue microenvironment play critical roles in cancer progression and invasion. The ability of cancer cells to leave the original tissue, invade and locate into the metastatic niches is known to be related to the extracellular matrix (ECM) composition and remodeling rate of the tumor microenvironment [12]. ECM remodeling at the tumor microenvironment takes place with the combined actions of increased levels of ECM remodeling enzymes (namely matrix metalloproteinases, MMPs), their tissue inhibitors and elevated collagen deposition. MMP proteins are known to be important mediators of ECM degradation and thus they contribute to the disruption of basement membrane and particularly the increased expression of MMP-9 in gastric carcinoma tissues is associated with the depth of cancer invasion [13]. In addition to MMPs, the expression of other ECM components such as collagen are elevated in gastric cancer tissues [14,15]. Abnormal cell-cell adhesion, increased collagen expression leading to ECM stiffness, increased matrix metalloproteinase (MMP) activity inducing ECM disruption and remodeling result in cancer cell invasion [16].

Studies performed by using gastric adenocarcinoma cells revealed that MMP-9 and collagen gene expressions are elevated in gastric cells and are related to CTGF expression [17]. The overexpression of COL1A1 in gastric cells is known to promote invasion and migration of the cells in addition to their increased proliferation rate. Moreover, miRNA associated suppression of these genes, inhibited their proliferation, invasion, and migration [17,18]. It is also demonstrated that, the inhibition of MMP-9 expression resulted in reduced migration, invasion and growth of gastric cancer cells [19]. Therefore, development of therapeutic approaches addressing the reduction of increased ECM proteins such as MMP-9 and COL1A1 might be promising for reducing migration, invasion and proliferation of gastric cancer cells.

In the literature it is stated that the knockdown of high CTGF expression in gastric cancer cells reduces MMP-9 expression in both mRNA and protein levels. Also, the restoring of CTGF levels through conditioned media reversed that reduction suggesting that MMP-9 expression is correlated with CTGF levels in the cells [20].

It is also known that collagen, being the main component in the ECM of tumors, is a substrate of MMPs and is also recognized as tumor-related gene [21]. Moreover, CTGF acts as a downstream mediator of TGF- β and increases the collagen type I deposition in tumor microenvironment [22]. The knockdown of COL1A1 was shown to be associated with low cell migration, invasion and proliferation of gastric cancer cells. Although not performed with gastric cancer cells, it is worth mentioning that the CTGF knockdown caused reduced COL1A1 expression in hepatocarcinoma spheroids [22]. In particular, CTGF overexpression in gastric cancer cells leads to enhanced cell migration and thus metastasis by inducing nuclear factor kappa-light-chain-enhancer of activated B cells (NF- κ B) signaling pathway. In addition, the elevated collagen expression is known to be related with tumor enlargement in gastric cancer [23]. Taking all this information together, CTGF may be considered as a potential target for the treatment of gastric cancer. The purpose of the study is to reduce CTGF levels in gastric cancer cells so that the reduction might potentially lead to suppression of collagen and MMP expressions, thus ultimately reduce cell migration, invasion, and tumor enlargement.

The use of nucleic acids as therapeutics is an emerging field. Antisense oligonucleotide (AON) based therapies have been studied in several cancer states. There are also several clinical trials with these therapeutics [24]. The therapeutic action of AON relies on the ability of specific nucleic acid sequences to modulate the expression of target mRNA. AONs are single-stranded 16 to 21-mer long sequences which function either by degrading the mRNA (through RNase H activity), by modifying the splicing of mRNA or by sterically blocking the translation of mRNA. The use of AON as it is, has some limitations such as poor cellular penetration, easy degradation by nucleases and possible toxicity due to degradation products of AONs which might possess antiproliferative effects [24,25]. Therefore, numerous modifications have been implemented to overcome these limitations. These modifications have led to the emergence of three different types of AONs known as the first, second and third generation AONs.

The “Antisense locked nucleic acid (LNA) GapmeR” used in this study, falls under the category of third generation AONs. It is a 16 nucleotide long single-stranded antisense oligonucleotide that induces RNase H activity. The flanking regions (both 5' and 3') are modified with LNA and the central region is composed of LNA-free DNA nucleotide. The central region is responsible for inducing the RNase H activity and the LNA flanking regions increase the targeting efficiency. It has a fully phosphorothioate (PS) modified backbone to increase the resistance to enzymatic degradation.

In this study, the custom designed and synthesized Antisense LNA GapmeR was investigated in terms of its effectiveness in suppressing CTGF expression in gastric cancer cells. The possible outcome of CTGF inhibition was also studied by analyzing COL1A1 and MMP-9 mRNA expressions along with the changes in the proliferation of gastric cancer cells.

2. Material and Method

2.1. Cell culture conditions

Human gastric adenocarcinoma cell line, AGS (American Type Culture Collection, ATCC CRL-1739) was a kind gift from the laboratory of Prof. Nazlı Arda (Istanbul University, Turkey). This commercially available cell line which exhibits epithelial-like morphology was isolated in 1979 from the stomach tissue of a 54-year-old, Caucasian, female patient with gastric adenocarcinoma with no prior anti-cancer treatment. The cells were cultured under normal conditions (37 °C, 5% CO₂) in RPMI medium, supplemented with 10% FBS, penicillin/streptomycin (1%) and 2 mM L-glutamine.

2.2. GapmeR sequences and transfection studies

The CTGF mRNA specific GapmeR sequence was custom designed by Qiagen with the product number LG00789631. The scrambled negative control was also purchased from Qiagen (LG00000002). For the transfection studies, a commercially available transfection reagent, HiPerFect Transfection Reagent (HP) (Qiagen, Germany) was used with a fast forward transfection technique, as follows.

For gene expression studies, HP (3 µL) was diluted in OptiMem™ Reduced Serum Medium (100 µL) and then mixed with AON sequences (10 µM, 1.5 µL). The mixture was incubated for 10 min for complete complexation of AON sequences with HP. Meanwhile, AGS cells (1.2x10⁵ cells) were seeded in 12 well plates. At the end of incubation, the HP-AON complexes were added onto the cell suspension within the 12 well plates and the medium was completed to 500 µL with a 1:1 (v/v) OptiMem™: RPMI

full medium. Gene silencing was monitored at 48 h, post transfection. Cells that are not treated with any type of AON were used as a control group for the experiment.

For protein expression analysis studies, HP (12 μ L) was diluted in OptiMemTM medium, mixed with AON (10 μ M, 6 μ L) and incubated for 10 min. The HP-AONs complexes were added dropwise onto AGS cell suspension (6×10^5 cells) in 6-well plates. The final volume was completed to 2.5 mL with 1:1 (v/v) OptiMemTM and RPMI full mediums. The cells that were not treated with AON sequences were used as a control group for the experiment.

2.3. Gene expression studies

In order to determine the efficiency of AON sequence to knockdown CTGF gene expression and the indirect effects of CTGF downregulation on the AGS cells, quantitative real time PCR (qRT-PCR) was performed (CFX96 Touch Real Time PCR System, BioRad). The primer pairs used for the study are given in Table 1.

Table 1. qRT-PCR primer pairs and the amplicon sizes

	Primers (5' - 3')	Sequence	Amplicon Size (bp)
CTGF	Forward	GAAGAGAACATTAAGAAGGGCAAA	97
	Reverse	ATGTCTTCATGCTGGTGCAG	
Collagen Type I	Forward	GTTGTGCGATGACGTGATCTGTGA	110
	Reverse	TTCTTGGTCGGTGGGTGACTCTG	
MMP 9	Forward	CGTCTTCCAGTACCGAGAGA	124
	Reverse	GCAGGATGTCATAGGTCACG	
GAPDH	Forward	TGCACCACCAACTGCTTAGC	87
	Reverse	GGCATGGACTGTGGTCATGAG	

On day 2, the RNA was isolated (NucleoSpin RNA isolation kit, Macherey Nagel) and converted to cDNA (OneScript Plus cDNA Synthesis Kit, ABM) according to manufacturer's protocols. For qRT-PCR analysis BlasTaqTM 2X qPCR MasterMix (ABM, Canada) was used with primers given (6 pmol). The qRT-PCR cycling conditions for all the primers were as follows: 95°C, 10 min initial denaturation, followed by denaturation at 95°C 15 s and annealing-extension 65°C 60 s for 35 cycles.

The reaction was terminated with melt curve analysis (65°C-95°C; 1°C/1 cycle). The fold changes of CTGF, COL1A1 and MMP9 was calculated by normalization to GAPDH as an internal control using the $2^{-\Delta\Delta C_t}$ relative expression equation:

$$\Delta C_t (\text{treated}) = C_t (\text{target gene}) - C_t (\text{ref. gene}) \quad (1)$$

$$\Delta C_t (\text{control}) = C_t (\text{target gene}) - C_t (\text{ref. gene}) \quad (2)$$

$$\Delta\Delta C_t = \Delta C_t (\text{treated}) - \Delta C_t (\text{control}) \quad (3)$$

$$\text{Target normalized to reference gene and relative to control} \quad (4)$$

$$(\text{Fold Change}) = 2^{-\Delta\Delta C_t}$$

2.4. Western blotting

72 h post-transfection, the cells were washed with cold PBS, scraped in RIPA buffer supplemented with PMSF (1 mM) and incubated for 30 min at +4°C with constant shaking. The resultant suspension was centrifuged 10000 rpm for 10 min at +4°C and the protein concentration was measured from the supernatant by BCA method. For western

blot analysis, equal amounts of protein sample were separated in SDS-PAGE (4% stacking-12% separating gel). The samples were run at 75V for 90 min and transferred to nitrocellulose membranes using Trans-Blot Turbo Transfer System (Bio-Rad, USA). The membranes were blocked with 5% skim milk (1h at RT) and incubated at +4°C overnight with CTGF primary antibody (Proteintech, 25474-1AP; 1/1000), washed with TBS-T. The membranes were then incubated with HRP-conjugated anti-rabbit secondary antibody (1/2000 at RT) and finally visualized with ECL reagent (SignalFire™, CST) using gel documentation system (GelDoc EZ System, Bio-Rad). The intensity of the protein bands was analyzed using Image Lab 6.1 Software.

2.5. Effect of AON on the proliferation of AGS cells

AGS cells (10^4 cells/well) were seeded on 24 well plates. The cells were transfected with scrambled and CTGF AON sequences by using HP as described in section 2.2. The cells were incubated for 48 h and effect of AON sequences on the cell proliferation was observed by Alamar Blue Cell Viability Assay. For analysis, the cells were washed twice with PBS, colorless DMEM containing 10% Alamar Blue Solution was added to each well and incubated (1.5 hours at 37°C under 5% CO₂). The OD values (570 nm and 595 nm) of the individual wells were used to calculate percent reduction. Data is represented as percent viability calculated with respect to percent reduction of the positive control.

2.6. Statistical analysis

All qualitative data presented were expressed as mean \pm standard deviations. Statistical analyzes were carried out using GraphPad Prism (GraphPad Software 8.0.2). Statistical differences between the groups were determined using one-way ANOVA with Tukey post-hoc analysis. Statistical significance was expressed as $p < 0.05$ *.

3. Results and Discussion

3.1 Gene expression studies

In this study, a novel GapmeR sequence was studied for its efficiency in inhibiting CTGF mRNA in gastric cancer cells. For this intent, the GapmeR sequence targeted specifically to CTGF mRNA was administered to AGS cells with a transfection reagent (HiPerFect Transfection Reagent, Qiagen). As negative control a scrambled GapmeR sequence was used to eliminate the nonspecific inhibitory effect of the GapmeR presence on gene expression. The fold changes of both scrambled and CTGF targeted GapmeR sequences were calculated with respect to TCPS (tissue culture polystyrene) control group, where none of the GapmeR sequences or HiPerFect Reagent were applied. The changes in the gene expressions of the groups were studied with qRT-PCR technique and analyzed by $2^{-\Delta\Delta C_t}$ relative quantification method (Figure 1). The primer pairs used for the study are provided in Table 1.

48 h post transfection, statistically significant reduction was observed in CTGF mRNA levels. The fold change of CTGF mRNA was 0.36 ± 0.05 leading to 64% inhibition. In addition, the scrambled GapmeR sequence did not lead to any reduction in the fold change of CTGF mRNA. This result shows that the inhibition of CTGF mRNA in CTGF GapmeR administered cells was not a nonspecific reduction. The suppression in CTGF levels is due to the GapmeR sequence used specifically against CTGF [26].

After confirming the reduction in CTGF mRNA levels in gastric cancer cells, the ultimate effect of CTGF inhibition on the expression of ECM components, such as COL1A1 and MMP9 gene expression levels were also studied by qRT-PCR technique. COL1A1

mRNA expression was also found to be significantly reduced (80%) by the treatment with the CTGF GapmeR (AON) sequence. The fold change of Col1A1 mRNA was found to be 0.20 ± 0.06 . This result is very important for this study, because COL1A1 is closely related to tumor regulation, functioning as an oncogene [27,28]. Many studies confirmed that, in different kinds of cancers, COL1A1 is associated with the metastatic ability, invasion and proliferation of cancer cells and the same results were observed with gastric cancer cells. For instance, the downregulation of COL1A1 through miRNA resulted in reduction in cell invasion and migration capability in gastric cancer cells. In addition, in the same study, siRNA mediated knockdown of COL1A1 caused reduced cell viability and proliferation [29]. It is known that the increased COL1A1 levels activate the TGF β signaling and thus ultimately leads to increased migration and invasion. Therefore, the suppression of COL1A1 might be advantageous in reducing the migration of gastric cancer cells. In addition, CTGF, being the downstream mediator of TGF β , is known to induce the migration of gastric cancer cells, which can be reversed by RNAi induced knockdown of CTGF. Taking the information about the involvement of CTGF in cell migration and the effect of COL1A1 expression in cell invasion, migration and proliferation of gastric cancer cells, finding effective therapeutic agents acting on CTGF and COL1A1 can be considered as an advantageous treatment strategy. In this study, the GapmeR mediated suppression of CTGF also resulted in inhibition in COL1A1 expression. This result can be considered as a good starting point to further explore the response of the cells to this reduction. Therefore, further studies such as wound healing assay and Matrigel-coated invasion assays [30] are required to observe the effectiveness of the inhibition of these mRNA levels on migration and invasion.

Since cancer invasion and metastasis requires the action of matrix metalloproteinases (MMP), reduction in the MMP levels can be considered as a powerful impact of the therapeutic reagent. Alteration in MMP-9 levels was chosen as a parameter to be analyzed in the present study because of its importance in invasion in addition to the direct effect of CTGF on MMP-9 levels and activity [31]. The transfection of AGS cells with CTGF targeting AON sequence, however, did not cause any inhibition in *MMP 9* levels. This was an interesting result, as mentioned before, the direct effect of inhibition of CTGF in gastric cancer cells resulted in the reduction in MMP-9 levels as determined by qRT-PCR and western blot analysis. The unsuccessful inhibition of *MMP 9* in AGS cells might be due to AON dose used for the study. The proliferation of cells during experiments ultimately may lead to reduction in the AON concentration per cell, therefore by increasing the dosing, effective *MMP9* inhibition might be observed. Moreover, time course studies might be performed to determine whether the unsuccessful mRNA suppression is because of insufficient dose, or due to RNA turnover.

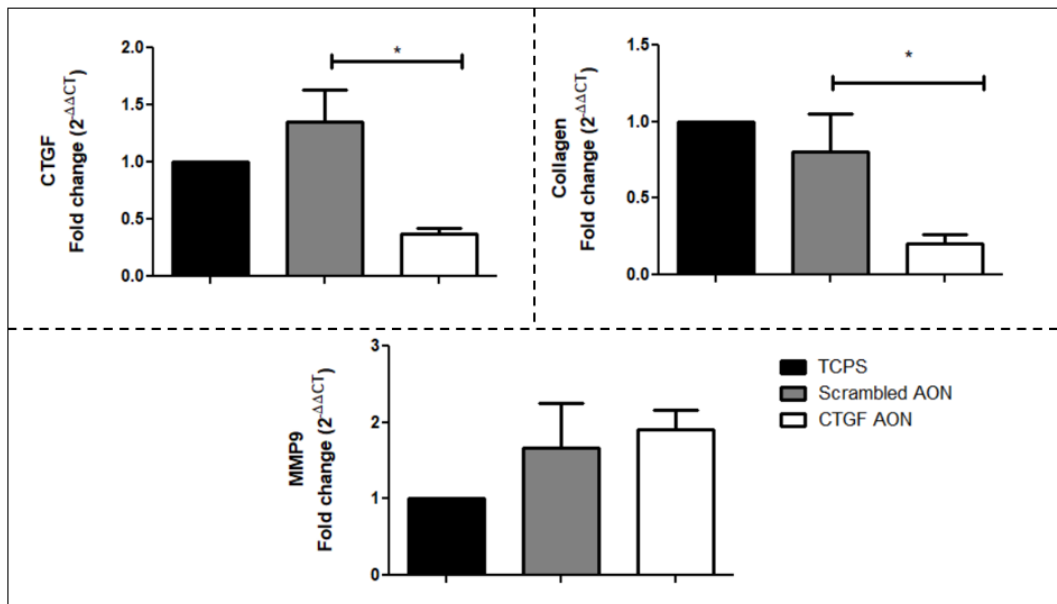


Figure 1. Fold changes of *CTGF*, *collagen (Col1A1)* and *MMP9* mRNA expression after administration of GapmeR sequence. TCPS: TCPS control; Scrambled AON: Treatment with scrambled AON sequence, CTGF AON: Treatment with CTGF AON sequence. The fold changes are given as mean \pm STDEV ($p < 0.05$ *)

3.2 Western blotting

The effect of CTGF GapmeR AON on the CTGF protein levels were also studied by western blot technique (Figure 2). The CTGF band intensity was normalized to the corresponding band intensity of β -actin. With respect to TCPS control group, a 44% inhibition in CTGF protein levels was observed, when the AGS cells were treated with the GapmeR AON sequence. The achievement of reduction in CTGF protein levels implies that the amount of AON administered to AGS cells was sufficient to suppress both the CTGF mRNA and protein levels.

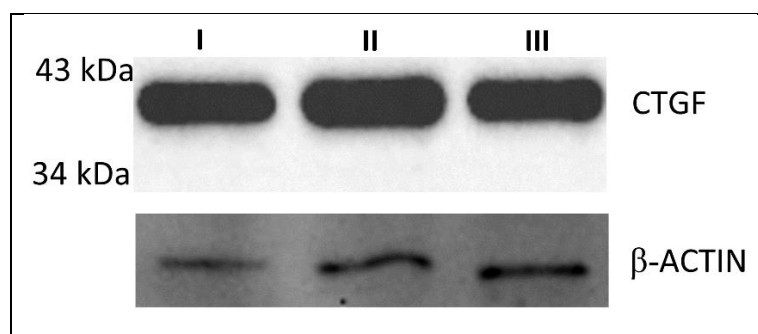


Figure 2. CTGF protein expression of AGS cells after treatment with CTGF GapmeR AON sequence. β -actin serves as loading control. I: TCPS Control, II: Treatment with scrambled AON sequence, III: Treatment with CTGF AON sequence.

3.3 Effect of AON on the proliferation of AGS cells

It is known that abnormal expression of CTGF in different types of tumors such as prostate cancer, gliomas, breast cancer is also observed in gastric cancer, and it leads to increased cell proliferation along with increased migration and metastasis. Therefore, it is important to observe reduced proliferation of gastric cancer cells following CTGF GapmeR AON treatment. The proliferation ability of the AGS cells were studied with Alamar Blue Cell Viability Assay. It can be clearly observed from Figure 3 that, with the treatment of cells with CTGF GapmeR AON, the proliferation of the cells reduced significantly (by 50%) when compared to TCPS. More importantly, the scrambled AON

did not cause reduction in cell viability, revealing that the reduction in AGS cell proliferation with CTGF AON administered group is not through the toxicity of the GapmeR presence, but through the inhibition in abnormal CTGF expression in gastric cancer cells. There are studies in the literature suggesting the possible reason for reduced gastric cell proliferation due to CTGF inhibition. Cyclin D1 levels, one of the regulators of cell cycle, in addition to the c-Myc levels were found to be correlated with the overexpression of CTGF and thus the proliferation [32]. Therefore, suppressing CTGF levels might reduce the proliferation, however further studies are needed to understand the background of reduced cell proliferation with suppression of CTGF in AGS cells.

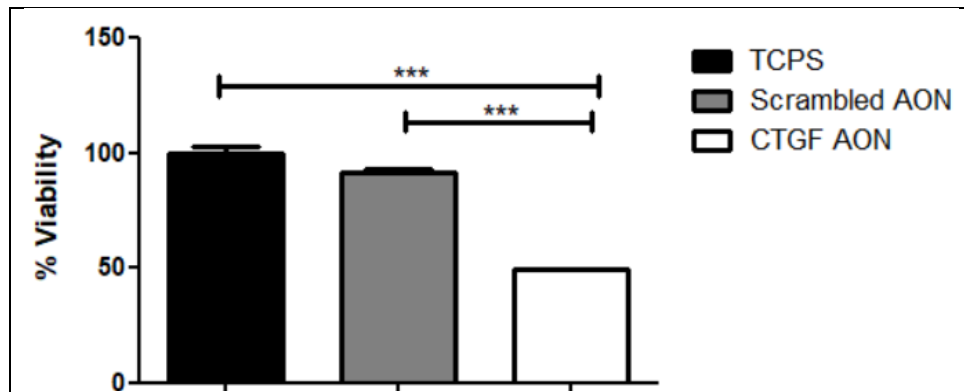


Figure 3. % viability of AGS cells treated with GapmeR sequences. ($p < 0.001$ ***)

4. Conclusion

In summary, the custom designed CTGF GapmeR AON, used in this study is highly effective in inhibiting the CTGF mRNA expression in gastric cancer cells. The reduction is also followed by the reduced expression of collagen from the AGS cells, which might be the indicator of reduced ECM production. The CTGF reduction was also observed in the protein levels and caused significant suppression in the proliferation of AGS cells. Further studies with mentioned GapmeR sequence on gastric cancer cell proliferation, migration and invasion, may lead to the development of alternative effective ways for reversing the tumor enlargement, invasion and metastasis.

Authorship contribution statement

D. Sezlev Bilecen: Conceptualization, Methodology, Experimental Procedures, Data Collection, Writing.

Declaration of competing interest

The authors declare that they have no known competing financial interests or personal relationships that could have appeared to influence the work reported in this paper.

Acknowledgment

The authors acknowledge Konya Food and Agriculture University for laboratory facilities.

Ethics Committee Approval and/or Informed Consent Information

As the authors of this study, we declare that we do not have any ethics committee approval and/or informed consent statement.

References

- [1] E. C. Smyth, M. Nilsson, H. I. Grabsch, N. Ct Van Grieken, and F. Lordick, “Gastric cancer Epidemiology and risk factors”, *The Lancet*, 396, 635–48, 2020.
- [2] H. Sung, J. Ferlay, R. L. Siegel, M. Laversanne, I. Soerjomataram, A. Jemal, and F. Bray, “Global Cancer Statistics 2020: GLOBOCAN Estimates of Incidence and Mortality Worldwide for 36 Cancers in 185 Countries”, *CA: A Cancer Journal for Clinicians*, 71(3), 209–249, 2021.
- [3] S. S. Joshi and B. D. Badgwell, “Current treatment and recent progress in gastric cancer”, *CA: A Cancer Journal for Clinicians*, 71(3), 264–279, 2021.
- [4] S. W. T. Ho and P. Tan, “Dissection of gastric cancer heterogeneity for precision oncology”, *Cancer Science*, 110, 3405–3414, 2019.
- [5] X. F. Zhang, C. M. Huang, H. S. Lu, X. Y. Wu, C. Wang, G. X. Guang, J. Z. Zhang, and C. H. Zheng, “Surgical treatment and prognosis of gastric cancer in 2 613 patients”, *World Journal of Gastroenterology*, 10(23), 3405-3408, 2004.
- [6] P. Bork, “The modular architecture of a new family of growth regulators related to connective tissue growth factor”, *Federation of European Biochemical Societies*, 327(2), 125-130, 1993.
- [7] L. F. Lau and S. C-T Lam, “The CCN Family of Angiogenic Regulators: The Integrin Connection”, *Experimental Cell Research*, 248, 44–57, 1999.
- [8] L. Kular, J. Pakradouni, P. Kitabgi, M. Laurent, and C. Martinerie, “The CCN family: A new class of inflammation modulators?”, *Biochimie*, 93(3), 377–388, 2011.
- [9] Z. Mao, X. Ma, Y. Rong, L. Cui, X. Wang, W. Wu, J. Zhang, and D. Jin, “Connective tissue growth factor enhances the migration of gastric cancer through downregulation of E-cadherin via the NF- κ B pathway”, *Cancer Science*, 102(1), 104–110, 2011.
- [10] J. Hutchenreuther, K. Vincent, C. Norley, M. Racanelli., S. B. Gruber, T. M. Johnson, D. R. Fullen, L. Raskin, B. Perbal, D. W. Holdsworth, L. M. Postovit, and A. Leask, “Activation of cancer-associated fibroblasts is required for tumor neovascularization in a murine model of melanoma”, *Matrix Biology*, 74, 52–61, 2018.
- [11] L. Y. Liu, Y. C. Han, S. H. Wu, and Z. H. Lv, “Expression of connective tissue growth factor in tumor tissues is an independent predictor of poor prognosis in patients with gastric cancer”, *World Journal of Gastroenterology*, 14(13), 2110–2114, 2008.
- [12] A. M. Moreira, J. Pereira, S. Melo, M. S. Fernandes, P. Carneiro, R. Seruca, and J. Figueiredo, “The Extracellular Matrix: An Accomplice in Gastric Cancer Development and Progression”, *Cells*, 9(2), 394-417, 2020.
- [13] S. Z. Chen, H. Q. Yao, S. Z. Zhu, Q. Y. Li, G. H. Guo, and J. Yu, “Expression levels of matrix metalloproteinase-9 in human gastric carcinoma”, *Oncology Letters*, 9: 915-919, 2015.
- [14] Q. N. Zhang, H.L. Zhu, M.T. Xia, J. Liao, X.T. Huang, J.W. Xiao, and C. Yuan, “A panel of collagen genes are associated with prognosis of patients with gastric cancer and regulated by microRNA-29c-3p: An integrated bioinformatics analysis and experimental validation”, *Cancer Management and Research*.11, 4757–4772, 2019.
- [15] J. Li, Y. Ding, and A. Li, “Identification of COL1A1 and COL1A2 as candidate prognostic factors in gastric cancer”, *World Journal of Surgical Oncology*, 14, 297, 2016.
- [16] Y. Zhao, T. Zhou, A. Li, H. Yao, F. He, L. Wang, and J. Si, “A potential role of collagens expression in distinguishing between premalignant and malignant lesions in stomach”, *Anatomical Record*, 292(5), 692–700, 2009.
- [17] Y. Guo, G. Lu, H. Mao, S. Zhou, X. Tong, J. Wu, Q. Sun, H. Xu, and F. Fang, “miR-133b Suppresses Invasion and Migration of Gastric Cancer Cells via the COL1A1/TGF- β Axis”, *Oncotargets and Therapy*, 13: 7985-7995, 2020.
- [18] Q. Wang and J. Yu, “MiR-129-5p suppresses gastric cancer cell invasion and proliferation by inhibiting COL1A1” *Biochemistry and Cell Biology*, 96: 19-25, 2018.
- [19] A. Baghbazadeh, E. Baghbani, K. Hajiasgharzadeh, S. Noorolyai, V. Khaze, B. Mansoori, M. Shirmohamadi, B. Baradaran, and A. Mokhtarzadeh, “microRNA-193a-5p Suppresses the Migratory Ability of Human KATO III Gastric Cancer Cells through Inhibition of Vimentin and MMP-9”, *Advanced Pharmaceutical Bulletin*, 12(1): 169-175, 2022.
- [20] C. G. Jiang, L. Lv, F. R. Liu, Z. N. Wang, F. N. Liu, Y. S. Li, C. Y. Wang, H. Y. Zhang, Z. Sun, and H. M. Xu, “Downregulation of connective tissue growth factor inhibits the growth and invasion of gastric cancer cells and attenuates peritoneal dissemination”, *Molecular Cancer*. 28 (10), 122, 2011.
- [21] I. Radziejewska, K. Supruniuk, J. Nazaruk, E. Karna, B. Popławska, A. Bielawska, and A. Galicka, “Rosmarinic acid influences collagen, MMPs, TIMPs, glycosylation and MUC1 in CRL-1739 gastric cancer cell line”, *Biomedicine & Pharmacotherapy* 107: 397–407, 2018.
- [22] Y. Song, J. S. Kim, E. K. Choi, J. Kim, K. M. Kim, and H. R. Seo, “TGF- β -independent CTGF induction regulates cell adhesion mediated drug resistance by increasing collagen I in HCC”, *Oncotarget*, 8(13): 21650-21662, 2017.

- [23] H. Sun, Y. Wang, S. Wang, Y. Xie, K. Sun, S. Li, W. Cui, and K. Wang, "The involvement of collagen family genes in tumor enlargement of gastric cancer", *Scientific Reports*, 13(1), 100-111, 2023.
- [24] S. Karaki, C. Paris, and P. Rocchi, "Antisense Oligonucleotides, A Novel Developing Targeting Therapy", in *Antisense Therapy*, Editors, S. Sharad, S. Kapur, doi: 10.5772/intechopen.73736, 2019.
- [25] C. F. Bennett and E. E. Swayze, "RNA targeting therapeutics: Molecular mechanisms of antisense oligonucleotides as a therapeutic platform", *Annual Review of Pharmacology and Toxicology*, 50, 259-293, 2010.
- [26] T. Tabaglio, D. H. P. Low, W. K. L. Teo, P. A. Goy, P. Cywoniuk, H. Wollmann, J. Ho, D. Tan, J. Aw, A. Pavesi, K. Sobczak, D. K. B. Wee, and E. Guccione, "MBNL1 alternative splicing isoforms play opposing roles in cancer", *Life Science Alliance*, 1(5): e201800157, 2018.
- [27] P. Sengupta, Y. Xu, L. Wang, R. Widom, and B. D. Smith, "Collagen alpha1(I) gene (COL1A1) is repressed by RFX family", *Journal of Biological Chemistry*, 280(22): 21004-21014, 2005.
- [28] M. Hayashi, S. Nomoto, M. Hishida, Y. Inokawa, M. Kanda, and Y. Okamura, "Identification of the collagen type 1 alpha 1 gene (COL1A1) as a candidate survival-related factor associated with hepatocellular carcinoma", *BMC Cancer*, 14: 108, 2014.
- [29] Y. Shi, Z. Duan, X. Zhang, X. Zhang, G. Wang, and F. Li, "Down-regulation of the let-7i facilitates gastric cancer invasion and metastasis by targeting COL1A1" *Protein & Cell*. Feb;10(2):143-148. 2019.
- [30] K. I. Hulkower and R. L. Herber, "Cell Migration and Invasion Assays as Tools for Drug Discovery" *Pharmaceutics*, 3, 107-124, 2011.
- [31] H. S. Kim, M. H. Kim, M. Jeong, Y. S. Hwang, S. H. Lim, B. A. Shin, B. W. Ahn, and Y. D. Jung, "EGCG blocks tumor promoter-induced MMP-9 expression via suppression of MAPK and AP-1 activation in human gastric AGS cells", *Anticancer Research*, 24(2B):747-53, 2004.
- [32] Y. Z. Deng, P.P. Chen, Y. Wang, D. Yin, H. P. Koeffler, B. Li, X. J. Tong, and D. Xie, "Connective tissue growth factor is overexpressed in esophageal squamous cell carcinoma and promotes tumorigenicity through beta-catenin-T-cell factor/Lef signaling", *Journal of Biological Chemistry*, 14;282(50):36571-81, 2007.

Electric Field Responsive Smart Fluids from Olive Pulp Powder

Özlem Erol*

Chemistry Department, Science Faculty, Gazi University, 06560, Ankara, TÜRKİYE

<https://orcid.org/0000-0003-2156-537X>

*corresponding author: erol@gazi.edu.tr

(Received: 12.03.2024, Accepted: 12.08.2024, Published: 25.11.2024)

Abstract: This study aims to evaluate one of the wastes of the olive oil industry, olive pulp powder (OP), due to its consisting of mainly polarizable lignocellulosic biomass, as a dispersed phase in electric field-responsive (ER) fluid whose rheological properties can be tuned by an externally applied electric field (E). The supplied OP was extracted with n -hexane, and structural and thermal analysis revealed the removal of residual oil and soluble small molecules. The OP and n -hexane treated-OP (h-OP) were dispersed in silicon oil (SO), and their rheological and dielectric properties, and dispersion stabilities were investigated. According to the flow test results, the yield stresses (τ_y) of both dispersions increased with increasing concentration and the E . The τ_y of the OP/SO and h-OP/SO dispersions (25 wt%) under $E=3.5$ kV/mm increased 29 and 130 times greater than their τ_y values under no E , respectively. The dielectric spectrum analysis showed that enhanced interfacial polarization and decreased nonpolarized forces after the n -hexane extraction improved the ER response of the h-OP/SO dispersion. The enhanced dispersion stability (90%) was determined for h-OP/SO dispersion at 25 wt%. As a result, the h-OP could be a sustainable candidate for evaluation as a dispersing phase of ER fluids for vibration-damping systems.

Key words: Sustainability, Agricultural industry waste, Olive pulp powder, Electric field responsive fluids, Upcycling

1. Introduction

With the advancement of technology, the rise in productivity of agricultural products leads to significant increases in waste production. Due to the high amount of waste generated in the agricultural industry, its high cost and environmental effects lead to a substantial problem. Both academic and industrial studies on transforming bio-based products obtained from raw biomass and renewable agricultural resources into eco-friendly products capable of rivaling petroleum-based alternatives in the market have recently attracted attention [1]. The significant rise in the world population leads to a rapid increase in food consumption and, therefore, to a rise in agricultural industry-related wastes released. For this reason, it is essential to encourage producers and consumers to reduce solid waste production by recycling, reusing, and upcycling. Recently, increasing awareness of environmentally friendly products and choosing biodegradable materials have come to the fore to overcome and reduce environmental problems.

Smart materials with rheological characteristics that can be manipulated using an external electric field (E) are promising for applications such as hydraulic control systems, robotic systems, the automotive industry, microfluidics, and drug release [2] and one of them is called electric-field responsive or electrorheological (ER) fluids. The suitable particles that can be polarized by the E effect are dispersed in an insulating carrier fluid like silicone

oil (SO) to obtain an ER fluid. In the ER fluid, fibrillar or columnar-like structures perpendicular to the electrodes are formed by aligning the dispersed particles in the applied E direction. These reversibly formed structures allow the dispersion to transform from a liquid-like state to a solid-like state. Many ER-active materials have been developed and reported in the literature to date. The first studies were mostly on materials such as silica, alumina, zeolite, cellulose, and starch, which derive their polarizability from the water adsorbed into their structure. Subsequently, interest has turned to intrinsically polarizable materials, such as various conductive polymers, carbon nanotubes, graphene oxide, and poly(ionic) liquids, whose polarizability does not depend on the water in their structure [3].

Considering sustainability and green chemistry principles, priority should be given to studies on developing ecological products in ER fluids or using green strategies to prepare ER active materials. In this respect, because of their biodegradability and natural abundance, the use of biologically sourced materials such as cellulose [4], chitin, chitosan [5, 6, 7], porous chitosan [7], starch [8, 9, 10], alginate [11], etc., and their modified forms or composites have been reported as ER active materials. In addition to environmentally friendly materials, there have been limited studies in the literature on using agricultural wastes as ER active materials. In a study, the ER performance of microcrystalline cellulose obtained from rice husk waste by applying alkaline, bleaching, and hydrolysis processes were examined, and its electric field response was reported to be lower compared to previously prepared microcrystalline cellulose using different sources but exhibited viscoelastic properties with similar trends [12]. In another study, microcrystalline cellulose obtained from rice husk waste was used to prepare phosphatized microcrystalline cellulose via the esterification reaction of cellulose in the presence of urea and phosphoric acid, and its dispersions in SO displayed a higher ER response [13]. Also, waste rice husk was utilized to prepare nano-silica particles by applying acid and heat treatments, and it was reported that its dispersion in SO responded strongly to the E [14]. In another study, the dispersion of organic waste spent coffee grounds obtained after extracting coffee from roasting coffee grounds (containing trace metals and hemicellulose, cellulose, lignin, and some residual acids released during roasting of coffee) in SO was reported to show higher ER activity at a particular threshold concentration value (40% by volume) than pre-waste state ground coffee dispersion in SO [15]. It was suggested that the ER activity of spent coffee grounds was due to some functional groups remaining on the grain surfaces after the extraction process.

In the olive oil production process, olive pulp (OP) is obtained by processing the residual solid waste, mostly consisting of seeds, shell, and pulp, remaining after the extraction of crude olive oil [16]. High amounts of organic matter, fat, carbohydrates, proteins, and water-soluble phenolic species remained in the OP, and its composition mainly consists of lignocellulosic biomass (30-41.6% lignin, 35.3-49.0% cellulose, pectic polymers, hemicelluloses, oils, and minerals) [16]. The utilization of agro-industrial residue, OP, is increasingly gaining attention and becoming more commonplace as a fuel, an additive in animal feed, and a filler in polymer composites [17]. Since this agricultural industry waste comprises polarizable structures such as cellulose, hemicellulose, and lignin, OP can be evaluated as a dispersed phase in electric field-responsive smart fluids.

This study aimed to evaluate one of the agro-industrial wastes, the OP, as an electric field-responsive material. The supplied OP particles were washed with n -hexane using a Soxhlet apparatus to remove residual oil and soluble small fatty acid molecules. After ball-milling, OP and n -hexane treated OP (h-OP) were used as the dispersed phase for preparing ER fluid. OP and h-OP dispersions were prepared in SO. Their dielectric

properties and dispersion stabilities were investigated, and their rheological properties under E were explored via steady shear, oscillatory shear, and creep-recovery tests.

2. Materials and Methods

2.1. Materials

Olive pulp (OP) particles, approximately 150 μm size were kindly supplied under the brand name MOROVA by the Şenol Food Industry Incorporated Company (Aydın, Türkiye). The supplied OP particles comprised the pulp-rich part obtained by processing the solid waste pulp remaining after the oil was taken from the olive fruit after drying and granulating. The extraction solvent, *n*-hexane, was purchased from Merck and used as received. Silicone oil (SO, polydimethylsiloxane with viscosity of 1.0 Pa s and density of 0.967 g/mL) was provided from Sigma Aldrich and vacuum dried before preparing ER fluids as a dispersing medium.

2.2. Preparation of ER fluids

Before using the OP particles for the preparation of ER fluids as a dispersing phase and for further characterization studies, the residual oil, soluble small molecules, and fatty acids were extracted via the Soxhlet extraction at 100°C using *n*-hexane for 24 h. After vacuum drying at 60°C for 24 h, to obtain fine-grade powder form for further uses, the OP particles and *n*-hexane extracted OP particles (h-OP) were grounded using a ball-miller at 20 Hz for 20 min (Retsch, MM400, Germany). The ER dispersions were prepared by dispersing OP and h-OP at mass percent concentration series of 5-25 wt% in SO with 5% increments. The dispersions were mixed mechanically and then thoroughly using a probe sonicator (Sonics, Vibracell, USA) to make uniform dispersion, and utilized for the rheological, dielectric, and dispersion stability measurements.

2.3. Characterization methods

The primary functional groups present in OP and h-OP were determined via attenuated total reflectance Fourier transform infrared spectroscopy (ATR-FTIR, Thermo Scientific, Nicolet IS50, USA), operating with a resolution of 4 cm^{-1} and conducting 64 scans. Elemental analysis of the samples was conducted using Thermo Scientific Flash 2000 organic elemental analyzer (USA). The thermal analysis of the samples was conducted using a Hitachi STA 7300 (Japan) thermogravimetric analyzer device in the range of an ambient temperature to 800°C under an inert Ar atmosphere, and the heating rate was adjusted to 10°C/min. The degradation temperature at which the most significant mass loss occurred (T_{max}) was measured from the maximum value of the mass loss derivative. After coating with a thin layer of gold using a sputter coater (Leica EM ACE200, Germany), the morphologies of the samples were investigated via scanning electron microscopy (SEM) with an accelerating voltage of 5 kV (SEM, Hitachi SU5000, Japan). The four-probe technique was employed to measure the electrical conductivities of the OP and h-OP by using their compressed disc-shaped pellets with defined dimensions at 25°C (Entek Electronic, FPP 470-A, Türkiye), and the average electrical conductivity values of the samples were derived by collecting measurements from at least five distinct locations on the pellet. The apparent densities of OP and h-OP were determined using the calculated volume and measured mass of the prepared pellets as mentioned earlier.

2.4. Dielectric measurements

An impedance analyzer (Agilent E4980A precision LCR meter, Japan) equipped with a parallel plate capacitor for liquids (Agilent 16452A, Japan) was used to measure the

dielectric characteristics of the OP and h-OP dispersions within the frequency range from 20 Hz to 1 MHz.

2.5. Dispersion stability measurements

The dispersion stabilities of the OP and h-OP dispersions were determined by taking the percentage ratios of the height of the dispersion occupied by the particle-rich part to the entire height of the dispersion.

2.6. The rheological measurements

The rheological measurements of all the OP and h-OP dispersions were conducted at 25°C using a torque rheometer (Thermo-Haake RS600, Germany) connected to the DC electric field generator (HCL 14, FuG Elektronik, Germany). During measurements, the gap between the measuring geometries of 35.0 mm parallel plates was adjusted to 1.0 mm. After pre-shearing (60 s^{-1}) for 60 s, the dispersions were allowed to reach equilibrium without shearing for 60 s under a particular E application before initiating each measurement. The flow curves were generated by measuring shear stresses (τ) and viscosities (η) as a function of shear rates ($\dot{\gamma}$) under various E values. The elastic and loss moduli were determined via dynamic oscillatory rheological measurements to display the viscoelastic properties of the ER fluids. Firstly, elastic, and viscous modulus values of the dispersions were measured as a function of shear stress at a constant frequency of 1 Hz as a function of the E to determine the linear viscoelastic regions (LVER). The LVER was determined by observing the limit of the plateau region of elastic modulus (G') versus the stress curve after where the G' became stress-dependent. Secondly, the viscoelastic moduli were measured over a 1-100 Hz frequency range at constant stress levels within the predefined LVER at various E values. The creep-recovery tests were conducted through measurement of the strain values over a specified period of 100 s during the application of the applied stress ($\tau > 0$) instantaneously and recovered strain values after releasing the applied stress ($\tau = 0$) for another 100 s.

3. Results

3.1. Characterizations

The OP and h-OP samples displayed the specific FTIR spectrum of a lignocellulosic compound dominantly (Figure 1). Both materials exhibited similar peaks without any significant peak shifts but with a decrease in peak intensity for several peaks, as discussed below. The OP presented a broad band with a maximum of around 3300 cm^{-1} , assigned to the stretching vibration of the O–H involved in hydrogen bonding. The two peaks around 2922 and 2852 cm^{-1} , identified as the asymmetric and symmetric C–H stretching vibrations in methyl and methylene groups found in cellulose, lignin, hemicellulose, and fatty acids, were notably observed in OP [18, 19].

The peaks observed at various wavenumbers corresponded to specific molecular vibrations are given as following: The band observed at 1740 cm^{-1} was assigned to the stretching vibration of C=O bonds in carbonyl, carboxyl, and acetyl groups; 1635 cm^{-1} represented a composite signal encompassing bands associated with conjugated C–O bonds in quinones coupled with C=O stretching in various groups, as well as contributions from adsorbed water molecules and C=C stretching in the aromatic skeleton of lignin; C=O stretching vibrations in the amide bond of residual proteins; 1514 cm^{-1} indicated the stretching vibration of C=C bonds in the aromatic skeleton of lignin and N-H bending and C-N stretching vibrations in the residual proteins; the signals at 1455 and 1416 cm^{-1} were linked to the deformation of C–H bonds in lignin and carbohydrates; 1373 cm^{-1}

corresponded to the bending vibration of C–H bonds in cellulose and hemicellulose, along with the stretching vibration of C–O bonds in the guaiacyl unit of lignin; 1232 cm^{-1} represented the stretching vibration of C–H bonds in the syringyl unit of lignin and C–N stretching vibrations found in residual proteins; 1030 cm^{-1} was designated as representing the skeletal vibration of the C–O–C pyranose ring in cellulose [19, 20] and $\sim 600\text{--}750\text{ cm}^{-1}$ may be corresponded to the stretching of the C–S bonds in the residual sulfur containing amino acids [22]. All peaks were retained for h-OP after Soxhlet extraction of OP with *n*-hexane. However, the reductions of the broad peak spanning from 3600 and 3000 cm^{-1} , the peaks around 2922 and 2852 cm^{-1} , and the peak at 1740 cm^{-1} can be ascribed to the successful removal of the excess oil, fatty acids, and non-polar soluble molecules in the OP after Soxhlet extraction for h-OP.

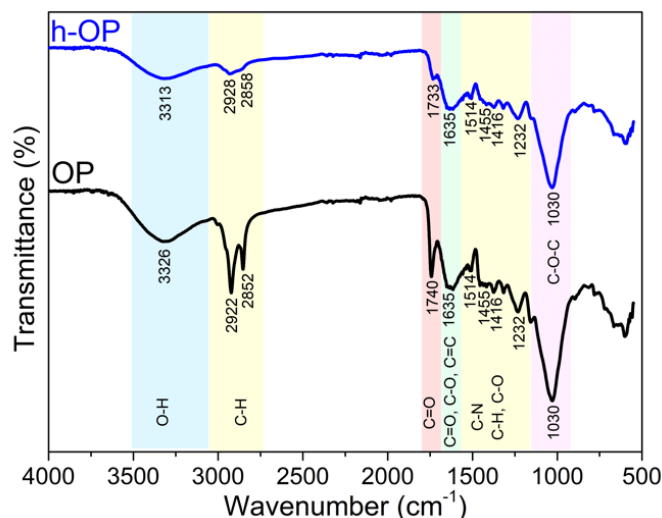


Figure 1. ATR-FTIR spectra of the OP and h-OP

The elemental composition of the OP depends on the origin of the compound [21]. As a lignocellulosic material, the main substances in OP are carbon sources constituting hemicellulose, cellulose, and lignin. Additionally, protein and extractives as nitrogen, sulfur sources, and fat are other constituents of the OP [22]. The removal of the excess olive oil, fatty acids, and soluble extractive molecules was also revealed by elemental analysis. According to the elemental analysis results, the decrease in C and H content of the OP after Soxhlet extraction revealed the successful removal of excess olive oil, fatty acids, and small soluble non-polar molecules. On the other hand, *n*-hexane extraction could not effectively remove the most polar compounds, including proteins and amino acids (which were sources of N and S). The elemental analysis results were in good agreement with the ATR-FTIR results.

Table 1. The % composition obtained from elemental analysis (N, C, H, S) of the OP and h-OP

Sample	N (%)	C (%)	H (%)	S (%)
OP	1.8343±0.0335	51.0651±0.071	6.4708±0.0247	0.1409±0.0077
h-OP	3.9993±0.2572	48.2369±0.037	5.8969±0.2877	0.1572±0.0079

A comparison of the thermogravimetry (TG)/differential TG (DTG) curves of the OP and h-OP is presented in Figure 2a-b. The OP and h-OP exhibited two main decomposition steps in an inert atmosphere during the thermal degradation (Figure 2a). A slight mass loss of 6% and 5% occurred between 40°C and 130°C , corresponding to the evaporation of moisture adsorbed to the OP and the h-OP, respectively. The second decomposition step occurred within the $150\text{--}550^{\circ}\text{C}$ temperature range for both samples. According to the previous studies, the primary constituents of the OP, i.e. hemicellulose, cellulose, and

lignin, showed consecutive pyrolysis steps involving primary pyrolysis of hemicellulose occurred between 150-315°C giving a shoulder at lower temperatures, and cellulose occurred between 300-400°C with a well-defined sharp peak followed by mainly lignin pyrolysis occurred over a broad temperature span from 100°C to 900°C as a wide shoulder on the main degradation domain [23, 24]. Besides, the decomposition temperature intervals of these components can partially overlap [19]. The OP studied in this work showed a T_{\max} at 320°C followed by decay with a long tail and a shoulder around 366°C which disappeared for h-OP (Figure 2b) due to the removal of remaining olive oil [25] in the OP after the Soxhlet extraction process, corresponding to approximately 4% mass loss difference, which was consistent with the elemental analysis results by considering the difference in C and H content between OP and h-OP. Hemicellulose, composed of various saccharides, has random and amorphous structures and, thus, has weaker thermal stability than cellulose, with an ordered and long unbranched linear polymeric structure consisting of glucose units with a glycosidic bond. For that reason, the shoulder is usually observed for hemicellulose content of the OP at lower temperatures of the main decomposition peak. However, this shoulder did not appear in the DTG curve of the OP and h-OP due to the superposition of its decomposition with cellulose and lignin [19]. Additional broad peaks with insignificant intensity observed above 600°C were detected, likely indicating the decomposition of mineral matter in the samples [26].

The SEM images in Figure 2c-d indicated that both samples demonstrated approximately the same size, irregular, particulate-like, and slightly porous structures with cavities on the surfaces. In previous studies, spherical-like with a low aspect ratio and porous structures were reported for olive pulp powder [24, 27].

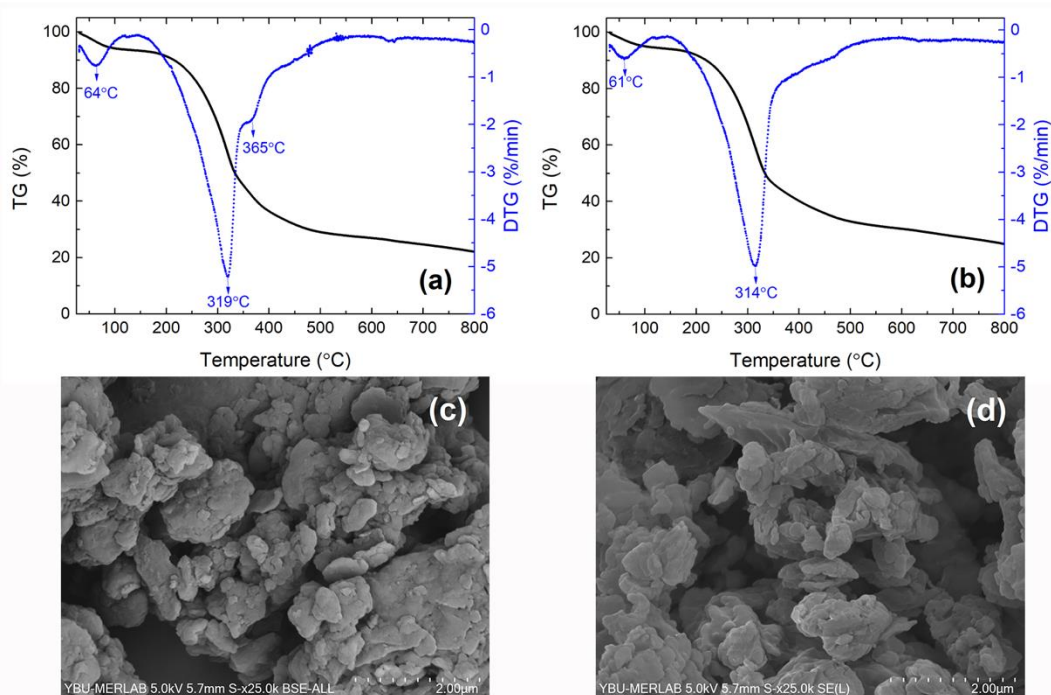


Figure 2. TG/DTG curves of (a) OP and (b) h-OP, and SEM image of (c) OP and (d) h-OP

Various critical key factors affect the electric field response of the ER fluid including particle size distribution, shape, wettability, electrical conductivity, dielectric characteristics of the particles, the concentration of the dispersion, the E , temperature, properties of carrier fluid, and dispersion stability [2]. Therefore, developing ER fluids with the desired high performance is challenging given the complexity of these variables. The conductivity of the dispersed particles is recommended to be in the semiconducting range of 10^{-6} – 10^{-12} S/cm [28]. The conductivities of OP and h-OP were measured as

$(8.05 \pm 0.83) \times 10^{-7}$ S/cm and $(5.44 \pm 1.00) \times 10^{-7}$ S/cm, respectively, indicating their being in the desired range as an ER active material. Additionally, Soxhlet extracting with n-hexane may lead to a relative decrease in the conductivity of OP due to the removal of the fatty acid molecules.

3.2. Dielectric properties

The strength of the electric field response of an ER fluid has a strong relationship with its dielectric properties, and thus, so does the polarizability of the dispersed particles. A good ER response requires larger interfacial polarizability and dielectric loss peaks in the 10^2 to 10^6 Hz range. The dielectric analysis was conducted to explore the correlation between the intensity of the ER phenomenon and the dielectric characteristics of ER fluids. The spectra of dielectric permittivity (ϵ') and loss (ϵ'') of the OP/SO and h-OP/SO dispersions are shown in Figure 3 for 25 wt%.

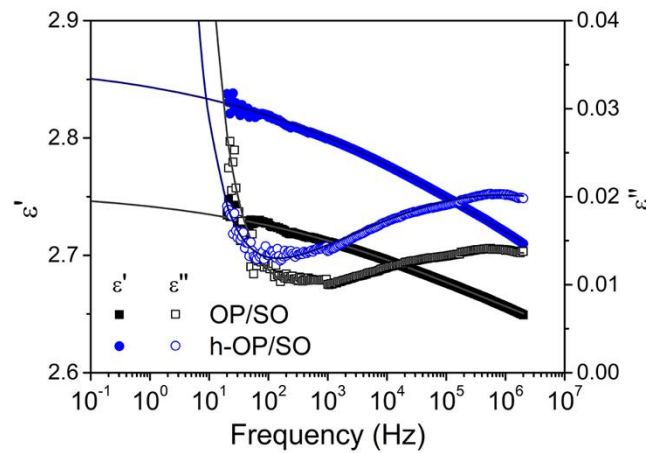


Figure 3. Dielectric spectra of the OP/SO and h-OP/SO dispersions (25 wt%). The solid lines show the fitted the ϵ' and ϵ'' spectra using the Equation 1

The Havriliak–Negami (HN) dielectric relaxation equation (Equation 1), combined with the conductivity term, was applied to fit the experimental complex dielectric permittivity, $\epsilon^*(\omega)$ [29, 30]. The first two terms indicate the HN function for a single relaxation process, and the last term corresponds to the contribution of conductivity to the dielectric loss spectrum in Equation 1 [31]. Additionally, the ω is the angular frequency (f), where $\omega = 2\pi f$. The τ_{HN} is the average relaxation time of the polarization process and is equal to $1/2\pi f_{max}$ where f_{max} represents the frequency at which the dielectric loss peak occurs. The $\Delta\epsilon$ is the dielectric relaxation strength, which displays the difference in the ϵ' at low frequency (ϵ_s) with the ϵ' at the high-frequency limit, $\epsilon(\infty)$. The exponents α and β related to the broadness and asymmetry of the respective relaxation loss peak, respectively ($0 \leq \alpha, \beta \leq 1$), and describe the distribution of the relaxation times. The σ is the conductivity of the dispersion, ϵ_0 is the vacuum permittivity (8.854×10^{-12} F/m), and the N denotes the exponent that defines the conduction process. The relevant dielectric parameters obtained are tabulated in Table 2.

$$\epsilon^*(\omega) = \epsilon'(\omega) - i\epsilon''(\omega) = \epsilon(\infty) + \frac{\Delta\epsilon}{[1 + (i\omega\tau_{HN})^{1-\alpha}]^\beta} - i\left(\frac{\sigma}{\epsilon_0\omega}\right)^N \quad (1)$$

Table 2. Dielectric parameters obtained from the fitted dielectric spectra according to the Equation 1 for the OP/SO and h-OP/SO dispersions (25 wt%)

Sample	ϵ_s	$\epsilon(\infty)$	$\Delta\epsilon = \epsilon_s - \epsilon(\infty)$	f_{max} (Hz)	τ_{HN} (s)	α	β	σ
OP/SO	2.755	2.556	0.199	1.0×10^5	1.6×10^{-6}	0.196	0.72	1.8×10^{-11}
h-OP/SO	2.866	2.578	0.288	8.0×10^5	2.0×10^{-7}	0.178	0.99	1.1×10^{-11}

The $\Delta\epsilon$ relates to the degree of interfacial polarization, whereas the relaxation time τ_{HN} denotes the rate of polarization. Maximizing the strength of the relaxation process is crucial for achieving a high ER response [31]. Although the $\Delta\epsilon$ values were relatively low, both dispersions exhibited the required polarization response to the E at the desired rate of 10^2 – 10^6 Hz range. The h-OP/SO exhibited a relatively higher magnitude of interfacial polarization and shorter relaxation time than OP/SO, consistent with the ER performance discussed in section 3.4. At lower frequencies, the dispersions exhibited pronounced electrode polarization traits attributed to the abundant polar hydroxyl groups in cellulose [32]. Comparable rises in dielectric loss were reported in low-frequency regions for nanocellulose and microcellulose particles dispersed in olive oil, attributed to the connection of the cellulose particles in the large agglomerates leading to the conductivity through the dielectric oil medium [31]. The observed difference in dielectric properties of OP/SO and h-OP/SO can be associated with an increase in interphase boundaries after removing the excess fatty acids and extractive molecules, which may ease the polarizability of the particles.

3.3. Dispersion stabilities

The dispersion stability is one of the essential criteria to assess the long-term usage of ER fluids and possible industrial applications. The dispersion stability is desired to be maintained during application, and ER activity is weakened drastically if there is a sedimentation tendency of the dispersed phase. The nature, morphology, size, and surface properties of the dispersed particles, type, and viscosity of the medium, the presence of any stabilizer such as surfactants, and density mismatch between the dispersed phase and carrier fluid are the main factors affecting the dispersion stability. Numerous attempts have been undertaken in the literature to enhance the dispersion stability [33]. The apparent densities of the dispersed particles were determined to evaluate the effect of the density on the dispersion stability. The apparent density of the OP and h-OP were determined as 1.197 ± 0.002 g/cm³ and 1.235 ± 0.010 g/cm³, respectively. The density of carrier fluid, SO, is known as 0.970 g/cm³. The relatively slight density contrast between the dispersed OP and h-OP and the SO may lead to improved dispersion stability.

The OP/SO and h-OP/SO dispersions with various concentrations were allowed to settle undisturbed for one month. Their dispersion stabilities were assessed by measuring the change in anti-sedimentation ratio with time at 25°C. Initially, all the dispersions were in a well-dispersed state (Figure 4). Throughout the settling process, dispersed particles in the fluid gradually settled to the bottom of the container, leaving a relatively clearer carrier fluid above the sediment enriched with particles. Over time, the anti-sedimentation ratio reached an equilibrium value faster at lower and slower at higher concentrations for both samples.

The anti-sedimentation ratios of the dispersions enhanced as the dispersion concentration rose, attributed to the heightened interactions between the dispersed phase and dispersing medium, along with the increase in dispersion viscosity [34]. On the other hand, the effect of gravitational forces on dispersed particles became prominent at lower concentrations, resulting in lower dispersion stability. When the results of SEM analysis and density measurement were evaluated, it was concluded that both samples had similar particle size, morphology, and density values. Thus, the anti-sedimentation ratio improvement from 74 % to 90 % reached at the end of 30 days for 25 wt% was attributed to the improved interfacial adhesion between the carrier fluid and h-OP after Soxhlet extraction by *n*-hexane of OP.

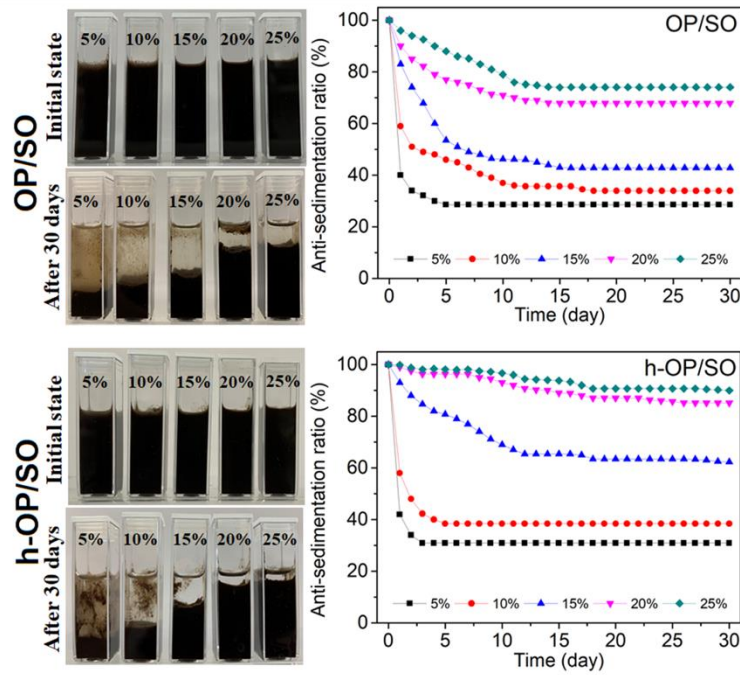


Figure 4. The visual appearance of the OP/SO and h-OP/SO dispersions at the initial of the dispersion stability test and after 30 days of observation for 5–25 wt%, and the change in the anti-sedimentation ratio with time for the OP/SO and h-OP/SO dispersions

3.4. Electrorheological properties

3.4.1. The flow behavior

The steady shear rheological measurements were carried out under appropriate controllable E values to understand the behavior of dispersions to the E . Various rheological models, including Bingham [35], de Kee–Turcotte [36], Herschel–Bulkley [37], Cho–Choi–Jhon (CCJ) [38], or Seo–Seo [39] can be utilized to depict the rheological characteristics of the ER fluids. In this study, the CCJ model (Equation 2) was selected to demonstrate the flow behavior of both dispersions over the shear range examined since the successful fitting curves of shear stress were observed for both dispersions studied. The flow behavior of both ER dispersions across a broad spectrum of shear rates was examined using the CCJ model, and the best-fitting curves (solid curves) are depicted in Figure 5 for 25 wt% concentration.

$$\tau = \frac{\tau_y}{(1 + (t_1\dot{\gamma})^\alpha)} + \eta_\infty \left(1 + \frac{1}{(t_2\dot{\gamma})^\beta}\right)\dot{\gamma} \quad (2)$$

The CCJ model equation comprises six parameters where τ is the shear stress, τ_y is the dynamic yield stress, η_∞ is the viscosity at a high shear rate, $\dot{\gamma}$ is the shear rate, t_1 and t_2 are time constants, and the exponent α is associated with the reduction of shear stress while the exponent β has the range of $0 < \beta \leq 1$ [38]. When subjected to an E , randomly distributed particles were drawn towards each other and linked due to the electric field polarization effect, resulting in the formation of chain/columnar-like structures. In the low shear rate region, the shear stress increased rapidly, and the mechanical shear force was insufficient to break the linking force between electric field-induced particles forming fibrillar or columnar-like structures. Thus, the curve maintained high shear stress at low shear rate values. The shear stress and viscosity values were raised with the increase of the E for both dispersions.

The rates at which fibrillar-like structures, formed through induced electrostatic interactions, are broken down and rebuilt between the dispersed particles under shear force are mainly dependent on the race between electrostatic forces arising from interfacial polarization of dispersed particles and hydrodynamic forces resulting from shear flow within the dispersion [40, 41]. At low $\dot{\gamma}$, electrostatic forces prevailed, while at high $\dot{\gamma}$, hydrodynamic forces disrupted aligned structures and facilitated flow. The electrical-induced structures were then completely broken down, and the shear stress values raised gradually with rising $\dot{\gamma}$, showing Newtonian fluid behavior beyond the critical $\dot{\gamma}$ because there was not enough time for the chain-like structure to reform adequately during swift shear deformation. These changes in the microstructure of dispersed particles led to a significant decrease in viscosity, displaying a shear-thinning behavior. At low E range (0.5–1.5 kV/mm), the breakage of the aligned dispersed particles was not substantial, and a wide plateau emerged in the shear stress until reaching the critical $\dot{\gamma}$. As the E increased to a higher range, the flow curve displayed a decline in shear stress at a moderate $\dot{\gamma}$ values, range due to the apparent destruction rate against the reformation rate of the fibrillar-like structures [39]. Similar behaviors were observed for the dispersions of porous chitosan particles in carrier fluid olive oil [42].

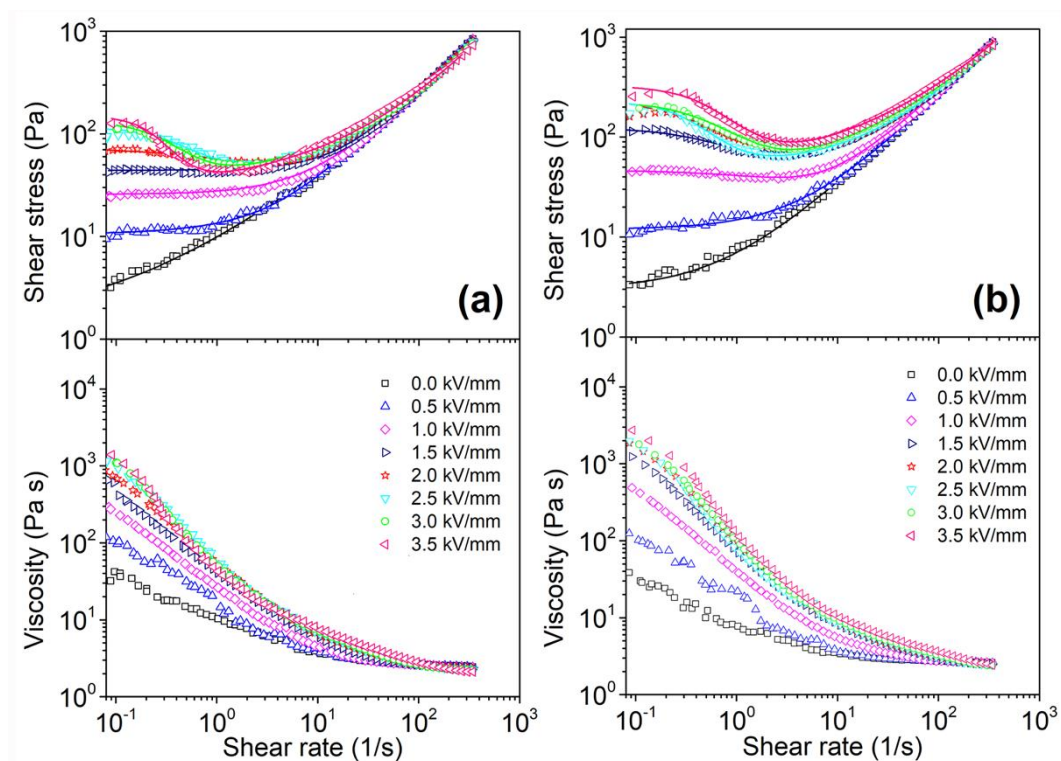


Figure 5. The change in shear stress and viscosity (flow curves) of (a) OP/SO and (b) h-OP/SO dispersions under various E for 25 wt% concentration. The solid curves in the shear stress-shear rate graph shows the best-fitted curves using the Equation 2

The flow curves were obtained for the OP/SO and h-OP/SO dispersions with a series of concentrations between 5–25 wt% to explore how the particle concentration influences the ER performance and to determine the optimum concentration value for further rheological measurements. Therefore, the τ_y values of the dispersions determined according to the Equation 2 were compared. The dependence of the τ_y on the E as a function of OP and h-OP particle mass percentages are shown in Figure 6a and Figure 6b, respectively. The τ_y was increased with increasing particle mass percentage and the E . With increasing E , the shear resistance related to the yield stress was strengthened due to the increased electrostatic forces between the particles arranged in the direction of E . This observation was more pronounced as the particle concentration increased due to the decrease in interparticle distance and the increase in the number of denser

fibrillar/columnar-like structures [43]. On the other hand, the τ_y values displayed two distinct linear trends on the log-log scale with the E , intercepting at $E=2.0$ kV/mm for all dispersions (the dotted lines in Figure 6). After that point, the slope was changed, and the increase in the τ_y with the E was observed to be insignificant. This observation could be attributed to the saturation of the interfacial polarization above this electric field strength [44].

The power law equation describes the correlation between τ_y and E as $\tau_y \propto E^\alpha$, where α serves as the index parameter indicating the slope of the fitted curve on a log-log scale used to evaluate the mechanism of the ER effect. In the case of α is equal to 2 and 1.5, the ER mechanism corresponds to the polarization model and the conduction model, respectively [45]. However, the dispersed particle size and shape, surface characteristics and concentration, as well as the dielectric properties of the dispersion on the τ_y affect this relationship in certain instances [43]. The slope of the τ_y curve was approached from 0.5 to 1.5 and 0.7 to 2.0 as the dispersion mass percentage was increased from 5% to 25% for OP/SO and h-OP/SO dispersion for up to 2 kV/mm, respectively. With increasing the dispersed particle concentration, the behavior approached the conduction and polarization model for the OP/SO and h-OP/SO dispersion, respectively. Therefore, the response of OP particles dispersed in SO under an E indicated that it was primarily influenced by the significant impact of the conductivity mismatch between the particles and the carrier medium [46]. A similar index parameter value of <1.5 was previously reported for various biomaterial-based ER fluids, including α -chitin nanorods [47], porous chitosan [7], phosphorylated potato starch [9], and polypyrrole–silica–methylcellulose composite [48]. The decrease in the index α value (<1.5) was attributed the formation of the non-polarization forces such as hydrogen bonding interactions of the dispersed particles with the carrier fluid and surface polarization saturation [43, 47, 49]. In another study, poly(ionic liquid) based ER fluid whose ER response originated from local ion motion tended to follow the conduction model, whereas its composite with polyaniline led to incline to polarization model [50]. On the other hand, h-OP/SO dispersion was consistent with the polarization model, whose α value was 2.0, indicating that the removal of fatty acids and extractives contributes to the enhancement of polarization of OP particles by decreasing the non-polarization forces. In a study, nanocellulose particles dispersed in castor oil containing ricinoleic acid were reported to exhibit the index parameter approaching 1.5 with increasing concentration, due to the hindering of the electrostatic forces because of H-bonding or van der Waals interactions between the hydroxyl groups in the nanocellulose particles and the carrier fluid castor oil [44].

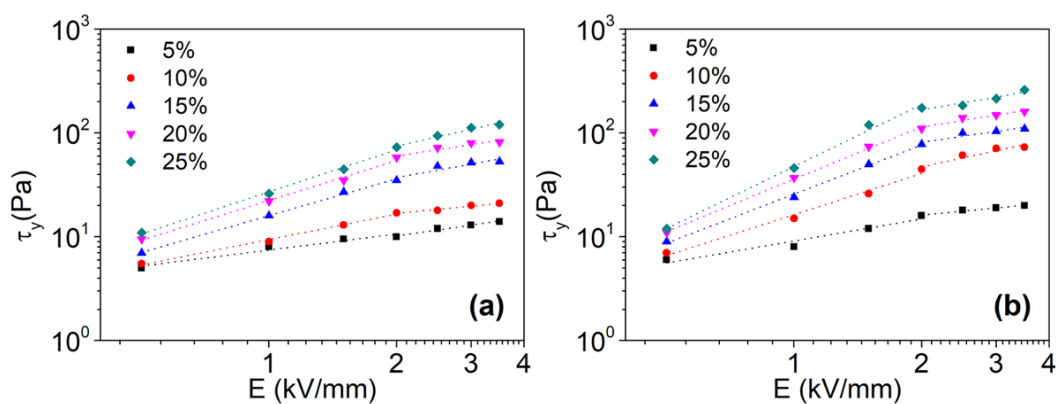


Figure 6. The yield stress as a function of the E for (a) OP/SO and (b) h-OP/SO dispersions for concentrations between 5 to 25 wt%, the dotted lines show the trendlines of a power-law scaling

3.4.2. Oscillation rheology results

The viscoelastic characteristics of the OP/SO and h-OP/SO dispersions (25 wt%) were examined by the dynamic oscillation experiments. The shear stress sweep test was conducted firstly to determine the LVER of the dispersions at a constant frequency of 1 Hz, as shown in Figure 7a. The elastic modulus (G') values were independent of the applied shear stress in the LVER and increased with the E . Furthermore, the enhanced polarization forces between the particles led to a shift of the LVER to higher shear stresses with increasing E . At the end of the plateau region, the electrical-induced fibrillar structures became broken, and the G' values began to decrease by the applied oscillatory shear deformation. The G' was increased by around 12 and 35 times for OP/SO and h-OP/SO dispersions, respectively, under 3.0 kV/mm in the LVER compared to off-field conditions, indicating h-OP/SO dispersion showed significantly greater elastic dominant character than OP/SO dispersion.

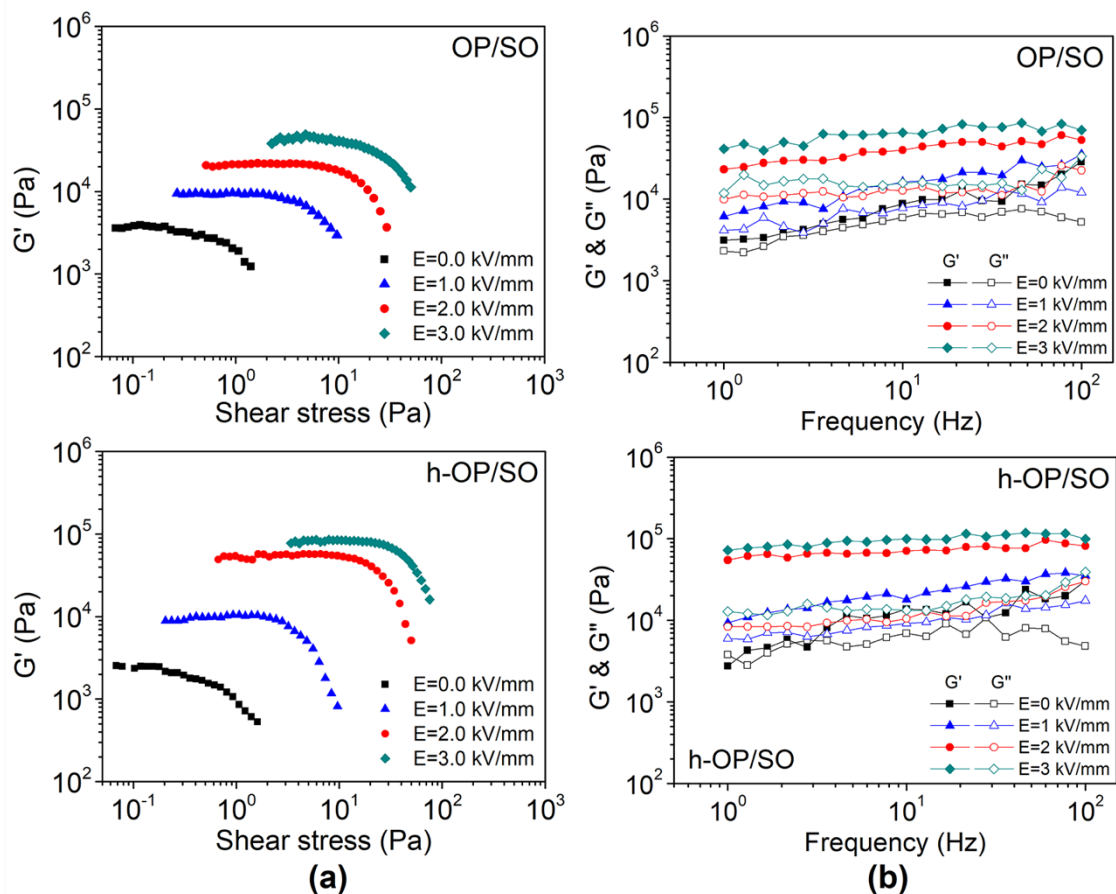


Figure 7. (a) The shear stress dependence of G' and (b) the frequency dependence of the G' and G'' for OP/SO and h-OP/SO dispersions

Secondly, the change in G' and viscous modulus (G'') values of both dispersions were determined as a function of the frequency in the range of 1–100 Hz at constant stress values in the previously determined LVER at various E values, as shown in Figure 7b. In the off-field, the G' slightly exceeded the G'' within the studied frequency range and both moduli values increased with frequency for both dispersions. Thus, the OP/SO and h-OP/SO dispersions behaved like weak gel and confirmed the presence of the low yield stress values at 25 wt% concentrations obtained from the steady shear flow curve tests. The main reason for such gel-like formation without the E could be attributed to the percolation network formation and the structural organization of the dispersed particles due to the restricted motions through dominant attraction forces between them. The formation of similar percolation networks for various particles such as clay [51],

detonation nanodiamond [52], and porous chitosan particles [7] were reported, and the reasons were attributed to the particle anisotropy.

With the E , the G' values dramatically exceeded the G'' and reached about 65 kPa and 100 kPa at the electric field of 3 kV/mm for OP/SO and h-OP/SO, respectively, demonstrating that the predominant behavior was solid-like, characterized by a stable plateau region, rather than viscous. The G' values of h-OP/SO dispersion were 1.5 times greater than that of OP/SO dispersion under E , indicating the enhanced polarization ability and higher solidification of h-OP dispersion. The moduli values were increasing with E , indicating that the electrical-induced fibrillar structures of the OP/SO and h-OP/SO dispersions were not broken in the studied frequency range, and the elastic and solid-like properties of the dispersions were strengthened with E . The increased gap between the values of G' and G'' with increasing the E demonstrated the increase in the elastic component of the dispersions.

3.4.3. Creep and recovery results

In a creep recovery test, the deformation behavior of a material is evaluated by initially measuring the strain under a constant shear stress load, followed by unloading, over a specified duration at a constant temperature. After the stress is removed, there is only a partial recovery that is controlled by the retardation and the corresponding creep for viscoelastic materials, and the recovery ratio (χ) was defined to evaluate the contribution of the elastic character of the ER fluid and calculated using the following Equation 3 [53]:

$$\chi = \frac{\gamma_i - \gamma_f}{\gamma_i} \quad (3)$$

where γ_i denotes the achieved strain prior to the removal of the applied shear stress (τ_0), while γ_f represents the strain following the removal of the τ_0 . A creep-recovery test was conducted to monitor the deformation and recovery of the electrically induced structures over time, and the recorded strain as a function of time under various E for the optimum dispersion, h-OP/SO, is presented in Figure 8.

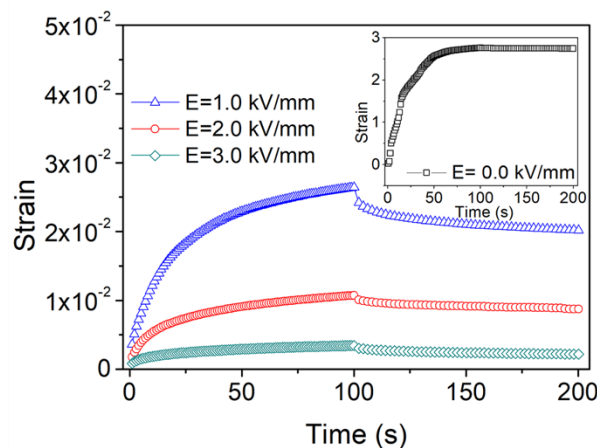


Figure 8. Changes in strain over time at different levels of E during the creep-recovery test for h-OP/SO. The creep-recovery curve of h-OP/SO for off-field is displayed in the inset figure ($\tau_0 = 5$ Pa for the first 100 s and then $\tau_0 = 0$ Pa, 25 wt%).

Upon stress loading, an instantaneous strain appeared and subsequently escalated over time, reaching a maximum value indicating time-dependent nonlinear deformation under constant stress. After the removal of the stress loading, subsequent time-dependent reformations were observed under E . In contrast, almost no recovery was observed

without the presence of the E , as shown in the inset figure in Figure 8. The strain values obtained during the creep-recovery test decreased as E increased, suggesting the formation of a more robust solid-like structure with increasing E [33]. For the h-OP/SO dispersion, the recovery ratios with increasing E were observed to enhance as following: $\chi_{E=1\text{kV/mm}}=0.27 < \chi_{E=2\text{kV/mm}}=0.42 < \chi_{E=3\text{kV/mm}}=0.48$, suggesting increased elastic response among particles at higher E .

4. Conclusion

By considering environmental issues, the utilization of nontoxic and eco-friendly products as a component of ER fluids is highly desired. With this respect, the agricultural organic waste, the olive pulp (OP), discarded after the olive oil extraction process consisting of sustainable biomass sources, was upcycled as an electric field-responsive smart fluid. The OP was further subjected to Soxhlet extraction by n -hexane to remove excess residual fatty acids and small molecules that existed in the raw OP. Structural, thermal, morphological, and electrical characterizations of the OP and n -hexane treated OP (h-OP) samples were performed. Successful removal of the excess oil, fatty acid, and residual small molecules in the OP was revealed by ATR-FTIR, elemental analysis, and TG/DTG analysis. The conductivities of the OP and h-OP were determined to be in the desired semiconducting range for the ER fluids, and relatively lower conductivity was obtained for h-OP compared to OP. Also, the h-OP dispersion showed a relatively higher magnitude of interfacial polarization and shorter relaxation time than that of the OP dispersion due to the improved polarization resulting from the increase in interphase boundaries after the Soxhlet extraction process and decreased nonpolarized forces. The enhanced dispersion stability was determined for h-OP dispersion. Both control shear rate flow curve and oscillation rheological analysis results under the E indicated that Soxhlet extraction led the OP to display stronger electric field response and higher ER activity. This study suggests that OP, an agricultural industrial waste that occurs in high amounts in the olive oil production process, is a good candidate for upcycling in the field of electric field responsive smart fluids due to its higher dispersion stability and ER activity after being subjected to the pre-washing process by n -hexane.

Authorship contribution statement

Ö. Erol: Conceptualization, Methodology, Investigation, Data Curation, Visualization, Original Draft Writing, Review and Editing.

Declaration of competing interest

The author declares that she has no known competing financial interests or personal relationships that could have appeared to influence the work reported in this paper.

Acknowledgment

The author expresses her gratitude to Prof. Dr. H.İ. Ünal (Gazi University, Science Faculty, Chemistry Department) for giving the opportunity to provide the laboratory facility for rheological and electrical studies.

Ethics Committee Approval and/or Informed Consent Information

As the author of this study, I declare that I do not have any ethics committee approval and/or informed consent statement.

References

- [1] F. P. La Mantia, M. Morreale, "Green composites: A brief review", *Composites Part A: Applied Science and Manufacturing*, 42(6), 579-588, 2011.
- [2] N. M. Kuznetsov, V. V. Kovaleva, S. I. Belousov, S. N. Chvalun, "Electrorheological fluids: From historical retrospective to recent trends", *Materials Today Chemistry*, 26,101066, 2022.
- [3] K. Zhang, H. J. Choi, "Smart polymer/carbon nanotube nanocomposites and their electrorheological response", *Materials*, 7(5), 3399-3414, 2014.
- [4] V. I. Kordonsky, E. V. Korobko, T. G. Lazareva, "Electrorheological polymer-based suspensions", *Journal of Rheology*, 35(7), 1427-1439, 1991.
- [5] Y. G. Ko, S. S. Shin, U. S. Choi, Y. S. Park, J. W. Woo, "Gelation of chitin and chitosan dispersed suspensions under electric field: Effect of degree of deacetylation", *ACS Applied Materials & Interfaces*, 3(4), 1289-1298, 2011.
- [6] Y. G. Ko, H. J. Lee, S. S. Shin, U. S. Choi, "Dipolar-molecule complexed chitosan carboxylate, phosphate, and sulphate dispersed electrorheological suspensions", *Soft Matter*, 8(23), 6273-6279, 2012.
- [7] N. M. Kuznetsov, Y. D. Zagoskin, A. Y. Vdovichenko, A. V. Bakirov, R. A. Kamyshinsky, A. P. Istomina, T. E. Grigoriev, S. N. Chvalun, "Enhanced electrorheological activity of porous chitosan particles", *Carbohydrate Polymers*, 256, 117530, 2021.
- [8] K. Negita, H. Itou, T. Yakou, "Electrorheological effect in suspension composed of starch powder and silicone oil", *Journal of Colloid and Interface Science*, 209(1), 251-254, 1999.
- [9] J. H. Sung, D. P. Park, B. J. Park, H. J. Choi, M. S. Jhon, "Phosphorylation of potato starch and its electrorheological suspension", *Biomacromolecules*, 6(4), 2182-2188, 2005.
- [10] M. Yavuz, T. Tilki, C. Karabacak, O. Erol, H. I. Unal, M. Uluturk, M. Cabuk, "Electrorheological behavior of biodegradable modified corn starch/corn oil suspensions", *Carbohydrate Polymers*, 79(2), 318-324, 2010.
- [11] Y. G. Ko, H. J. Lee, Y. J. Chun, U. S. Choi, K. P. Yoo, "Positive and negative electrorheological response of alginate salts dispersed suspensions under electric field", *ACS Applied Materials & Interfaces*, 5(3), 1122-1130, 2013.
- [12] B. Sim, D. H. Bae, H. J. Choi, K. Choi, M. S. Islam, N. Kao, "Fabrication and stimuli response of rice husk-based microcrystalline cellulose particle suspension under electric fields", *Cellulose*, 23(1), 185-197, 2016.
- [13] D. H. Bae, H. J. Choi, K. Choi, J. D. Nam, M. S. Islam, N. Kao, "Fabrication of phosphate microcrystalline rice husk based cellulose particles and their electrorheological response", *Carbohydrate Polymers*, 165, 247-254, 2017.
- [14] S. H. Kwon, I. H. Park, C. M. Vu, H. J. Choi, "Fabrication and electro-responsive electrorheological characteristics of rice husk-based nanosilica suspension", *Journal of the Taiwan Institute of Chemical Engineers*, 95, 432-437, 2019.
- [15] Y. Chun, Y. G. Ko, T. Do, Y. Jung, S. W. Kim, U. Su Choi, "Spent coffee grounds: Massively supplied carbohydrate polymer applicable to electrorheology", *Colloids and Surfaces A: Physicochemical and Engineering Aspects*, 562, 392-401, 2019.
- [16] P. Otero, P. Garcia-Oliveira, M. Carpena, M. Barral-Martinez, F. Chamorro, J. Echave, P. Garcia-Perez, H. Cao, J. Xiao, J. Simal-Gandara, M. A. Prieto, "Applications of by-products from the olive oil processing: Revalorization strategies based on target molecules and green extraction technologies", *Trends in Food Science & Technology*, 116, 1084-1104, 2021.
- [17] G. Espadas-Aldana, P. Guaygua-Amaguaña, C. Vialle, J.-P. Belaud, P. Evon, C. Sablayrolles, "Life cycle assessment of olive pomace as a reinforcement in polypropylene and polyethylene biocomposite materials: A new perspective for the valorization of this agricultural by-product", *Coatings*, 11(5), 525, 2021.
- [18] M. Volpe, D. Wüst, F. Merzari, M. Lucian, G. Andreottola, A. Kruse, L. Fiori, "One stage olive mill waste streams valorisation via hydrothermal carbonisation", *Waste Management*, 80, 224-234, 2018.
- [19] S. Sismanoglu, U. Tayfun, C.-M. Popescu, Y. Kanbur, "Effective use of olive pulp as biomass additive for eco-grade TPU-based composites using functional surface modifiers", *Biomass Conversion and Biorefinery*, 13, 12303-12318, 2023.
- [20] M. J. Pancholi, A. Khristi, K. M. Athira, D. Bagchi, "Comparative analysis of lignocellulose agricultural waste and pre-treatment conditions with FTIR and machine learning modeling", *BioEnergy Research*, 16(1), 123-137, 2023.
- [21] H. M. Boundzanga, B. Cagnon, M. Roulet, S. de Persis, C. Vautrin-UI, S. Bonnamy, "Contributions of hemicellulose, cellulose, and lignin to the mass and the porous characteristics of activated carbons produced from biomass residues by phosphoric acid activation", *Biomass Conversion and Biorefinery*, 12(8), 3081-3096, 2022.
- [22] A. I. Martín García, A. Moumen, D. R. Yáñez Ruiz, E. Molina Alcaide, "Chemical composition and nutrients availability for goats and sheep of two-stage olive cake and olive leaves", *Animal Feed Science and Technology*, 107(1), 61-74, 2003.

- [23] V. Benavente, A. Fullana, "Torrefaction of olive mill waste", *Biomass and Bioenergy*, 73, 186-194, 2015.
- [24] S. Lammi, A. Barakat, C. Mayer-Laigle, D. Djenane, N. Gontard, H. Angellier-Coussy, "Dry fractionation of olive pomace as a sustainable process to produce fillers for biocomposites", *Powder Technology*, 326, 44-53, 2018.
- [25] R. Font, M. D. Rey, "Kinetics of olive oil pyrolysis", *Journal of Analytical and Applied Pyrolysis*, 103, 181-188, 2013.
- [26] M. Wzorek, R. Junga, E. Yilmaz, B. Bozhenko, "Thermal decomposition of olive-mill byproducts: A tg-ftir approach", *Energies*, 14(14), 4123, 2021.
- [27] T. Akar, I. Tosun, Z. Kaynak, E. Ozkara, O. Yeni, E. N. Sahin, S. T. Akar, "An attractive agro-industrial by-product in environmental cleanup: Dye biosorption potential of untreated olive pomace", *Journal of Hazardous Materials*, 166(2), 1217-1225, 2009.
- [28] Y. Z. Dong, H. M. Kim, H. J. Choi, "Conducting polymer-based electro-responsive smart suspensions", *Chemical Papers*, 75(10), 5009-5034, 2021.
- [29] J. K. Jung, Y. I. Moon, G. H. Kim, N. H. Tak, "Characterization of dielectric relaxation process by impedance spectroscopy for polymers: Nitrile butadiene rubber and ethylene propylene diene monomer", *Journal of Spectroscopy*, 2020, 8815492, 2020.
- [30] S. Havriliak, S. Negami, "A complex plane analysis of α -dispersions in some polymer systems", *Journal of Polymer Science Part C: Polymer Symposia*, 14(1), 99-117, 1966.
- [31] N. M. Kuznetsov, V. V. Kovaleva, A. Y. Vdovichenko, S. N. Chvalun, "Natural electrorheological fluids based on cellulose particles in olive oil: The filler size effect", *Colloid Journal*, 85(3), 408-417, 2023.
- [32] M. Hasanin, A. M. Labeeb, "Dielectric properties of nicotinic acid/methyl cellulose composite via "green" method for anti-static charge applications", *Materials Science and Engineering: B*, 263, 114797, 2021.
- [33] O. Erol, H. I. Unal, "Core/shell-structured, covalently bonded TiO₂/poly(3,4-ethylenedioxythiophene) dispersions and their electrorheological response: The effect of anisotropy", *RSC Advances*, 5(125), 103159-103171, 2015.
- [34] G. T. Ngatu, N. M. Wereley, J. O. Karli, R. C. Bell, "Dimorphic magnetorheological fluids: Exploiting partial substitution of microspheres by nanowires", *Smart Materials and Structures*, 17(4), 045022, 2008.
- [35] E. C. Bingham, *Fluidity and Plasticity*, New York, McGraw-Hill Book Company, Inc., 440 pages, 1922.
- [36] D. D. Ké, G. Turcotte, "Viscosity of biomaterials", *Chemical Engineering Communications*, 6(4-5), 273-282, 1980.
- [37] W. H. Herschel, R. Bulkley, "Konsistenzmessungen von gummi-benzollösungen", *Kolloid-Zeitschrift*, 39(4), 291-300, 1926.
- [38] M. S. Cho, H. J. Choi, M. S. Jhon, "Shear stress analysis of a semiconducting polymer based electrorheological fluid system", *Polymer*, 46(25), 11484-11488, 2005.
- [39] Y. P. Seo, Y. Seo, "Modeling and analysis of electrorheological suspensions in shear flow", *Langmuir*, 28(6), 3077-3084, 2012.
- [40] L. I. Linzhi, G. A. O. Shujuan, "Polyaniline (PANI) and BaTiO₃ composite nanotube with high suspension performance in electrorheological fluid", *Materials Today Communications*, 24, 100993, 2020.
- [41] J.-Y. Hong, M. Choi, C. Kim, J. Jang, "Geometrical study of electrorheological activity with shape-controlled titania-coated silica nanomaterials", *Journal of Colloid and Interface Science*, 347(2), 177-182, 2010.
- [42] N. M. Kuznetsov, Y. D. Zagoskin, A. V. Bakirov, A. Y. Vdovichenko, S. N. Malakhov, A. P. Istomina, S. N. Chvalun, "Is chitosan the promising candidate for filler in nature-friendly electrorheological fluids?", *ACS Sustainable Chemistry & Engineering*, 9(10), 3802-3810, 2021.
- [43] S. Y. Oh, T. J. Kang, "Electrorheological response of inorganic-coated multi-wall carbon nanotubes with core-shell nanostructure", *Soft Matter*, 10(21), 3726-3737, 2014.
- [44] M. A. Delgado-Canto, S. D. Fernández-Silva, C. Roman, M. García-Morales, "On the electro-active control of nanocellulose-based functional biolubricants", *ACS Applied Materials & Interfaces*, 12(41), 46490-46500, 2020.
- [45] B. Zhang, Y. Chen, H. Zheng, C. Li, L. Ma, H. Zhang, B. Wang, C. Hao, "Composites of co-doped graphitic C₃N₄ nanosheets and TiO₂ nanoparticles for electrorheological fluid applications", *ACS Applied Nano Materials*, 5(1), 1003-1015, 2022.
- [46] J. Liu, X. Wen, Z. Liu, Y. Tan, S. Yang, P. Zhang, "Electrorheological performances of poly(o-toluidine) and p-toluenesulfonic acid doped poly(o-toluidine) suspensions", *Colloid and Polymer Science*, 293(5), 1391-1400, 2015.

- [47] V. V. Kovaleva, N. M. Kuznetsov, A. P. Istomina, O. I. Bogdanova, A. Y. Vdovichenko, D. R. Streltsov, S. N. Malakhov, R. A. Kamyshinsky, S. N. Chvalun, "Low-filled suspensions of α -chitin nanorods for electrorheological applications", *Carbohydrate Polymers*, 277, 118792, 2022.
- [48] D. J. Yoon, Y. D. Kim, "Synthesis and electrorheological behavior of sterically stabilized polypyrrole-silica-methylcellulose nanocomposite suspension", *Journal of Colloid and Interface Science*, 303(2), 573-578, 2006.
- [49] X. Huang, W. Wen, S. Yang, P. Sheng, "Mechanisms of the giant electrorheological effect", *Solid State Communications*, 139(11), 581-588, 2006.
- [50] C. Zheng, Q. Lei, J. Zhao, X. Zhao, J. Yin, "The effect of dielectric polarization rate difference of filler and matrix on the electrorheological responses of poly(ionic liquid)/polyaniline composite particles", *Polymers*, 12(3), 703, 2020.
- [51] R. K. Pujala, H. B. Bohidar, "Slow dynamics and equilibrium gelation in fractionated montmorillonite nanoplatelet dispersions", *Colloid and Polymer Science*, 297(7), 1053-1065, 2019.
- [52] N. M. Kuznetsov, S. I. Belousov, A. V. Bakirov, S. N. Chvalun, R. A. Kamyshinsky, A. A. Mikhutkin, A. L. Vasiliev, P. M. Tolstoy, A. S. Mazur, E. D. Eidelman, E. B. Yudina, A. Y. Vul, "Unique rheological behavior of detonation nanodiamond hydrosols: The nature of sol-gel transition", *Carbon*, 161, 486-494, 2020.
- [53] Y. D. Liu, X. Quan, B. Hwang, Y. K. Kwon, H. J. Choi, "Core-shell-structured monodisperse copolymer/silica particle suspension and its electrorheological response", *Langmuir*, 30(7), 1729-1734, 2014.

Experimental and Theoretical Monitoring of the Adsorption of 2,4-Dimethylphenol on *Coturnix Coturnix Japonica* Eggshell

Belgin Tunalı¹, Deniz Türköz Altuğ², Taner Kalaycı³, Neslihan Kaya Kınaytürk^{4*}

¹ Department of Nanoscience and Nanotechnology, Faculty of Arts and Sciences, Burdur Mehmet Akif Ersoy University, 15030, Burdur, TURKEY

<https://orcid.org/0000-0003-0768-679X>

² Department of Science Education, Faculty of Education, Süleyman Demirel University, East Campus, 32260, Isparta, TURKEY

<https://orcid.org/0000-0002-1861-6263>

³ Department of Opticianry, Vocational School of Health Services, Bandırma Onyedi Eylül University, 10200, Balıkesir, TURKEY

<https://orcid.org/0000-0002-6374-2373>

⁴ Department of Nanoscience and Nanotechnology, Faculty of Arts and Sciences, Burdur Mehmet Akif Ersoy University, 15030, Burdur, TURKEY

*corresponding author: nkinayturk@mehmetakif.edu.tr

<https://orcid.org/0000-0002-2170-1223>

(Received: 21.04.2024, Accepted: 05.09.2024, Published: 25.11.2024)

Abstract: Phenolic compounds are serious risks to both the environment and human health. It has led to an increase in the number of scientific studies on the elimination of these pollutants. Among these compounds, 2,4-Dimethylphenol is particularly common and therefore of significant concern. This study investigates the removal of this chemical using pure and calcined *Coturnix-Coturnix Japonica* eggshells as adsorbents. For theoretical calculations of 2,4-Dimethylphenol, the Density Functional Theory B3LYP/ 6311++G(d,p) basis set is used. These calculations provided information about the molecule's geometry, molecular electrostatics potential surface map, frontier molecular orbitals, and chemical activity values. To validate the experimental findings, theoretical infrared spectra for 2,4- Dimethylphenol were calculated and compared with experimental results. Then, the adsorption process of 2,4-Dimethylphenol on pure and calcined eggshells was described. Experimental infrared spectral results were supported by theoretical calculations and approved the adsorption process via strong wavenumbers in the related spectrum. The surface morphology of eggshells was characterized using light microscopy, Atomic Force Microscopy, and Scanning Electron Microscopy.

Additionally, demonstrated strong agreement between experimental and theoretical infrared spectra for pure 2,4- Dimethylphenol. Post-adsorption Infrared spectral analysis showed that 2,4- Dimethylphenol adsorbed to calcined eggshells. This study highlights the potential of mentioned eggshells as natural, promising materials for environmental remediation and pollution control. Thus, it can contribute to improving environmental and human health.

Key words: 2,4-dimethylphenol, Adsorption, Eggshell, *Coturnix Coturnix Japonica*, DFT

1. Introduction

Phenols derived from benzene exhibit various chemical reactivity and physical properties. These characteristics make them integral components in numerous industries, including pharmaceuticals [1], agricultural [2], personal care [3], and daily applications [4]. 2,4-Dimethylphenol (2,4-DMP) is formed by substituting the methyl groups to the phenol ring. [5]. It can also be explained as benzene ring which substitute hydroxyl and methyl groups. It is also called 2,4-Xylenol. 2,4-DMP is a compound widely used in the world, such as disinfectants, and antiseptics [4], wood preservatives [6], chemical intermediates [7].

However, 2,4-DMP; is a toxic, carcinogenic, endocrine disruption, air, water, and soil pollutant, making it harmful to humans and wildlife [4, 8-10]. Industrial processes and combustion activities [11] are among the reasons why 2,4-DMP causes air pollution. These processes can cause both smog and respiratory ailense. Removal techniques such as adsorption onto activated carbon, cleaning with chemical reagents, and catalytic oxidation provide effective means to reduce airborne 2,4-DMP levels and improve air quality [12]. In addition, advances in photocatalysis [13] are promising for degrading 2,4-DMP molecules into harmless byproducts. 2,4-DMP creates difficulties in water and wastewater treatment due to its persistence and resistance to traditional treatment methods [14-16]. Physical processes such as filtration and membrane separation can effectively remove to particulate 2,4-DMP [17]. Chemical processes involving oxidation with ozone or chlorine, as well as advanced oxidation processes (AOPs) such as UV/H₂O₂ or UV/O₃, are used to degrade dissolved 2,4-DMP [13, 18].

Soil contamination with 2,4-DMP, which often results from agricultural practices, industrial leaks, or improper disposal of waste, requires remediation strategies to prevent its accumulation in food crops and groundwater [6, 9]. Soil washing [19], bioremediation using microbial degradation [20] and phytoremediation [21], which uses plants to uptake and detoxify 2,4-DMP, are among the techniques used to reduce soil pollution. Activities aimed at reducing the negative effects of phenols on the environment and living things are one of the most current research topics. When research was conducted on WoS (Web of Science) using the words “phenols and environment” and “phenols and remove” in the last 10 years, it was observed that the studies on these subjects increased. (Supplementary Figure1)

Eggshells have a physical and chemical structure to be used not only in the protection of developing embryo, but also especially in adsorption processes. Their porous structure, which has an internal order in terms of physical properties, and their chemical composition of approximately 94% calcium carbonate, make eggshells effective supplement for a wide variety of substances [22-24]. The adsorbent property of eggshells stems from their porous structure allows physical and chemical interaction with surrounding molecules and ions [25, 26-28]. Calcining eggshells by burning them at an average of 800 °C allows them to increase their adsorption capacity [29].

In environmental applications, eggshells have received great attention as cost-effective and environmentally friendly adsorbents for the removal of pollutants from air, water, and soil. Research has shown the effectiveness of eggshells in adsorbing heavy metals, organic pollutants, and dyes, offering promising solutions to reduce environmental pollution and improve water quality [25-28, 30]. The abundance and low cost of eggshells make them attractive alternatives to traditional adsorbents, contributing to sustainable and environmentally responsible practices in various industries. As a result of the screening, there is a potential to remove phenols from the environment, generally through eggshells.

There are almost no studies on the removal of 2,4-DMP from the environment via eggshell. In this work, it has been researched that 2,4-DMP can be removed from the environment by using the adsorption feature of *Coturnix-Coturnix Japonica* (CCJ) and calcined *Coturnix-Coturnix Japonica* (C-CCJ) eggshells. In this way, it is thought that this study can be evaluated in terms of environmental improvement processes, pollution control and the protection of human health.

2. Material and Method

2.1. Experimental details

The CCJ eggshell was washed, then separated from its membrane, boiled with pure water at 110°C for 2 hours and left to dry at room temperature. In addition to that, calcination was carried out at 800 °C for 2 hours. Fourier Transform Infrared Spectroscopy (FTIR) analyses of CCJ eggshells were performed before and after calcination. A stereo microscope, Scanning Elektron Microscope (SEM) image and Atomic Force Microscope (AFM) image of the CCJ were taken. Adsorption with 2,4-DMP (Sigma Aldrich) on CCJ eggshell samples was carried out for 72 hours. 2,4-DMP was not subjected to any purification process. The filtered samples were washed with ethanol. FTIR analyses were performed again. 2,4-DMP was analyzed in the range of 200-300 nm using an Ultraviolet Visible (UV-Vis) spectrophotometer.

2.2. Computational details

The software package Gaussian 09 was utilized to do the theoretical computations. The B3LYP functional and 6-311++G(d,p) basis sets were used in the density functional theory (DFT) approach to produce results for quantum chemical calculations [31]. The harmonic force field of the cluster was evaluated via scaled quantum mechanical force field suggested by Pulay et al.[32] Potential Energy Distributions of the cluster were computed by MOLVIB [33, 34]. The computed wavenumbers by DFT/B3LYP/6-311++G(d,p) level of theory were scaled to provide acceptable agreement between experimental and calculated wavenumbers. The following scale factors were applied; O-H stretch 0.88; C-H stretch 0.95; C-H deformation 0.92; all others 0.98. The GaussView software was used to visualize the results. A Schematic representation of 2,4-DMP is shown in Figure 1. The optical properties, encompassing the ultraviolet-visible (UV-Vis) spectrum and excitation energy, were derived through time-dependent density functional theory (TD-DFT) calculations employing the CAM-B3LYP functional, while also accounting for solvation effects in chloroform. Incorporating solvent effects in theoretical computations is essential for achieving a satisfactory alignment between theoretical predictions and experimental spectral data. In this investigation, the excitation energy was computed utilizing the integral equation formalism of the polarizable continuum model (IEF-PCM) [35, 36].

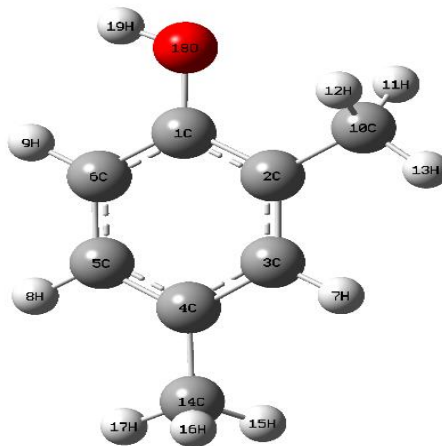


Figure 1. Schematic representation of 2,4-DMP

3. Results

3.1. Molecular geometry

The 2,4-DMP molecule is formed by bonding methyl to the 2nd and 4th carbon atoms of the benzene atom and OH to the 5th carbon atom. The bond angle and bond length calculation results showing the geometric structure of this molecule are presented in Supplementary Table 1.

Bond lengths may elongate or shorten as a result of orbital interactions and the charge distribution within the molecular structure. The presence of electronegative atoms induces charge transfers, resulting in changes in the lengths of C–O, C–N, and C–C bonds [37]. According to the table, when the bond lengths in the aromatic ring are evaluated, the C1-C2 bond length has the highest value (1.4046 Å), while the shortest bond length is calculated as well as C1-C6 (1.3910 Å). The theoretical structural parameters of 2,4-dimethylphenol (2,4-DMP) were compared with the experimental structural parameters of phenol [38]. The O-H bond length in phenol was determined to be 0.957 Å, while in 2,4-DMP it was calculated as 0.9624 Å. The C-O bond length was 1.3750 Å in phenol and 1.3719 Å in 2,4-DMP which it is calculated in this work (Supplementary Table 1). In the phenol molecule, C-C bond lengths range from 1.391 Å to 1.395 Å. Similarly, in 2,4-DMP, the C-C bond lengths vary between 1.391 Å and 1.405 Å. This indicates a remarkable consistency between these two similar structures.

The bond lengths of all C-H bonds in the methyl group were calculated to be in the range of 1.0915-1.0951 Å, and the C-H bond lengths in the aromatic structure were calculated between in the range of 1.0850-1.0868 Å. When looking at the bond angles in the 2,4-DMP molecule, the smallest bond and biggest bond angle values in the aromatic ring of this molecule were determined as C3-C4-C5 (117.7287°) and C2-C3-C4 (122.8751°), respectively. The bond angles in the methyl group are smaller than that of the aromatic structure.

3.2. Molecular electrostatic potential surface (MEP)

The charge distribution and changeable charge region of molecules are shown by molecular electrostatic potential surface maps, or MEPs. The charge distribution is frequently used to predict aspects of hydrogen bonding, molecular behavior, structural

activity, electrophilic and nucleophilic reactivity, and intermolecular interaction [37], [38]. Furthermore, by locating active areas in chemical bonds, MEP maps play a critical role in the development of novel techniques for chemical synthesis. The color-coded electrostatic potential surface map is shown in Figure 2. The increments are in the following order: green, blue, orange, yellow and red [39]. On the molecule's MEP map, the region with low electron density is marked in blue, and the region with high electron density is coded in red [40]. The range of -0.0635 a.u. to +0.0635 a.u. represents the regions with the highest negative to highest positive potential for the 2,4-DMP molecule. The most electronegative region is the relative red zone, which is concentrated on the O atom and is made up of displaced pi electrons in the middle of the phenyl rings. Blue-coded sections are the most positively nucleophilic and are next to the H atom in the OH group.

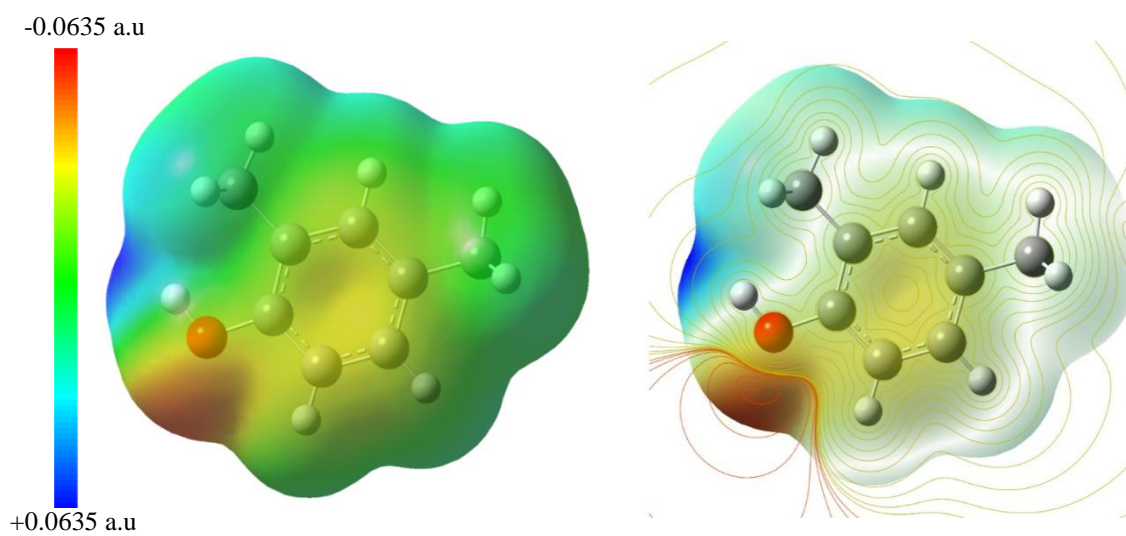


Figure 2. Molecular electrostatic potential mapped of 2,4-DMP

3.3. Frontier molecular orbitals (FMOs) and chemical activity

Among the molecular orbitals, LUMO denotes the lowest unoccupied molecular orbital and HOMO denotes the highest occupied molecular orbital. The HOMO and LUMO energies are recognized as crucial variables in quantum chemistry [41]. For instance, a molecule's HOMO energy directly represents its ionization potential, whereas LUMO represents the molecule's electron affinity. Additionally, the chemical stability of a molecule and the electric charge flow characteristics are ascertained by analyzing the energy gap between HOMO and LUMO. Like this, the HOMO and LUMO energy values dictate several of the molecule's distinctive characteristics. The quantum chemical formulas that are derived from HOMO and LUMO energies are listed below [42].

$$\text{Ionization energy } I = -E_{\text{HOMO}}$$

$$\text{Electron affinity } A = -E_{\text{LUMO}}$$

$$\text{Hardness } \eta = (I-A)/2$$

$$\text{Softness } S = 1 / 2\eta$$

$$\text{Mulliken electronegativity parameter } \chi = (I+A)/2$$

$$\text{Electrophilic index } w = \mu^2 / 2\eta,$$

$$\text{Chemical potential } \mu = -(I+A)/2$$

$$\text{Maximum charge transfer parameter } \Delta N_{\text{max}} = (I+A)/2(I-A)$$

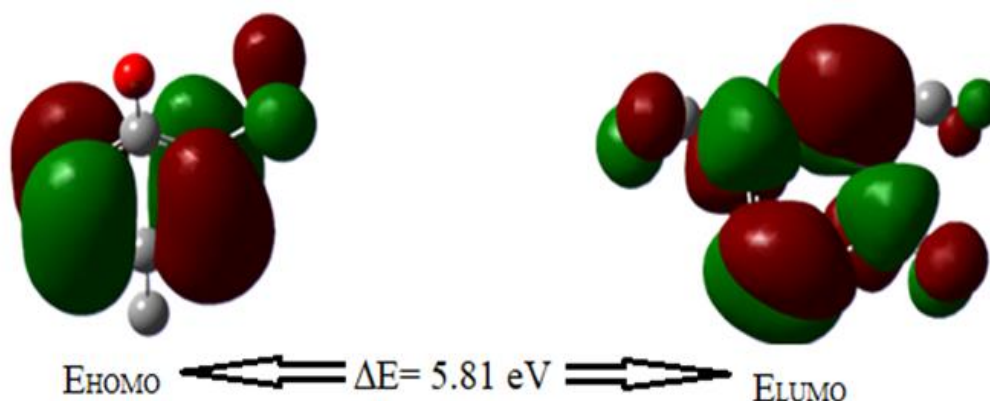


Figure 3. HOMO-LUMO Plot of 2,4-DMP

Figure 3 displays the HOMO and LUMO surface pictures, while Table 1 provides the calculated values. Because of their large energy gaps, the data demonstrate that 2,4-DMP possesses high hardness and low softness properties. These suggest that this molecule has high kinetic stability and low chemical activity, indicating its stability. The chemical reactivity descriptors show that low softness and high hardness values indicate less intermolecular charge transfer and, hence, poor polarity. With the use of frontier molecular orbital (FMO) analysis, we were able to determine that the methyl groups and phenyl rings (as π -type bonding) are where the molecular orbitals of HOMO and LUMO in 2,4-DMP are concentrated (Figure. 3). The value of HOMO energy is -6.27 eV . The value of LUMO energy is -0.46 eV . Furthermore, a projected energy gap of 5.81 eV exists between the HOMO and LUMO orbitals (Table 1). These small HOMO–LUMO energy gaps demonstrate that 2,4-DMP is the site of the charge transfer. Electrons travel from high chemical potential to low chemical potential in molecules, moving from one with a low χ to one with a high χ . The definition of the χ value in the title molecule is 3.37 eV . For 2,4-DMP, the η value is determined as 2.90 eV based on the HOMO and LUMO energies.

Table 1. Global chemical reactivity indices for the 2,4-DMP

Parameters	Values [eV]
E_{HOMO}	-6.27
E_{LUMO}	-0.46
ΔE	5.81
Ionization potential (I)	6.27
Electron affinity (A)	0.46
Electronegativity (χ)	3.37
Chemical potential (μ)	-3.37
Chemical hardness (η)	2.90
Chemical softness (s)	0.17
Electrophilic index (w)	1.96
Maximum load transfer parameter (ΔN_{max})	0.58

eV: electron-volt, E_{HOMO} = highest occupied molecular orbital energy, E_{LUMO} = lowest unoccupied molecular orbital energy, ΔE = energy differences between E_{HOMO} and E_{LUMO} .

3.4. Spectral analysis

Supplementary Table 2 reports the positions of the IR bands, as well as their assignments, measured and computed using the B3LYP/6311++G(d,p) method. The experimental and theoretical FTIR spectra of 2,4-DMP are presented in Figure 4, while the experimental and theoretical UV-Vis. spectra are shown in Figure 5.

In Figure 4, it is seen that the peaks in the spectrum resulting from the theoretical calculation are sharper and separate from each other, while the peaks in the spectrum obtained with the experimental method are less sharp and overlap each other. The reason for this is that the interaction between molecules is prominent in the experimental study and the liquid form of 2,4-DMP is used for analysis, while theoretical calculations are made on a single molecule in gaseous form.

In the experimental spectrum of 2,4-DMP, the broad band at 3358 cm^{-1} is attributed to the O-H band, and this band is observed at 3375 cm^{-1} in the theoretical spectrum. The strong bands observed at 1505 cm^{-1} , 1261 cm^{-1} , 1200 cm^{-1} , and 1115 cm^{-1} in the experimental spectrum of 2,4-DMP. They are attributed to the vibration of C-C, H-C-C, H-O-C, and H-C-C bonds, respectively. These results are supported with the literature [43]. The vibration bands observed at 806 cm^{-1} , 766 cm^{-1} and 717 cm^{-1} in the experimental spectrum are the bands formed by the conjunction of the C atoms in the ring to the methyl group. These bands were calculated at 809 cm^{-1} , 788 cm^{-1} , and 717 cm^{-1} in the theoretical spectrum, respectively.

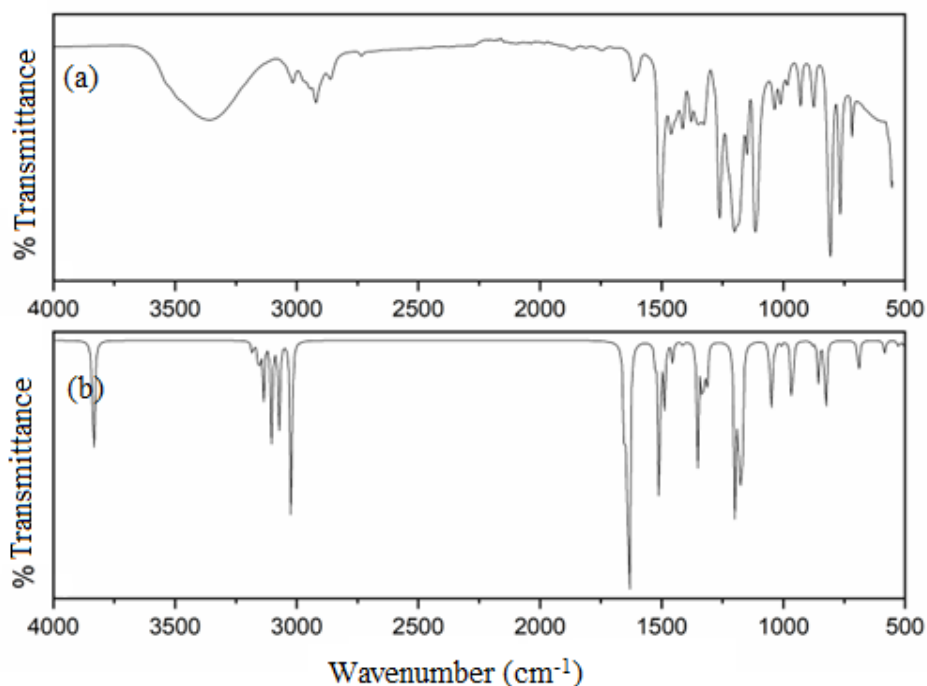


Figure 4. (a) Experimental (b) Theoretical FTIR spectra of 2,4-DMP

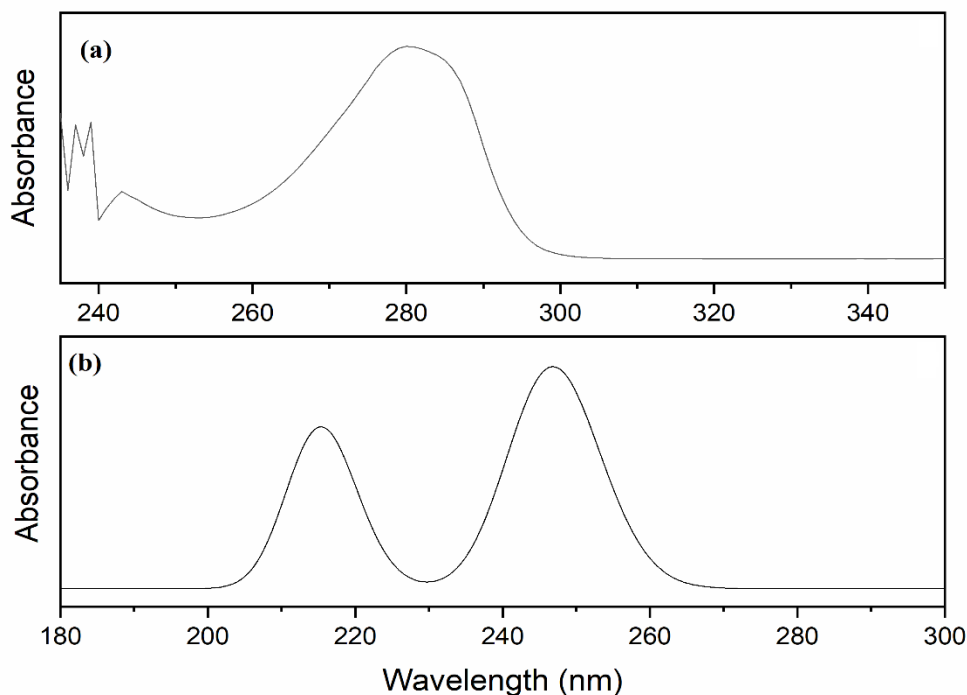


Figure 5. (a) Experimental (b) Theoretical UV-Vis. spectra of 2,4-DMP

The experimental and theoretical UV-Vis. spectra are presented in Figure 5. Due to the presence of a benzene ring, 2,4-DMP exhibits significant absorption in the UV-Vis spectra because of π - π^* transitions. The methyl groups influence the absorption maximum. Upon examining the experimental and theoretical UV-Vis. spectra of the molecule, an absorbance value was observed at 280 nm experimentally and at 255 nm theoretically. The observation of the absorbance value calculated through the theoretical method at a lower wavelength compared to the experimental value can be attributed to the limitations of the chosen computational approach and the possibility that theoretical calculations were conducted under ideal conditions for a single molecule. According to the scientifically validated NIST Chemistry WebBook, 2,4-DMP exhibits a peak at 275 nm in its UV-Vis spectrum [44]. This result is consistent with the findings of this study.

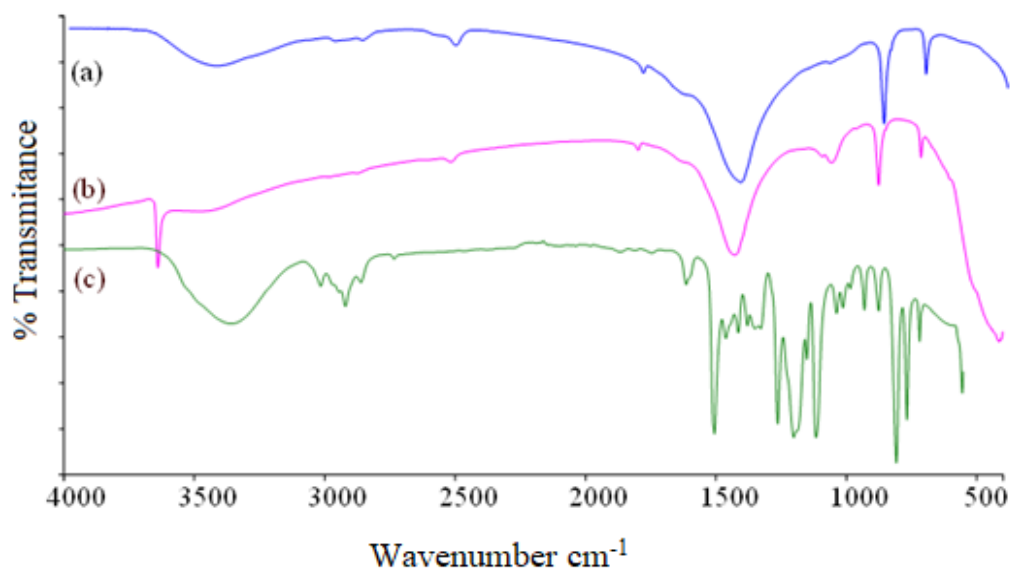


Figure 6. FTIR spectra of (a) pure CCJ, (b) Calcined form of CCJ (C-CCJ) and, (c) pure 2,4-DMP

FTIR spectra of (a) pure CCJ, (b) calcined form of CCJ (C-CCJ) and (c) pure 2,4-DMP are presented in Figure 6. When the FTIR spectra of CCJ and C-CCJ were examined, a deep peak in the fingerprint region between $1500\text{-}1000\text{ cm}^{-1}$ and 2 moderate intensity peaks between $1000\text{-}500\text{ cm}^{-1}$ were observed. These peaks are characteristic vibration bands of eggshell. They were observed in our previous studies [45] and attributed to carbonate peaks; details are available in other studies [30], [46]. In Figure 6c, peaks in the range of $3500\text{-}3000\text{ cm}^{-1}$, which belong to 2,4-DMP, are seen in pure CCJ, also. The peaks in this region belong to OH groups. The C-CCJ form of CCJ after calcination is shown in Figure 6(b). It is observed that water is completely removed from the eggshell calcined at $800\text{ }^{\circ}\text{C}$, but there is a sharp OH peak belonging to the hydroxyl group in Figure 6b.

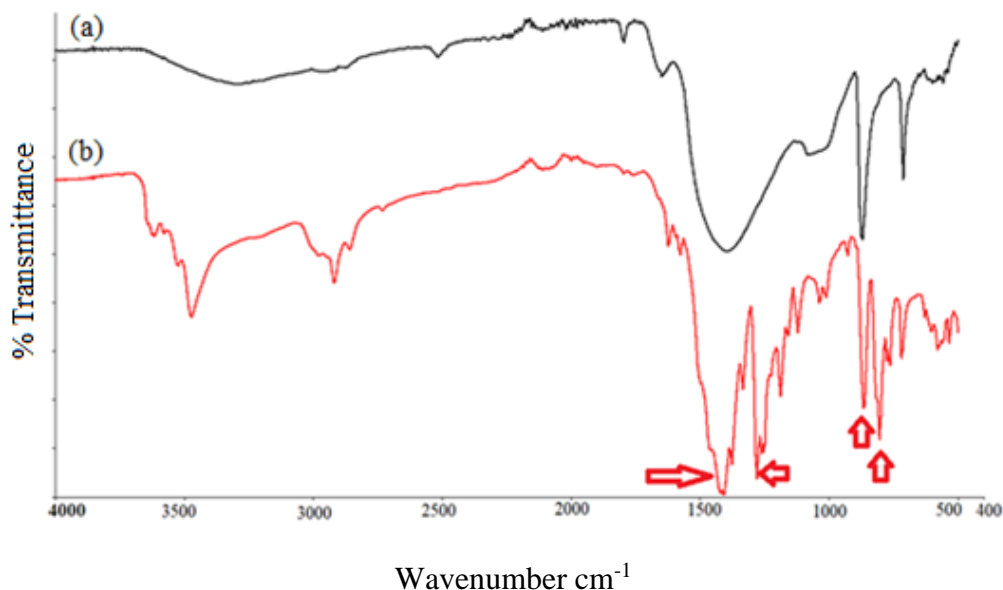


Figure 7. FTIR spectra of (a) 2,4-DMP+CCJ and (b) 2,4-DMP+C-CCJ. Arrows implies the strong peaks.

In Figure 7, it can be seen that the peaks showing adsorption in both CCJ and C-CCJ are in the range of $1600\text{-}500\text{ cm}^{-1}$, which is called the fingerprint region. The strong peaks in this area are marked with arrows. The calcination process enables the vibration bands of 2,4-DMP to be observed more clearly in the range of $4000\text{-}3000\text{ cm}^{-1}$. While no peaks are observed in this region in pure CCJ after adsorption, weak and medium peaks are observed in C-CCJ.

In the characteristic peaks of 2,4-DMP, the H-C-H and C-C-C angle bending peak at 1415 cm^{-1} are seen at 1420 cm^{-1} in C-CCJ after the adsorption process. Unfortunately, in the same region, $\sim 1400\text{ cm}^{-1}$, there is a broad band in the CCJ spectrum. For this reason, this peak, which may belong to adsorption at CCJ, may be hidden. The 2,4-DMP band at 1261 cm^{-1} appeared as a strong peak at 1278 cm^{-1} in the region indicated by the arrow in DMP+C-CCJ. H-C-C-C torsion vibrational mode at 875 cm^{-1} are seen at 864 cm^{-1} for 2,4-DMP+C-CCJ in Figure 7.

3.5. Surface image analysis

AFM and SEM images of the outer surface of CCJ eggshells are presented in Figure 8. Figure 8a depicts the stereo microscope image of the painted CCJ eggshell. Figure 8b shows an area of $5\times 5\text{ }\mu\text{m}$ in AFM image. In this selected area, the distance between the highest and lowest points is approximately 1000 nm . When Figure 8b is examined, the morphological structure of the outer surface of the eggshell consists of bumps. In these bumps, the dark brown color shows the highest points, while the dark blue colors show

the lowest points. It is generally seen as having bubble structure. However, these bubbles do not have a regular size on the selected surface. Some bubbles are very small while others are quite large. The area where light green and yellow colors are mixed resembles the appearance of a valley. Figure 8c is the SEM image of the outer surface of the eggshell. 20Kx magnification was used to obtain this image. It can be seen that it has a bubble structure of different sizes, just like in the AFM image. Two fractures are clearly visible on the SEM image. These fractures are thought to be ventilation channels. Figure 8d is the SEM image of calcined eggshells recorded at 10Kx magnification. It consists of particles stuck together. These particles no longer look like bubbles. The applied calcination process changed the bubbled and regular appearance of the eggshell. Its outer surface appears to have very rough particles. Almost no particle is like another in both appearance and size. When the particulate structure of C-CCJ in the SEM image is evaluated with FTIR results, it is seen that C-CCJ is more suitable for adsorption than pure CCJ. Particles of eggshells are significantly more attractive to remove chemicals than untreated (pure) eggshells. As it was also mentioned before another work [47]. Figure 8 shows that the pore diameters of the CCJ eggshell are of different sizes and the pore distribution is not uniform.

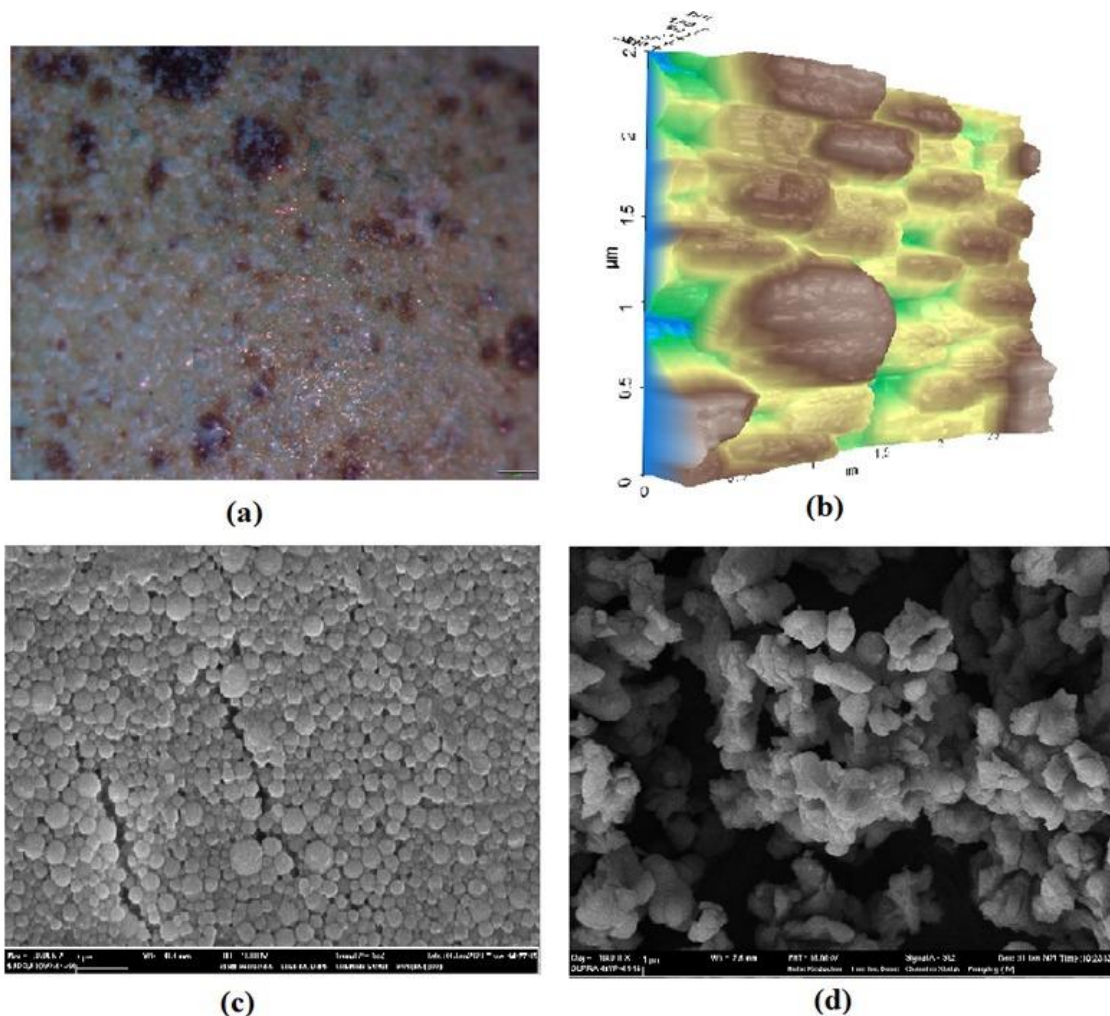


Figure 8. External surface image of CCJ eggshell (a) Stereo microscope (b) AFM (c) SEM and (d) SEM of C-CCJ

4. Conclusion

When looking at the bond lengths and bond angles in the geometry of the 2,4-DMP molecule, the shortest C-H bond length is between C5-H8 (1.0850 Å). The longest C-H bond length of the molecule is seen to be between C14-H16 (1.0951 Å). It is seen that the C2-C3-C4 angle has the largest degree (122.8751°). At the same time, this angle is the largest in the aromatic ring.

In the case of FTIR spectra evaluated, it is observed that water is completely removed from the eggshell calcined at 800 °C, but there is a sharp OH peak in the C-CCJ spectrum belonging to the hydroxyl group. After adsorption process, the 2,4-DMP band at 1328 cm⁻¹ appeared as a strong peak at 1278 cm⁻¹ in the region indicated by the arrow in DMP+C-CCJ. C-C-C-C torsion and H-C-C-C torsion vibrational modes at 875 cm⁻¹ are seen in 872 cm⁻¹ in CCJ and 864 cm⁻¹ in C-CCJ.

Following the adsorption procedure, the C-C stretching and H-C-H angle bending peaks, which are typical peaks of 2,4-DMP, are seen at 1409 cm⁻¹ in C-CCJ. Unfortunately, there is a huge band in the CCJ spectrum in the same area, ~ 1400 cm⁻¹. This may explain why this peak, which might be related to adsorption at CCJ, is concealed. Peaks (in red arrows) in fingerprints region of the spectra assured the adsorption 2,4-DMP on C-CCJ. Adsorption properties can be occurred on surface and/ or inside pores on CCJ. C-CCJ became a powdered form with particles and its particles make attractive sites for adsorption.

The theoretical data show that 2,4-DMP has strong hardness and poor softness qualities due to its wide energy gaps. These imply that the molecule is stable because of its high kinetic stability and low chemical activity. These results force us to explain the adsorption type as physisorption.

When the surface morphology of the CCJ is examined in SEM images, it is seen that both the size and distribution of the pores on the surface are heterogeneous. While the surface morphology is a single plateau in pure CCJ images, the SEM image of C-CCJ has particles. These particles are thought to be responsible for the adsorption of 2,4-DMP onto C-CCJ.

The study showed that 2,4-DMP can be removed from the environment by using CCJ and C-CCJ eggshells. In this study, the porous structure of CCJ and C-CCJ eggshells was proven using surface imaging techniques (light microscope, AFM and SEM). It has been shown that CCJ and C-CCJ eggshells are promising natural materials for the removal of 2,4-DMP from the environment, with their cheap and easily accessible properties they are also biodegradable. Whether they remain in nature or dissolve, they are not hazardous to the environment.

Authorship contribution statement

B. Tunalı: Supervision, Methodology, Instrument Supply, Resource, Conceptualization; **D. Türköz Altuğ:** Investigation, Conceptualization, Resource, Formal Analysis; **T. Kalaycı:** Software, Original Draft Writing, Formal Analysis, Visualization, Project Administration; **N. Kaya Kınaytürk:** Resource, Methodology, Review and Editing, Data Curation.

Declaration of competing interest

The authors declare that they have no known competing financial interests or personal relationships that could have appeared to influence the work reported in this paper.

Acknowledgment

The current study was supported by the Scientific Research Commission of Bandırma Onyedi Eylül University under Research Projects with Foundation Number BAP-22-1003-006 and was supported by the Research Projects with Foundation Number 0118-NAP-10, Burdur Mehmet Akif Ersoy University, Scientific Research Commission, Turkey.

Ethics Committee Approval and/or Informed Consent Information

As the authors of this study, we declare that we do not have any ethics committee approval and/or informed consent statement.

References

- [1] S. I. Mustapha, F. A. Aderibigbe, T. L. Adewoye, I. A. Mohammed, and T. O. Odey, "Silver and titanium oxides for the removal of phenols from pharmaceutical wastewater", *Mater Today Proceeding*, 38, 816–822, 2021.
- [2] Y. Li, H. Liu, L. Zhang, C. Lou, and Y. Wang, "Phenols in soils and agricultural products irrigated with reclaimed water", *Environmental Pollution*, 276, 116690, 2021.
- [3] K. P. Berger, K.R. Kogut, A. Bradman, J. She.Q. Gavin, R.Zahedi, K.L. Perra, K.G. Harley, "Personal care product use as a predictor of urinary concentrations of certain phthalates, parabens, and phenols in the Hermosa study", *Journal of Exposure Science & Environmental Epidemiology*, 29 (1), 21–32, 2019.
- [4] G. W. Holcombe, G. L. Phipps, and J. T. Fiandt, "Effects of phenol, 2,4-Dimethylphenol, 2,4-dichlorophenol, and pentachlorophenol on embryo, larval, and early-juvenile fathead minnows (*Pimephales promelas*)", *Archives of Environmental Contamination and Toxicology*, 11, 73-78 1982.
- [5] I. V. Gruzdev, I. M. Kuzivanov, I. G. Zenkevich, and B. M. Kondratenok, "Determination of methyl-substituted phenols in water by gas chromatography with preliminary iodination", *Journal of Analytical Chemistry*, 68(2), 161–169, 2013.
- [6] J. Miyazaki, N. Furuta, and T. Miyauchi, "Curing of phenol-formaldehyde resin mixed with wood preservatives", *Journal of Applied Polymer Science* 128(5), 2896–2901, 2013.
- [7] F. B. Daniel, M. Robinson, G. R. Olson, R. G. York, and L. W. Condie, "Ten and ninety-day toxicity studies of 2,4-dimethylphenol in Sprague-dawley rats", *Drug Chemical Toxicology*, 16(4), 51–368, 1993.
- [8] O. Onyekwere, C. J. Okonkwo, A. B. Okoroafor, and C. J. Okonkwo, "Occurrence and risk assessment of phenolic endocrine disrupting chemicals in shallow groundwater resource from selected Nigerian rural settlements", *Ovidius University Annals of Chemistry*, 30(2), 101–107, 2019.
- [9] U. States and E. Protection, "EPA Ambient Water Quality Criteria for Cadmium", no. October, US Environmental Protection Agency, 1980.
- [10] A. Romero, A. Santos, and F. Vicente, "Chemical oxidation of 2,4-dimethylphenol in soil by heterogeneous Fenton process", *Journal of Hazardous Materials*, 162(2–3), 785–790, 2009.
- [11] M. Li, X. Wang, C. Lu, R. Li, J. Zhang, S. Dong, L. Yang, L. Xue, J. Chen, and W. Wang., "Nitrated phenols and the phenolic precursors in the atmosphere in urban Jinan, China", *Science of the Total Environment*, 714, 136760, 2020,
- [12] A. Environment, Assessment report on xylenes for developing an ambient air quality objectives, RWDI West Inc,114 pages, 2004.
- [13] P. Raizada, A. Sudhaik, P. Singh, P. Shandilya, V. K. Gupta, A. Hosseini-Bandegharai, and A. Agrawal, "Ag₃PO₄ modified phosphorus and sulphur co-doped graphitic carbon nitride as a direct Z-scheme photocatalyst for 2, 4-dimethyl phenol degradation", *Journal of Photochemistry and Photobiology A Chemistry*, 374, 22–35, 2019.
- [14] J. P. Ghosh, K. E. Taylor, J. K. Bewtra, and N. Biswas, "Laccase-catalyzed removal of 2,4-dimethylphenol from synthetic wastewater: Effect of polyethylene glycol and dissolved oxygen", *Chemosphere*, 71(9), 1709–1717, 2008.

- [15] M. Al-Obaidi, B. Al-Nedawe, A. Mohammad, and I. Mujtaba, "Response surface methodology for predicting the dimethylphenol removal from wastewater via reverse osmosis process", *Chemical Product and Process Modeling*, 16(3), 193–203, 2021.
- [16] Canadian Water Quality Guidelines for the Protection of Aquatic Life, [Online]. Available: <https://ccme.ca/en/res/phenols-en-canadian-water-quality-guidelines-for-the-protection-of-aquatic-life.pdf>, Accessed:1999
- [17] K. Sharma, P. Raizada, A. Hosseini-Bandegharaei, P. Thakur, R. Kumar, V.K. Thakur, V. Nguyen, P. Singh, "Fabrication of efficient CuO / graphitic carbon nitride based heterogeneous photo-Fenton like catalyst for degradation of 2, 4 dimethyl phenol", *Process Safety and Environmental Protection*, 142, 63–75, 2020.
- [18] M. Trapido, Y. Veressinina, and R. Munter, "Advanced oxidation processes for degradation of 2,4-Dichlo- and 2,4-Dimethylphenol", *Journal of Environmental Engineering*, 124(8), 690–694, 1998.
- [19] F. Vicente, J. M. Rosas, A. Santos, and A. Romero, "Improvement soil remediation by using stabilizers and chelating agents in a Fenton-like process", *Chemical Engineering Journal*, 172(2–3), 689–697, 2011.
- [20] L. Rucká, J. Nešvera, and M. Pátek, "Biodegradation of phenol and its derivatives by engineered bacteria: current knowledge and perspectives", *World Journal of Microbiology and Biotechnology*, 33(9), 1–8, 2017.
- [21] C. Stratton and J. Stokes, "Multidisciplinary Remediation: An Analysis of Chlorinated Metabolites in Groundwater Contaminated by Pentachlorophenol Following 15 Years of Air/Biosparging, Phytoremediation, and In-Situ Chemical Oxidation Protocols", *Mississippi Water Resources Conference*, 31–37, 2016.
- [22] M. Waheed *et al.*, "Eggshell calcium: A cheap alternative to expensive supplements", *Trends in Food Science Technology*, 9, 1219–230, 2019.
- [23] M. Gaonkar, A. P. Chakraborty, and A. Professor, "Application of eggshell as fertilizer and calcium supplement tablet", *International Journal of Innovative Research in Science, Engineering and Technology*, 3297, 2007.
- [24] A. Schaafsma, J. J. van Doormaal, F. A. J. Muskiet, G. J. H. Hofstede, I. Pakan, and E. van der Veer, "Positive effects of a chicken eggshell powder-enriched vitamin–mineral supplement on femoral neck bone mineral density in healthy late post-menopausal Dutch women", *British Journal of Nutrition*, 87(3), 267–275, 2002
- [25] I. M. Muhammad, U. a El-Nafaty, S. Abdulsalam, and Y. I. Makarfi, "Removal of Oil from Oil Produced Water Using Eggshell", *Civil and Environmental Research*, 2(8), 52–64, 2012.
- [26] A. H. Jendia, S. Hamzah, A. A. Abuhabib, and N. M. El-Ashgar, "Removal of nitrate from groundwater by eggshell biowaste", *Water Science Technology: Water Supply*, 20(7), 2514–2529, 2020.
- [27] A. Rahmani-Sani, P.Sing, P. Raizada, E.C. Lima, I. Anastopoulos, D. A. Giannakoudakis, S. Sivamani, T.A. Dontsova, and A. Hosseini-Bandegharaei, "Use of chicken feather and eggshell to synthesize a novel magnetized activated carbon for sorption of heavy metal ions", *Bioresour Technol*, 297, 122452, 2020.
- [28] T. Y. Lin, W. S. Chai, S.J. Chen, J. Y. Shih, A. K. Koyande, B.L. Liu, and Y.K. Chang "Removal of soluble microbial products and dyes using heavy metal wastes decorated on eggshell", *Chemosphere*, 270, 128615, 2021.
- [29] A. Laca, A. Laca, and M. Díaz, "Eggshell waste as catalyst: A review", *Journal of Environmental Management*, 197, 351–359, 2017.
- [30] N. K. Kinaytürk, B. Tunali, and D. Türköz Altuğ, "Eggshell as a biomaterial can have a sorption capability on its surface: A spectroscopic research", *Royal Society Open Science*, 8(6), 2021.
- [31] J. A. P. M.J. Frisch, G.W. Trucks, H.B. Schlegel, G.E. Suzerain, M.A. Robb, J.R. Cheeseman Jr., J.A. Montgomery, T. Vreven, K.N. Kudin, J.C. Bu-rant, J.M. Millam, S.S. Iyengar, J. Tomasi, V. Barone, B. Mennucci, M. Cossi, G. Scalmani, N. Rega, G.A. Petersson, and H. Nakat, "Gaussian 09", 2003.
- [32] P. Pulay, G. Fogarasi, G. Pongor, J. E. Boggs, and A. Vargha, "Combination of theoretical ab initio and experimental information to obtain reliable harmonic force constants. Scaled quantum mechanical (sqm) force fields for glyoxal, acrolein, butadiene, formaldehyde, and ethylene", *Journal of American Chemical Society*, 105(24), 7037–7047, 1983.
- [33] T. Sundius, "Molvib-A flexible program for force field calculations", *Journal of Molecular Structure*, 218, 321-326, 1990.
- [34] T. Sundius, "Scaling of ab initio force fields by MOLVIB", *Vibrational Spectroscopy*, 29, 89-95, 2002.
- [35] R. El Mouhi, O. Daoui, A. Fitri, A. T. Benjelloun, S. Khattabi, M. Benzakour, M. Mcharfi, and M. Kurban, "A strategy to enhance VOC of π -conjugated molecules based on thieno[2,3-b] indole for applications in bulk heterojunction organic solar cells using DFT, TD-DFT, and 3D-QSPR modeling studies", *New Journal of Chemistry*, 47(2), 812–827, 2022.

- [36] R. El Mouhi, A. Slimi, A. Fitri, A. T. Benjelloun, S. ElKhattabi, M. Benzakour, M. Mcharfi, and M. Kurban, "DFT, DFTB and TD-DFT theoretical investigations of π -conjugated molecules based on thieno[2,3-b] indole for dye-sensitized solar cell applications", *Physica B Condensed Matter*, 636, 413850, 2022.
- [37] P. Divya and V. Bena Jothy, "Density functional theoretical analysis with experimental, invitro bioactivity and molecular docking investigations on the pesticide Albendazole", *Chemical Physics Letter*, 695, 1–7, 2018.
- [38] P. J. A. Madeira, P. J. Costa, M. T. Fernandez, J. A. M. Simões, and J. P. Leal, "Determination of Gas-Phase Acidities of Dimethylphenols: Combined experimental and theoretical study", *Journal of American Society Mass Spectrometry*, 19(11), 1590–1599, 2008
- [39] T. Kalaycı, N. K. Kınaytürk, and B. Tunalı, "Experimental and theoretical investigations (Ftir, Uv-Vis Spectroscopy, Homo-Lumo, Nlo and Mep analysis) of Aminothiophenol Isomers", *Bullutein Chemical Society Ethiopia*, 35(3), 2021.
- [40] S. Celik, G. Yilmaz, S. Akyuz, and A. E. Ozel, "Shedding light into the biological activity of aminopterin, via molecular structural, docking, and molecular dynamics analyses", *Journal of Biomolecular Structure Dynamics*, 1-22, 2023.
- [41] N. K. Kınaytürk, T. Kalaycı, B. Tunalı, and D. Türköz Altuğ, "A Spectroscopic Approach to Compare the Quantum Chemical Calculations and Experimental Characteristics of Some Organic Molecules; Benzene, Toluene, P-Xylene, P-Toluidine", *Chemical Physics*, 570, 111905, 2022.
- [42] N. Kaya Kınaytürk, T. Kalaycı, and B. Tunalı, "Experimental and computational investigations on the molecular structure, vibrational spectra, electronic properties, and molecular electrostatic potential analysis of phenylenediamine isomers", *Spectroscopy Letters*, 54(9), 93–706, 2021.
- [43] X. Zhou, Q. Zhou, H. Chen, J. Wang, Z. Liu, and R. Zheng, "Influence of dimethylphenol isomers on electrochemical degradation: Kinetics, intermediates, and DFT calculation", *Science of the Total Environment*, 794, 2021.
- [44] "Phenol,2,4-dimethyl", 2023.[Online].Available: <https://webbook.nst.gov/cgi/cbook.cg?ID=105-67-9>.
- [45] T. Kalaycı, D. Türköz Altuğ, N. Kaya Kınaytürk, and B. Tunalı, "Quantum chemical calculations of m-toluidine and investigation of its adsorption on eggshells", *Erzincan Üniversitesi Fen Bilimleri Enstitüsü Dergisi*, 16(1), 169–183, 2023.
- [46] B. Tunalı, D. Türköz Altuğ, N. Kaya Kınaytürk, and G. Tüzün, "Removal of heavy metals (copper and lead) using waste eggshell with two different species and three different forms", *Mehmet Akif Ersoy Üniversitesi Fen Bilimleri Enstitüsü Dergisi*, 12(1), 434–445, 2021.
- [47] S. G. Mohammad, S. M. Ahmed, and M. M. H. El-Sayed, "Removal of copper (II) ions by eco-friendly raw eggshells and nano-sized eggshells: A comparative study", *Chemical Engineering Communications*, 209(1), 83–95, 2022.

*Supplementary Material***Table S1.** Bond lengths and bond angles for 2,4-DMP

2,4-DMP					
Atoms	Bond length (Å)	Atoms	Bond Angles (°)	Atoms	Bond Angles (°)
C1-C2	1.4046	C2-C1-C6	120.5474	C2-C10-H12	111.1916
C1-C6	1.3910	C2-C1-O18	116.8836	C2-C10-H13	110.9211
C1-O18	1.3719	C6-C1-O18	122.5689	H11-C10-H12	106.5044
C2-C3	1.3922	O1-C2-C3	117.7989	H11-C10-H13	108.4363
C2-C10	1.5061	O1-C2-C10	119.9197	H12-C10-H13	108.4366
C3-C4	1.4013	C3-C2-C10	122.2814	C4-C14-H15	111.4706
C3-H7	1.0867	C2-C3-C4	122.8751	C4-C14-H16	111.4538
C4-H5	1.3930	C2-C3-H7	118.1537	C4-C14-H17	111.2448
C4-C14	1.5106	C4-C3-H7	119.9930	C15-C14-H16	107.1750
C5-C6	1.3947	C3-C4-C5	117.7287	H15-C14-H17	107.7049
C5-H8	1.0850	C3-C4-C14	120.7002	H16-C14-H17	107.5798
C6-H9	1.0868	C5-C4-C14	121.5702	C1-O18-H19	108.9943
C10-H11	1.0941	C4-C5-C6	120.8748		
C10-H12	1.0941	C4-C5-H8	119.8790		
C10-H13	1.0915	C6-C5-H8	119.2462		
C14-H15	1.0944	C1-C6-C5	120.175		
C14-H16	1.0951	C1-C6-H9	119.7726		
C14-H17	1.0921	C5-C6-H9	120.0523		
O18-H19	0.9624	C2-C10-H11	111.1890		

Table S2. Assignments of experimental and theoretical wavenumbers (cm^{-1}) of pure 2,4-DMP, 2,4-DMP adsorbed on CCJ and 2,4-DMP adsorbed on C-CCJ eggshells.

2,4-DMP	Theoretic al (Scaled)	Exp. IR	Assignment (%PED)	2,4-DMP+ CCJ	2,4-DMP+ C-CCJ
					3615 vw
3835	3375	3358 br	ν_{OH} (100)	3291 br	3472 m
3181	3022	3017 w	ν_{CH} (98)		
3156	2998		ν_{CH} (94)		
3136	2979	2972	ν_{CH} (97)	2973 w	2979 w
3104	2949		ν_{CH} (85)		
3103	2948	2947 w	ν_{CH} (83)		2946 w
3074	2920	2922 w	ν_{CH} (91)		2918 m
3071	2918		ν_{CH} (97)		
3023	2872	2861 vw	ν_{CH} (90)		2856 w
1653	1620	1614 m	ν_{CC} (52)+ δ_{HCC} (10)+ δ_{CCC} (11)	1620 w	1619 w
1635	1504	1505 vs	ν_{CC} (44)+ δ_{CCC} (32)+ δ_{HCC} (18)		1500 sh
1527	1497		δ_{HCH} (10)+ δ_{HCC} (14)+ τ_{HCCC} (10)+ ν_{CC} (26)		
1510	1479		δ_{HCH} (51)+ + τ_{HCCC} (14)		
1491	1461	1461 m	τ_{HCCC} (12)+ δ_{HCH} (65)		1460 sh
1487	1457		δ_{HCH} (65)+ τ_{HCCC} (20)		
1455	1426	1415 m	δ_{HCH} (73)+ δ_{CCC} (20)	1400 vs	1420 vs
1416	1388		δ_{HCH} (90)		1409 vs
1413	1385	1378 m	δ_{HCH} (93)		1373 w
1352	1325	1328 vw	ν_{CC} (43)		1335 w
1332	1305		δ_{HCC} (12)+ δ_{CCC} (10)+ ν_{OC} (17)+ ν_{CC} (46)		
1315	1288	1261 vs	δ_{HCC} (54)+ δ_{HOC} (17)		1278 s
1198	1174	1200 vs	δ_{HOC} (66)+ ν_{CC} (21)		1250 w
1183	1159	1150 m	δ_{HCC} (48)+ ν_{CC} (17)		1160 w
1172	1149	1115 vs	δ_{HCC} (52)+ ν_{OC} (16)	1081 w	1119 m
1059	1039		τ_{HCCC} (56)+ δ_{HCH} (11)		
1057	1036	1035 m	τ_{HCCC} (50)+ δ_{HCH} (16)		1036 w
1047	1026	1012 m	τ_{HCCC} (35)+ ν_{OC} (12)		1009 w
1034	1013		τ_{HCCC} (47)		
1009	989	982 w	δ_{CCC} (44)+ ν_{OC} (38)		
966	947	930 s	ν_{CC} (26)+ τ_{HCCC} (13)+ δ_{CCC} (11)		926 w
960	883	875 s	ν_{CC} (28)+ τ_{HCCC} (15)	870 vs	864 s
880	809	806 vs	τ_{HCCC} (80)		811 sh
856	788	766 vs	τ_{HCCC} (83)		777 m
827	761	717 m	τ_{HCCC} (62)	712 s	716 m
691	635		τ_{CCCC} (73)+ τ_{HCCC} (14)	601 w	577 w
584	572		τ_{OCCC} (13)+ δ_{HCC} (15)+ ν_{CC} (51)		
580	568	553 s	τ_{CCCC} (13)+ τ_{OCCC} (39)+ τ_{HCCC} (11)	557 w	560 vw

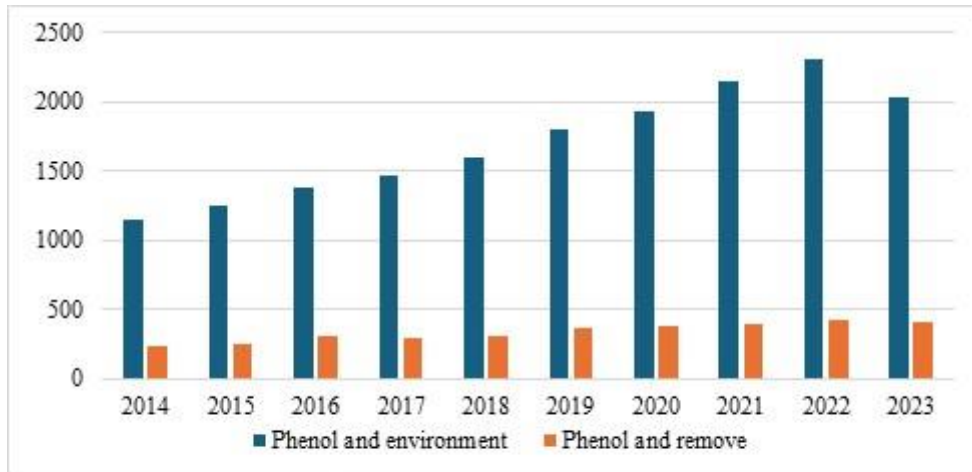


Figure S1. Numerical data of the search made with the words "Phenol and environment" and "Phenol and remove" in WOS between 2014 and 2023.

Cytogenetic and Morphophysiological Effects of Exogenous Triacantanol against Drought in Barley

Selma Tabur^{1,*}, Serkan Özmen¹, Ahmet Yiğit¹

¹Department of Biology, Faculty of Engineering and Natural Sciences, Suleyman Demirel University, 32100, Isparta, TÜRKİYE

<https://orcid.org/0000-0001-9458-944X>

*corresponding author: taburs@gmail.com

¹Department of Biology, Faculty of Engineering and Natural Sciences, Suleyman Demirel University, 32100, Isparta, TÜRKİYE

<https://orcid.org/0000-0003-4376-5866>

¹Department of Biology, Faculty of Engineering and Natural Sciences, Suleyman Demirel University, 32100, Isparta, TÜRKİYE

<https://orcid.org/0000-0001-5406-9044>

(Received: 07.08.2024, Accepted: 25.10.2024, Published: 25.11.2024)

Abstract: Drought stress is one of the leading abiotic stresses that have a devastating impact on sustainable agricultural policy as a result of the decrease in crop yield. For this reason, hormones or growth regulators can be used to grow plants that can adapt to morphological and physiological changes caused by stress. Triacantanol (TRIA) is a hormone that takes part in abiotic stress tolerance mechanisms and performs this task by ensuring the continuity of growth, productivity, development and vital metabolic processes. In this study, the morphophysiological and cytogenetic effects of exogenous TRIA application in barley (*Hordeum vulgare* cv. Avcı) under drought stress were investigated. The results showed that drought stress negatively affected barley both morphophysiological and cytogenetically. Application of exogenous TRIA had an increasing effect on germination percentage, radicle number, coleoptile length and percentage under drought stress. Moreover, in the same environment, with the effect of TRIA, there was an increase in the mitotic index (44%) and a decrease in chromosomal abnormalities (46%). The conclusion drawn from this study is that the application of 10 µM TRIA application causes physiological and cytogenetic improvements in barley under drought stress, resulting in the plant's stress tolerance.

Key words: Drought, Mitotic activity, Morphophysiological effects, TRIA.

1. Introduction

One of the biggest risks to plant growth is drought stress, which is caused by increasing temperatures due to climate change around the world, decreasing precipitation, and using the wrong tactics such as inconsistent irrigation. Crop development and productivity are severely harmed by drought stress because it lowers the quality of the morphological, physiological, and biochemical features of plants [1]. According to research conducted in a variety of countries, the drop in yearly precipitation produced by global warming has had a deleterious impact on plants, including a fall in relative water content and loss of turgor [2]. Drought also interferes with growth, photosynthesis, and other vital physiological and biochemical functions [3]. Previous studies has demonstrated that the stress caused by drought increases chromosomal aberrations, decreases the cell cycle and mitotic index, damages biological membranes and macromolecules, and generates oxidative stress [4-7].

Adverse environmental conditions such as drought threaten the survival of plants that depend on soil and inhibits plant growth, development, and product quality [8]. Numerous plant investigations have demonstrated the detrimental consequences of drought stress at the physiological [9–12] and cytogenetic levels [6, 13, 14]. However, plants produce a range of organic substances, including plant hormones, that aid in their adaptation in response to these changes through a variety of biochemical, molecular, and structural alterations [15].

Plant hormones are a class of signaling molecules that are present in minute quantities in cells. They are crucial for regulating metabolism in response to biotic and abiotic stresses and for improving a plant's capacity to morphologically and physiologically adapt to unfavorable environmental circumstances [16]. Although prior research has established the roles of certain hormones, including gibberellin, ethylene, auxins, ABA, and salicylic acid, in abiotic stress tolerance, it is recognized that the mechanisms of action of these hormones vary depending on the degree of stress, the type of plant, and the tissues that are under stress [17–19]. TRIA is a plant growth regulator that helps plants adapt to harsh environments like salt and drought by balancing a variety of physiological and biochemical processes. After exogenous application of TRIA, which is in the form of a 30-carbon primary alcohol, the increase in photosynthesis, water and nutrient assimilation, membrane stability, gene regulation and activities in vital processes has attracted the attention of researchers [20]. TRIA, which is present in plant epicuticular waxes, increases nitrogen fixation when applied exogenously to plants. In addition, it raises the levels of photochemical pigments, sugars, soluble proteins, free amino acids, carbonic anhydrase, transpiration rate, photosynthetic rate, and water usage efficiency [21]. The exogenous injection of TRIA boosts growth, dry mass, photosynthetic pigments, photosynthesis rate, suitable osmolytes, and antioxidant enzyme activities, hence mitigating the harmful effects on plants under abiotic stress conditions. This is because TRIA actively regulates the processes of plants in changing environmental conditions [22–24].

Aim of the work was designed to comprehensively test of the efficiency level of exogenous TRIA against effects physiological, cytotoxic and genotoxic in caused by drought stress in *Hordeum vulgare* cv. *Avc1* meristem cells and to contribute to the gap in the literature. That is, it is aimed at clarifying to what extent exogenous TRIA tolerates drought stress, whether it encourages cells to enter the mitosis division, and whether it causes any changes in the structure and behavior of chromosomes.

2. Material and Method

Hordeum vulgare cv. *Avc1* seedlings were obtained from Ankara Field Crops Central Research Institute and employed in the study's experimental phases. In addition, PEG 6000, among the chemicals used to reveal the effect of drought stress in plants, was supplied by Merck Firm (S7455691, 1 kg) and the TRIA Fluka Firm (90275, 100 mg) was supplied. To generate a 500 ml stock with a 100 μ M concentration for the investigation, the TRIA was dissolved in distilled water and kept at +4 °C in the refrigerator. In a preliminary investigations conducted by us, the most proper concentration of TRIA in alleviation of the drought stress at the germination were determined as 10 μ M and also 22% PEG 6000 was the most suitable concentration for drought stress. 22% PEG 6000 concentration was prepared fresh each use by dissolving it in distilled water.

2.1. Identification of physiological properties

Every germination experiment involving the barley seeds utilized in the study was conducted in a dark, sterile incubator with a temperature setting of 20 °C. During the first phase of the germination trials, seeds that appeared physically alive, plumpness, and similar characteristics were chosen. Prior to use, these chosen seeds were surface sterilized by washing them with distilled water for 24 hours and pre-treated in 1% sodium hypochlorite for 10 minutes. The sterilized seeds were placed in conical flasks with 50 ml of distilled water and 10 µM TRIA, and they were soaked for a full day at room temperature. Following that, these seeds were placed in 10 cm sterile, disposable petri plates that were double-layered with blotting paper on the bottom and contained 7 ml of distilled water and 22% PEG 6000. The germination percentage, fresh weight, radicle numbers and lengths, coleoptile percentage, and lengths of the seedlings sprouting from the germinated seeds were measured after the planted petri dishes were maintained in the incubator for seven days. The length of the radicle was measured by using a ruler to measure the portion of the germinated seeds from the point where the root and stem separated to the tip of the longest fringe root. By using a ruler to measure the length of each germinating seed, from the point where the root and coleoptile separate to the tip of these organs, the coleoptile length was ascertained. The number of radicles and the percentage of coleoptiles in the seedlings were determined by counting the germinated roots and coleoptiles based on their concentrations at the end of the seventh day in the incubator. A precision scale was used to weigh all of the germinated seeds after they had sprouted for seven days. The average fresh weight, given in grams per plant, was then calculated by dividing the weight by the total number of seeds that germinated [25].

2.2. Identification of cytogenetic characteristics

The root tips of seeds belonging all concentrations in the research after they reached 0.5–1 cm in length, the roots were chopped and placed in glass bottles containing pretreatment solution. Then, the root tips pretreated for 4 h. at paradichlorobenzene. Following a distilled water wash, root tips extracted from the paradichlorobenzene solution were kept in acetic alcohol (3 parts ethyl alcohol/1part glacial acetic acid) solution at +4 °C for a full day. After being taken out of the acetic alcohol, the root tips were placed in 70% alcohol solutions and refrigerated at +4 °C until the cytogenetic procedures were carried out [26].

2.3. Root tip staining procedures and preparation

After the root tips, which had been kept at +4 °C and 70% alcohol, had been washed several times with tap water were kept in 5 N HCl at room temperature for 20-25 minutes for hydrolysis. Hydrolyzed root tips were stained with Feulgen at room temperature for 1h. The root tips were then let to sit in little petri dishes filled with water for 15 min. to remove any leftover dye. Finally, after the dying process, the slayts were prepared by the crushing method for the preparation process and examinations were made [26].

2.4. Calculating chromosomal aberrations and mitotic index

The 100X magnification of the microscope was used to scan the slides prepared for the purpose of examining the stages of mitosis. Three iterations of counting the prepared slides were performed. After counting at least 3000 cells for each application (3x1000), mitotic index, phase indices and chromosomal abnormalities were calculated using the following equations. Images of chromosomal anomalies were photographed (100X) using a C-5060 WZ digital camera and an Olympus CX41 research microscope.

$$\text{Mitotic index (\%)} = \frac{\text{Number of cells in mitosis}}{\text{Total number of cells}} \times 100$$

$$\text{Chromosome aberrations (\%)} = \frac{\text{Number of abnormal cells}}{\text{Number of cells in mitosis}} \times 100$$

$$\text{Phase indices} = \frac{\text{Number of cells belonging to phase}}{\text{Total number of dividing cells}} \quad [27,28].$$

3. Results and Discussions

In this study, the physiological characteristics and cytogenetic effects of exogenous TRIA application in barley under normal and drought conditions were investigated and the results were compared. According to the results obtained, the scores of physiological changes in control and PEG 6000 applied seeds is presented in Table 1. The germination percentage value of barley seeds planted in petri dishes in distilled water (control group) environment after seven days was 79.00 ± 5.03 . However, with TRIA application alone to stress-free environment reached value of 92% increasing in the germination percentage by approximately 16% compared to the control group. This increase, in addition to being numerical, also revealed a statistically significant different. Drought stress showed its negative effect by decreasing from 79.00 ± 5.03 to 42.00 ± 4.00 (approx. 47%) the germination percentage compared to the control group. Exogenously applied TRIA were ameliorated the negative effect caused by drought on germination percentage, achieving value almost close to the stress-free environment. Drought+TRIA application compared to alone drought on the germination percentage was showed an increase of 70% and the germination percentage value was 72.00 ± 7.30 . As a result of the study, it was determined that the fresh weight of barley seeds germinated in distilled water environment was 257.00 ± 5.72 mg. TRIA administered alone showed an inhibitory effect of approximately 5% on fresh weight. After the application of drought stress, fresh weight down to 111.00 ± 2.16 mg by decreasing approximately 60% compared to the control group. After Drought+TRIA applied, there was a decrease in the amount of fresh weight compared to the control group, as in the non-stress environment. It was observed that the root length values in the control group were both statistically and numerically close to each other when TRIA was applied alone in a non-stressed environment. Accordingly, while the radicle length in the control group was 10.00 ± 2.21 cm, it was 10.93 ± 1.81 cm after TRIA application. However, drought stress and TRIA application values under stress also showed very close values to each other. After applying drought stress alone, radicle length decreased to 4.89 ± 1.52 cm, a 52% decrease compared to the control group. Likewise, after TRIA applied in a stressful environment, radicle length decreased to 4.22 ± 1.27 cm.

In the study conducted to determine the number of radicles in barley seeds, this value was determined to be 4.75 ± 0.59 in the control group. After the addition of TRIA, the number of radicles increased by approximately 5% and reached 4.99 ± 0.72 . As expected, the number of radicles decreased after drought stress. As a results of the study, the number of radicles decreased by approximately 30% under stress, with a value of 3.34 ± 0.76 . After exogenous TRIA application in the presence of drought stress, the number of radicles increased slightly, up to 3.40 ± 0.91 . When the coleoptile percentage values were examined in the study, it was determined that the results obtained after the control group and TRIA application were very close to each other. According to the results obtained, the coleoptile percentage values in the control group and after TRIA application were determined to be 98.69% and 100%, respectively. Application of drought stress caused the coleoptile percentage in barley plants to decrease by approximately 32%, down to 68% compared to the control group. However, TRIA applied in the presence of stress showed a stimulating effect on this parameter. According to the results obtained, the coleoptile

percentage increased by approximately 25% compared to the control group and rose to 83.80%. When the results obtained were examined, it was determined that the results of coleoptile lengths were parallel to the results of coleoptile percentage. Accordingly, the coleoptile length values in the control group and after TRIA application were 10.13 ± 1.99 and 10.21 ± 1.84 cm. Drought stress had a negative effect on this parameter, as in all other parameters. Application of drought stress caused the coleoptile length to decrease by 82% to 1.92 ± 1.32 cm. TRIA applied under drought stress showed an encouraging effect on coleoptile length by increasing the coleoptile length (approx. 12%) and reached 2.18 ± 1.31 cm (Table 1).

Table 1. Effects of exogenous TRIA on physiological changes in barley under drought stress and normal conditions (*Shows values with insignificant difference ($p < 0.05$) for each column shown with same letters, \pm standard deviation).

Applications	Germination percentage (%)	Fresh weight (mg)	Radicle length (cm)	Number of radicles	Coleoptile percentage (%)	Coleoptile length (cm)
Control	*79.00 \pm 5.03 ^b	257.00 \pm 5.72 ^c	10.00 \pm 2.21 ^b	4.75 \pm 0.59 ^{ab}	98.69 \pm 2.63 ^c	10.13 \pm 1.99 ^b
10 μ M TRIA	92.00 \pm 5.66 ^c	248.00 \pm 9.09 ^b	10.93 \pm 1.81 ^b	4.99 \pm 0.72 ^b	100.00 \pm 0.00 ^c	10.21 \pm 1.84 ^b
%22 PEG 6000	42.00 \pm 4.00 ^a	111.00 \pm 2.16 ^a	4.89 \pm 1.52 ^a	3.34 \pm 0.76 ^a	68.00 \pm 2.37 ^a	1.92 \pm 1.32 ^a
%22 PEG 6000 +10 μ M TRIA	72.00 \pm 7.30 ^b	108.00 \pm 2.94 ^a	4.22 \pm 1.27 ^a	3.40 \pm 0.91 ^a	83.80 \pm 11.10 ^b	2.18 \pm 1.31 ^a

Under normal conditions, where there are no biotic or abiotic stresses, there is no need to use additional external hormones or growth regulators for the seeds to germinate. In the absence of any stress conditions, growth regulators given externally to plants have positive effects on seed germination and seedling growth but may also have negative effects. According to the findings obtained in this study, it was determined that drought stress had an inhibitory effect on all physiological parameters. There are many studies showing that there is a decrease in germination percentage, fresh weight, root number, root length, coleoptile length and percentage as a result of applying drought stress [29–32]. In order to alleviate or eliminate such negative effects of drought stress, researchers have applied TRIA exogenously to various plants and at different drought stress intensities and shared the results. In one of these studies, 30% TRIA application to *Triticum aestivum* L. seedlings resulted in physiological developments due to increased seed germination, seedling growth, and free amino acid accumulation after PEG-based drought stress application [33]. In another study, it was reported that TRIA application in *Vigna unguiculata* (L.) seeds under drought stress improved the stress tolerance of the plant by improving germination parameters such as germination ability, relative seed germination, germination rate, radical and hypocotyl length, total seedling length and growth [34]. Sanadhya et al. [35] stated that TRIA pre-application to mung bean seeds significantly increased root and shoot length, germination percentage, fresh and dry weight of seedlings, thus increasing tolerance to PEG-induced drought stress. In another study conducted on rice plant, it was stated that TRIA application created a defense mechanism against drought stress by improving seed germination, seedling length, fresh mass, dry mass and biochemical enzyme activities [36]. After detailed literature research, no study was found investigating the effects of exogenous TRIA application on morphophysiological characteristics of especially barley plants under drought stress conditions. Therefore, the effects of TRIA application on the germination percentage,

fresh weight, number of radicles, radicle length, coleoptile length and coleoptile percentage in barley plants under drought and normal conditions are presented for the first time in this study. As can be seen from the results, drought stress caused negative effects on all parameters, causing a decrease in the values. Additionally, it is clearly seen that exogenous application of TRIA together with drought stress also creates a response mechanism to drought stress. It has been concluded that the increase in germination percentage, radicle length, radicle number, coleoptile percentage and length values caused by TRIA application has significant effects on coping with drought stress, especially in barley plant and other plants that can be used.

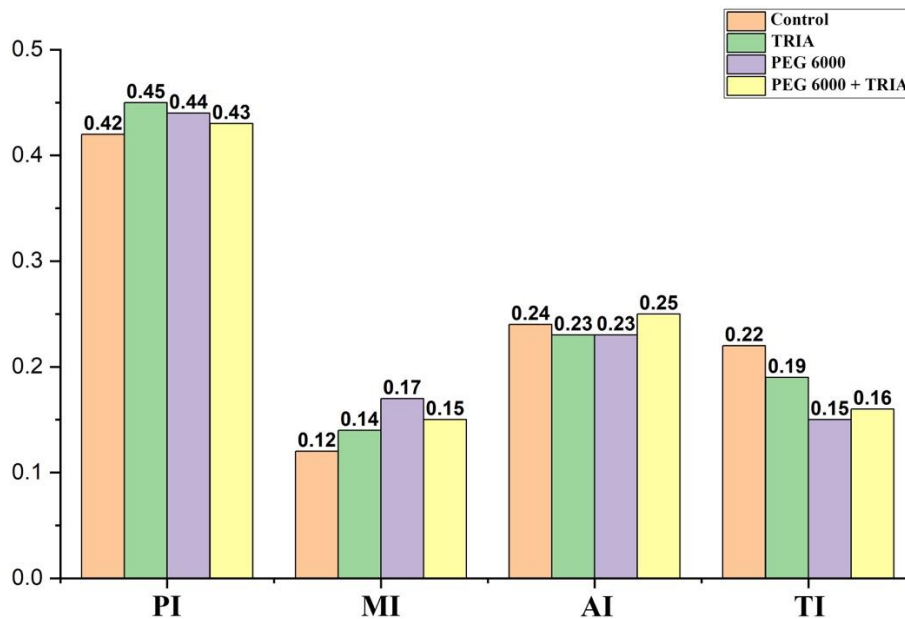


Figure 1. Effects of exogenous TRIA on mitotic division stages in barley under both drought and normal conditions (PI: Prophase index, MI: Metaphase index, AI: Anaphase index, TI: Telophase index)

Mitotic index and chromosome abnormality values according to the data obtained in this study are shown in Table 2. The mitotic index value was determined to be $10.20 \pm 0.76\%$ in the control group germinated in distilled water environment. With the application of drought stress to the control group, TRIA applied in both normal and drought environments revealed statistically and numerically significant differences. TRIA application alone increased the mitotic index value by approximately 8% ($11.04 \pm 0.21\%$) compared to the control group. The lowest mitotic index value was observed after the application of drought stress. That is, drought stress was an inhibitory effect by reducing the mitotic index value by 20% ($8.18 \pm 0.61\%$). With Drought stress+TRIA application, the mitotic index was the highest value reached. The findings revealed that TRIA applied under stress had a stimulating effect by increasing the mitotic index value by approximately 44% ($11.85 \pm 0.12\%$) compared to alone drought stress conditions.

Following the determination of the mitotic index, the indices at each stage of mitosis were determined by taking into account the dividing cells of all concentrations (Figure 2). While the concentration with the highest index in prophase, which is the first phase of mitosis, was the TRIA application alone, the concentration with the lowest index was seen in the control group. When the metaphase indices were examined, the concentration with the highest index was the drought stress application, while the concentration with the lowest phase index was the control group. At anaphase indexes, Drought stress+TRIA application had the highest phase index compared to all other concentrations, while TRIA and drought stress applications alone showed the lowest anaphase index values. At

telophase the highest index value occurred in the control group. In addition, Drought stress+TRIA and alone drought stress had the lowest telophase index values (Figure 1).

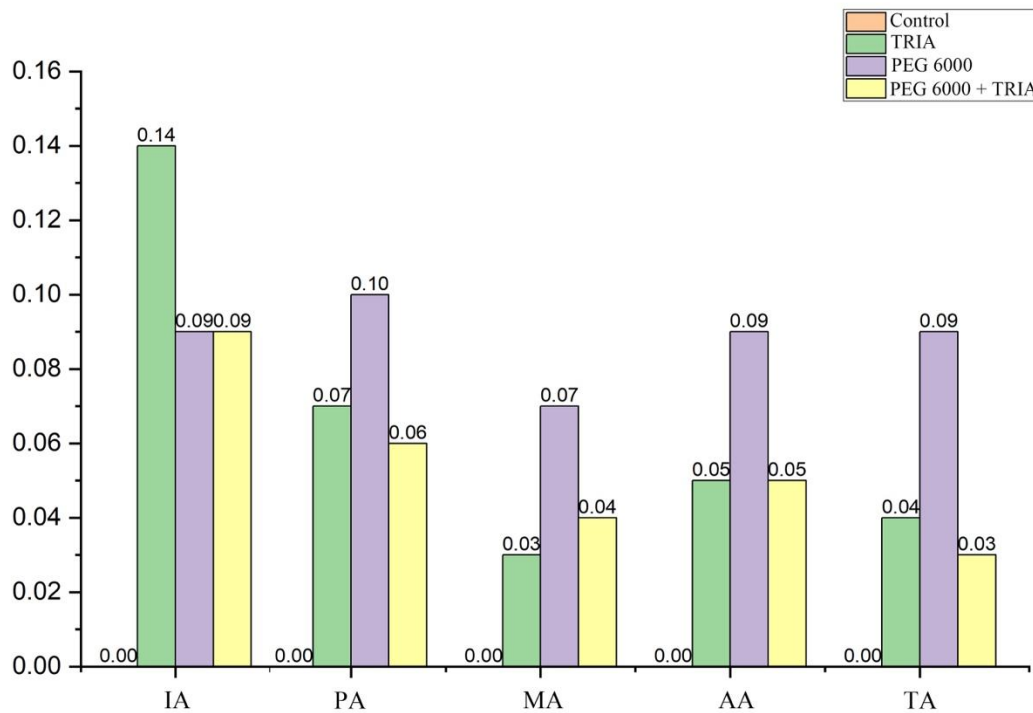


Figure 2. Distribution of chromosome abnormality indices in mitosis stages of exogenous TRIA applied to barley under drought and normal conditions (IA: Interphase abnormalities, PA: Prophase abnormalities, MA: Metaphase abnormalities, AA: Anaphase abnormalities, TA: Telophase abnormalities).

The chromosomal aberration frequencies data obtained from barley root tips germinated both distilled water and drought stress in the absence or presence of 10 μ M TRIA are summarized in Table 2. After alone TRIA application, chromosomal abnormalities frequency was $19.97 \pm 0.46\%$. After the application of drought stress, chromosomal abnormalities increased significantly and an abnormality percentage of approximately 35% was reached. Drought stress+TRIA application significantly reduced chromosomal abnormalities while there was a decrease of approximately 50% compared to alone drought stress, and the chromosomal abnormality frequency decreased to approximately 19%.

After chromosome abnormalities were determined, chromosome abnormality indices at each stage of mitosis were determined by taking into account dividing cells in all the concentrations. Since there are no chromosomal abnormalities in a stress-free environment, control group has the lowest chromosomal abnormality indices value in all phase. According to the results obtained, the application in which prophase, metaphase, anaphase and telophase abnormalities were most observed was the application of alone drought stress. In the interphase, the application with the highest chromosomal abnormality indices value was alone TRIA application (Figure 2).

In this study conducted on the root tips of barley plants to determine chromosome abnormalities, although no chromosome abnormalities were found in any of the seeds germinated in the control group, various chromosome abnormalities were found at samples belonging other concentrations. Microscopic images of a wide range of

chromosome aberrances observed in the preparations prepared with root tips belonging to all other application groups are shown in Figure 3-5.

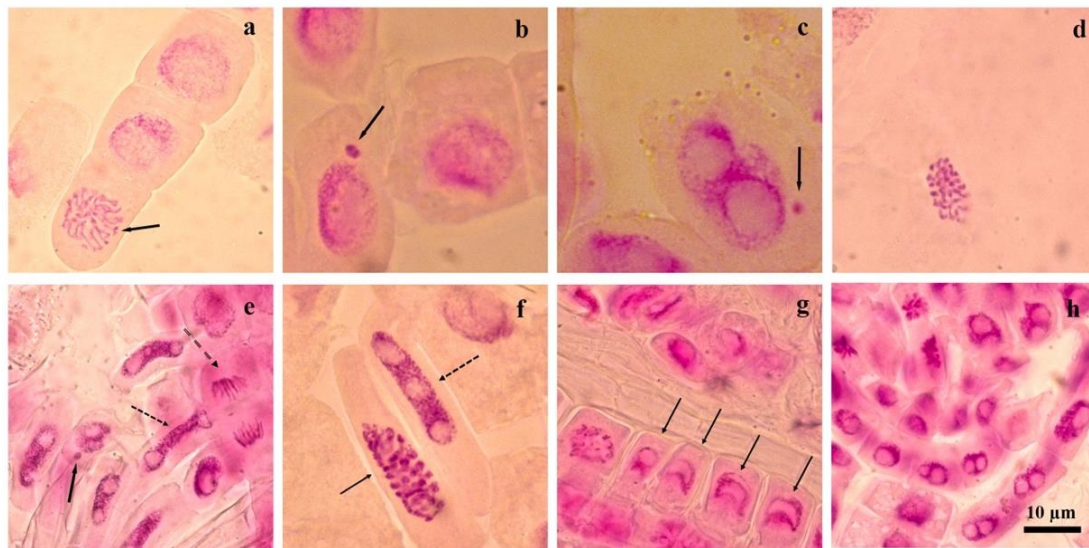


Figure 3. Interphase and prophase stages of exogenous TRIA applied under normal conditions and with drought stress and images of the chromosome abnormalities. a: normal prophase (arrow), b: micronucleus (arrow), c: micronucleus (arrow) in two-vacuolated cell, d: granulation, e: micronucleus (arrow), elongated nucleus with two vacuoles (short spaced arrow), anaphase (long spaced arrow), f: granulation (arrow), elongated nucleus with three vacuoles (striped arrow), g: sickle-shaped nucleus (arrows), h: two-vacuolated cell in interphase.

Chromosomal abnormalities, which occur spontaneously or as a result of the adverse effects of environmental stress, reflect the deleterious effects of a toxic agent on plant cells [37]. The aneugenic and clastogenic effects, which account for a significant proportion of the chromosome abnormalities observed in this study, may be largely due to spindle thread disruption and chromosome breakage, respectively. Micronucleus (MN) assay is agreed to be the most effective endpoint for the analysis of the mutagenic effects of toxic agents. The presence of a large MN in a cell is indicative of an aneugenic effect resulting from chromosome loss. Conversely, the presence of a small MN in a cell is indicative of a clastogenic effect due to chromosome breaks [38]. Briand and Kapoor [39] have indicated that the MNs (Figure 1a, c, e, 2 b, 3b) are a possible consequence of vagrant chromosomes and fragments. It is widely acknowledged by the research that a number of chromatin regulation-related factors, including histone modification enzymes, linker histone H1, HMG proteins and ATP-dependent chromatin remodelling factors, play a role in plant abiotic stress responses [40, 41]. Chromatin granulation observed at interphase (Figure 1d, f) is likely the result of the deformation of the nuclear material caused by toxic agents. This is thought to be a consequence of the aforementioned factors and abnormal chromatin condensation, and indicative of potential abnormalities that may occur in future mitosis phases. Sickle-shaped nucleus and elongated nucleus with vacuoles may have occurred due to absence of NuMA (Nuclear Mitotic Apparatus) in interphase, which is a protein required for the formation of spindle poles in mitosis. Sun et al. [42] and Merdes and Cleveland [43] asserted that the absence of NuMA in interphase nuclei was associated with non-spherical, elongated or beaded nuclear morphology, suggesting that NuMA may act as a non-fundamental nucleoskeletal element during interphase. The formation of sticky chromosomes (Figure 4 e,f) may be attributed to a number of factors, including aberrant DNA condensation, anomalous chromosomal wrapping and the inactivation of the axes [44]. It has also been proposed that such abnormalities may be caused by an incorrect folding of the chromatin fibres

[45]. Some researchers posit that the presence of sticky chromosomes indicates a high degree of toxicity affecting the chromatin, as well as an irreversibility of the change [46, 47]. Chromosome aberrations, such as bridges and breaks, are indicative of a clastogenic action, whereas chromosome losses, laggards, sticky, multipolarity and C-metaphase originate from aneugenic effects [48]. Given that kinetochore attachment is a stochastic process, it is susceptible to errors and can result in chromosome malorientation [49]. Mitodepressive actions, including spiralized chromosomes extending from pole to pole in metaphase, disorderly pro-anaphase, alignment anaphase, ring chromosome in anaphase, multipolar anaphase, bridges and polar slip in ana-telophase, star chromosome in ana-telophase, may be primarily attributable to the aforementioned factors. Furthermore, Tabur and Demir [50] proposed that the nucleoplasmic bridges observed in ana-telophase may have resulted from inversions. Similarly, Bonciu et al. [51] suggested that these bridges may originate from dicentric chromosomes or result from a faulty longitudinal break of sister chromatids during anaphase. Additionally, Fiskesjö [52] posited that bridges are clastogenic effects, resulting from both chromosome and chromatid breaks. Vagrant chromosomes (Figure 5i) and lagging chromosomes (Figure 5m) occur during the anaphase, whereby one or more chromatids become detached from the rest of chromatids and are unable to move towards the poles. Patil and Bhat [53] have put forth the hypothesis that laggard chromosomes may originate from the failure of the spindle apparatus to organize in the typical manner. Also, the laggard of chromosomes may have occurred due to a weak mitotic impress. It is hypothesised that irregular chromosome contractions may result in uncoiling of chromosomes in prophase and metaphase cells. Consequently, it is postulated that TRIA and/or drought stress may have been the cause of the aforementioned abnormalities, due to their ability to stimulate or inhibit enzymes and proteins that are essential for normal cell division, and thereby disrupt the spindle mechanism.

In addition to the substances found in the plant, substances such as hormones and growth regulators given externally can be perceived as stress in plant growth development and toxicity tests. This may result in mitodepressive effects such as inhibition of mitosis or suppression of DNA synthesis, depending on the dose of the substance administered or the duration of application [28]. Thanks to the active properties of the substances exogenously administered to plants, the fact that they cause different levels of clastogenic responses on chromosome structures and behavior varies according to plant species [54]. Researchers have done very little to examine the effects of TRIA on mitotic activity, and this is a major gap in the literature. In one of the rare studies conducted, they stated that TRIA application against the negative effect of salt stress on mitotic activity did not improve mitotic activity, but caused a decrease in chromosome abnormalities [55]. In another study, it was reported that TRIA application under ABA hormone decreased mitotic activity and chromosome abnormalities [56]. This study is the first in the literature to determine the clastogenic effects of exogenous TRIA on especially barley root tip meristems under the effects of drought stress. According to the results of the study, it has been determined that exogenous TRIA application promotes mitotic activity both in a stress-free environment and despite the negative effects of drought stress, and also helps maintain chromosome stability by reducing mutational damage that may occur in DNA or chromatids under drought stress. Although they generally occur as a result of environmental stresses, chromosomal abnormalities may also occur, albeit very rarely, as a result of changes occurring within the plant. This situation occurs especially under the influence of substances that have a toxic effect on plant cells [37]. Along with abiotic factors, biotic toxic agents cause chromosomal abnormalities as a result of aneugenic (changes in the total chromosome number) and clastogenic (changes in chromosome structure) effects. As a result of this study, it has been proven again that drought stress causes various chromosome abnormalities. Considering that chromosome abnormalities

occur as a result of stimulation/inhibition of enzymes and proteins necessary for normal cell division and disruption of the spindle mechanism [57], it is clear that stress has negative effects on these mechanisms. TRIA applied under drought stress showed ameliorative effects on chromosome abnormalities. This means that exogenous TRIA has a stimulating feature on the mechanisms mentioned above.

Table 2. Effects of exogenous TRIA applied on cytogenetic changes in barley under drought stress and normal conditions (*Shows values with insignificant difference ($p < 0.05$) for each column shown with same letters, \pm standard deviation).

Applications	Mitotic index	Chromosome aberrations
Control	*10.20 \pm 0.76 ^b	0.00 \pm 0.00 ^a
10 μ M TRIA	11.04 \pm 0.21 ^{bc}	19.97 \pm 0.46 ^b
%22 PEG 6000	8.18 \pm 0.61 ^a	35.03 \pm 2.32 ^c
%22 PEG 6000 + 10 μ M TRIA	11.85 \pm 0.12 ^c	18.98 \pm 1.25 ^b

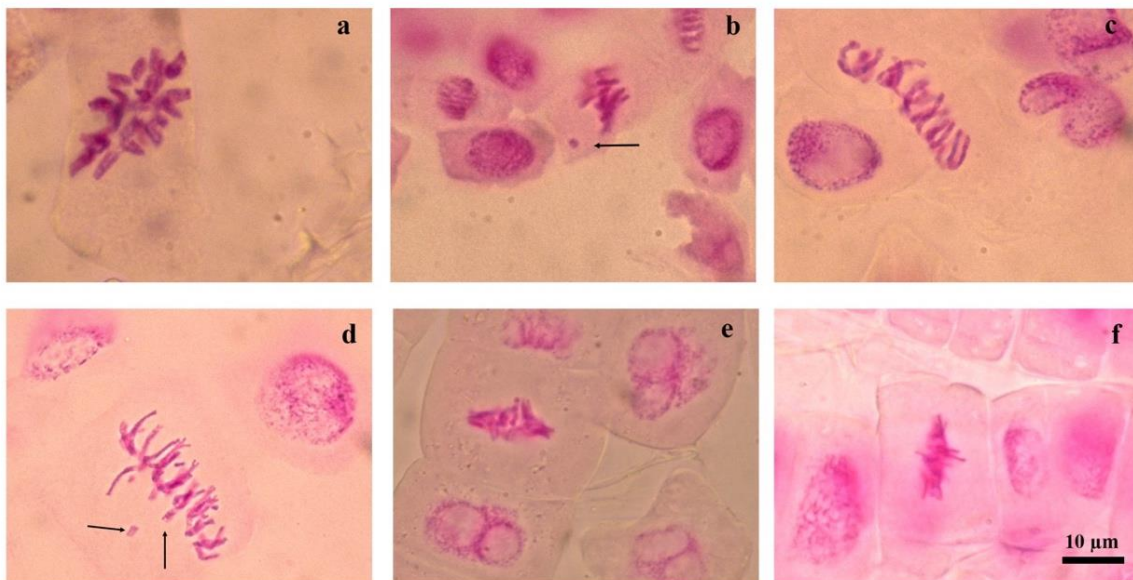


Figure 4. Images chromosomal aberrations of the metaphase stage of exogenous TRIA applied under normal conditions and drought stress. a: normal metaphase, b: micronucleus in metaphase (arrow), c: spiralized chromosomes extending from pole to pole in metaphase, d: fragmented chromosomes (arrows), e and f: sticky chromosomes.

4. Conclusion

As a result of this study, the morphophysiological and cytogenetic effects of exogenous TRIA application on *H. vulgare* cv. Avci, a barley cultivar under both distilled water and drought stress were examined. Drought stress fatally affects plant growth and development, and it is obvious that agricultural areas in almost all parts of the world will be damaged by these negative conditions in the near future. The results clearly show that TRIA application both under drought stress and alone showed encouraging effects on the mitotic index. While TRIA hormone application alone and drought stress caused chromosome abnormalities, TRIA application under stress reduced chromosome abnormalities. This study supports that the pre-application of TRIA given externally in drought conditions can eliminate the negative conditions in the studied parameters. In order to fully reveal the cytogenetic role of TRIA, it is very important and necessary to determine the effects of biosynthetic inhibitors involved in cell division on chromosome

behavior in different plant species. Consequently, investigating the effects of TRIA on basic metabolic events that may directly or indirectly affect cell division and chromosome configuration will be important to form the basis of strategies to combat drought stress.

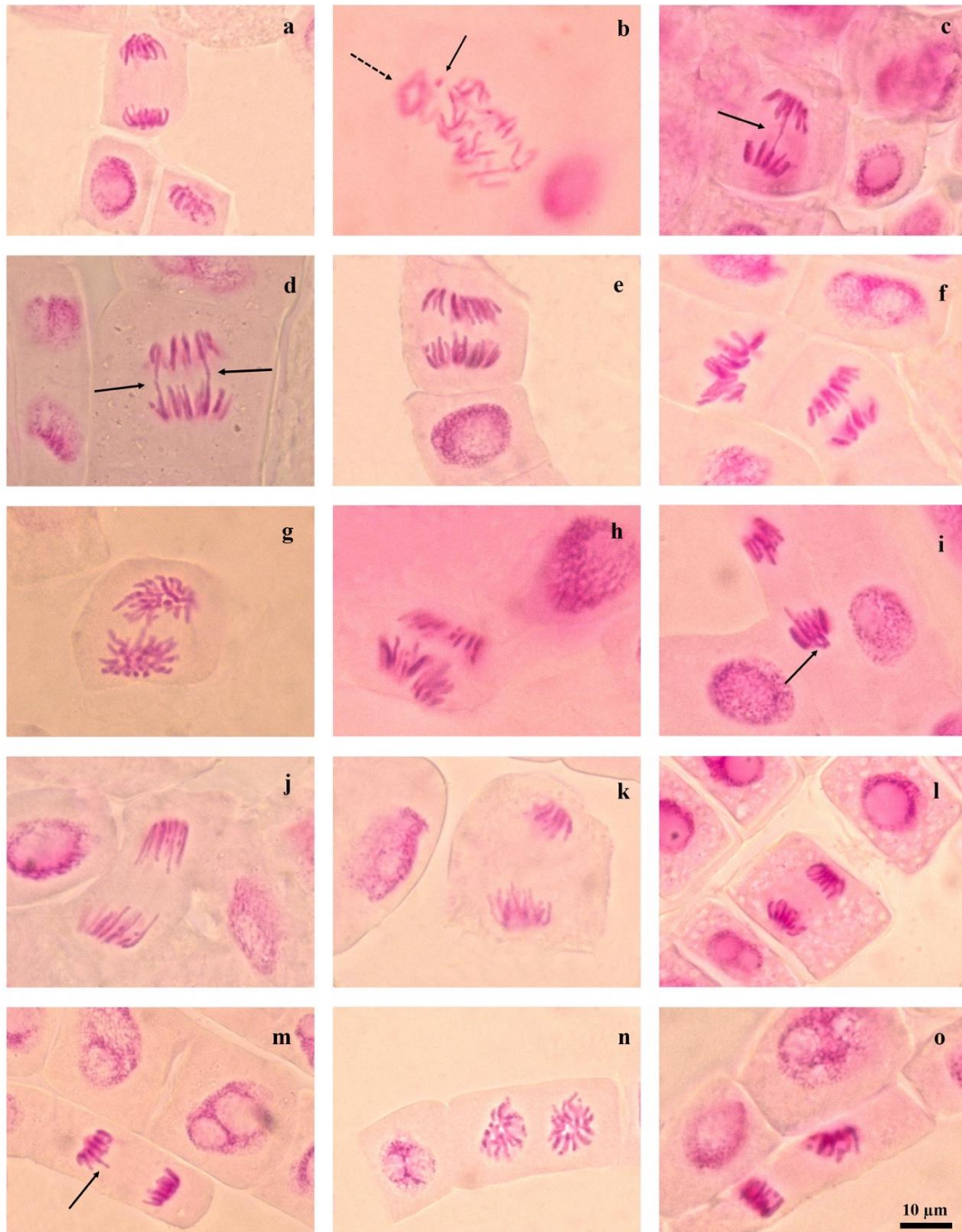


Figure 5. Images of the anaphase and telophase stage of exogenous TRIA applied under normal conditions and drought stress and the chromosome abnormalities. a: normal anaphase, b: micronucleus (arrow), disorderly anaphase and ring chromosome (striped arrow), c: bridge in anaphase (arrow), d: alignment anaphase and double bridge in anaphase (arrows), e and f: alignment anaphase, g: star anaphase, h: multipolar anaphase, i: vagrant chromosome (arrow), j and k: pole slip in anaphase, l: early telophase, m: lagging chromosome. (arrow), n: star telophase, o: pole slip in telophase.

Authorship contribution statement

S. Tabur: Investigation, Original Draft Writing, Review and Editing

S. Özmen: Data Curation, Original Draft Writing; Visualization

A. Yiğit: Assistance in the experimental stages.

Declaration of competing interest

There is no conflict of interest.

Acknowledgment

This study was supported by Suleyman Demirel University Scientific Research Projects with project number FYL-2022-8772. We would like to thank the relevant institution for their support.

Ethics Committee Approval and/or Informed Consent Information

As the authors of this study, we declare that we do not have any ethics committee approval and/or informed consent statement.

References

- [1] K.A.A. Abdelaal, K.A. Attia, S.F. Alamery, M.M. El-Afry, A.I. Ghazy, D.S. Tantawy, A.A. Al-Doss, E.-S.E. El-Shawy, A. M. Abu-Elsaoud and Y.M. Hafez, “Exogenous application of proline and salicylic acid can mitigate the injurious impacts of drought stress on barley plants associated with physiological and histological characters”, *Sustainability*,12(5),1736, 2020.
- [2] M. ALKahtani, Y. Hafez, K. Attia, T. Al-Ateeq, M.A.M. Ali, M. Hasanuzzaman and K. Abdelaal, “*Bacillus thuringiensis* and silicon modulate antioxidant metabolism and improve the physiological traits to confer salt tolerance in lettuce”, *Plants*,10(5),1025, 2021.
- [3] M. Pepe, M.F. Crescente and L. Varone, “Effect of water stress on physiological and morphological leaf traits: A comparison among the three widely-spread invasive alien species *Ailanthus altissima*, *Phytolacca americana*, and *Robinia pseudoacacia*”, *Plants*, 11 (7), 899, 2022.
- [4] M.R. Sofy, A.A. Aboseidah, S.A. Heneidak and H.R. Ahmed, “ACC deaminase containing endophytic bacteria ameliorate salt stress in *Pisum sativum* through reduced oxidative damage and induction of antioxidative defense systems”, *Environmental Science and Pollution Research*, 28, 40971–40991, 2021.
- [5] P. Zandi and E. Schnug, “Reactive oxygen species, antioxidant responses and implications from a microbial modulation perspective”, *Biology*, 11 (2), 155, 2022.
- [6] S. Özmen, S. Tabur, S. Öney-Birol and S. Özmen, “Molecular responses of exogenous polyamines under drought stress in the barley plants”, *Cytologia*, 87 (1), 7–15, 2022.
- [7] S. Ozmen, S. Tabur and S. Oney-Birol, “Alleviation role of exogenous cadaverine on cell cycle, endogenous polyamines amounts and biochemical enzyme changes in barley seedlings under drought stress”, *Scientific Reports*,13 (1), 17488, 2023.
- [8] F. Alghabari and M.Z. Ihsan: “Effects of drought stress on growth, grain filling duration, yield and quality attributes of barley (*Hordeum vulgare* L.)”, *Bangladesh Journal of Botany*, 47 (3), 421–428, 2018.
- [9] N.A. Anjum, S.S. Gill and R. Gill, “Plant Adaptation to Environmental Change: Significance of Amino Acids and their Derivatives”, *CABI*, 2014.
- [10] T.I. Allahverdiyev, J. M. Talai, I.M. Huseynova and J. A. Aliyev, “Effect of drought stress on some physiological parameters, yield, yield components of durum (*Triticum durum* desf.) and bread (*Triticum aestivum* L.) wheat genotypes”, *Ekin Journal of Crop Breeding and Genetics*, 1(1), 50–62, 2015.
- [11] D. Akhzaari and M. Pessaraki “Effect of drought stress on total protein, essential oil content, and physiological traits of *Levisticum officinale* Koch”, *Journal of Plant Nutrition*, 39, 1365–1371, 2016.
- [12] C. Zhang, S. Shi, B. Wang and J. Zhao, “Physiological and biochemical changes in different drought-tolerant alfalfa (*Medicago sativa* L.) varieties under PEG-induced drought stress”, *Acta Physiologia Plantarum*, 40(2), 25, 2018.

- [13] U. Schuppler, P. H. He, P.C.L. John and R. Munns, "Effect of water stress on cell division and Cdc2-Like cell cycle kinase activity in wheat leaves", *Plant Physiology*, 117(2), 667–678, 1998.
- [14] T.L. Setter and B.A. Flannigan, "Water deficit inhibits cell division and expression of transcripts involved in cell proliferation and endoreduplication in maize endosperm", *Journal of Experimental Botany*, 52, 1401–1408, 2001.
- [15] T.S. Per, M.I.R. Khan, N.A. Anjum, A. Masood, S.J. Hussain and N.A. Khan, "Jasmonates in plants under abiotic stresses: Crosstalk with other phytohormones matters", *Environmental and Experimental Botany*, 145, 104–120, 2018.
- [16] P.J. Zwack and A.M. Rashotte, "Interactions between cytokinin signalling and abiotic stress responses", *Journal of Experimental Botany*, 66, 4863–4871, 2015.
- [17] S. Tabur and K. Demir, "Role of some growth regulators on cytogenetic activity of barley under salt stress", *Plant Growth Regulation*, 60(2), 99–104, 2010.
- [18] S.H. Wani, V. Kumar, V. Shriram and S.K. Sah, "Phytohormones and their metabolic engineering for abiotic stress tolerance in crop plants", *The Crop Journal*, 4, 162–176, 2016.
- [19] A. EL Sabagh, M.S. Islam, A. Hossain, M.A. Iqbal, M. Mubeen, M. Waleed, M. Reginato, M. Battaglia, S. Ahmed, A. Rehman, M. Arif, H. U. R. Athar, D. Ratnasekera, S. Danish, M.A. Raza, K. Rajendran, M. Mushtaq, M. Skalicky, M. Brestic, W. Soufan, S. Fahad, S. Pandey, M. Kamran, R. Datta and M.T. Abdelhamid, "Phytohormones as growth regulators during abiotic stress tolerance in plants." *Frontiers in Agronomy*, 4, 765068, 2022.
- [20] T. Verma, S. Bhardwaj, J. Singh, D. Kapoor and R. Prasad, "Triacontanol as a versatile plant growth regulator in overcoming negative effects of salt stress", *Journal of Agriculture and Food Research*, 10, 100351, 2022.
- [21] M.K. Sharma, A. Singh, A. Kumar, S.A. Simnani, N. Nazir, A. Khalil, R. Mushtaq and R. Bhat, "Response of triacontanol on temperate fruit crops a review", *The International Journal of Current Microbiology and Applied Sciences*, 7, 3239–3243, 2018.
- [22] S. Islam, A. Zaid and F. Mohammad, "Role of triacontanol in counteracting the ill effects of salinity in plants: a review", *Journal of Plant Growth Regulation*, 40, 1–10, 2021.
- [23] M. Sarwar, S. Anjum, M.W. Alam, Q. Ali, C.M. Ayyub, M.S. Haider, M.I. Ashraf and W. Mahboob, "Triacontanol regulates morphological traits and enzymatic activities of salinity affected hot pepper plants", *Scientific Reports*, 12, 3736, 2022.
- [24] H. Faiz, O. Khan, I. Ali, T. Hussain, S.T. Haider, T. Siddique, M. Liaquat, A. Noor, R.W. Khan, S. Ashraf, S. Rashid, A. Noreen, S. Asghar and Q.S. Anjum: "Foliar application of triacontanol ameliorates heat stress through regulation of the antioxidant defense system and improves yield of eggplant", *Brazilian Journal of Biology*, 84, e253696, 2022.
- [25] P.E. Verslues, E.S. Ober and R.E. Sharp, "Root growth and oxygen relations at low water potentials. impact of oxygen availability in polyethylene glycol solutions", *Plant Physiology*, 116, 1403–1412, 1998.
- [26] Ş. Elçi and C. Sancak "Research methods and observations in cytogenetics", *Ankara Üniversitesi Publish House*, 227, 2013.
- [27] E. Ivanova, T. Staikova, I. Velcheva and K. Kostadinov, "Somatostatic effect of heavy metal contaminated waters in the region of the town of panagjurishte, Bulgaria" *Journal of Environmental Protection*, 4(2): 284-287, 2003.
- [28] S. Oney-Birol and F. Gunduz, "L- Karnitinin sitotoksik ve genotoksik etkilerinin *Allium cepa* kök ucu testi ile değerlendirilmesi", *Kahramanmaraş Sütçü İmam Üniversitesi Tarım ve Doğa Dergisi*, 22(4): 650-658, 2019.
- [29] M. Zheng, Y. Tao, S. Hussain, Q. Jiang, S. Peng, J. Huang, K. Cui and L. Nie, "Seed priming in dry direct-seeded rice: consequences for emergence, seedling growth and associated metabolic events under drought stress", *Plant Growth Regulation*, 78(2), 167–178, 2016.
- [30] M. Aydin, A. Hossein pour, M. Tosun and K. Haliloglu, "Effect of application of putrescine on seedling growth and cell division of wheat (*Triticum aestivum* L.) under drought stress", *Yuzuncu Yil University Journal of Agricultural Sciences*, 26, 319–332, 2016.
- [31] I.M. Zeid and Z.A. Shedeed, "Response of alfalfa to putrescine treatment under drought stress", *Biologia Plantarum*, 50(4), 635, 2006.
- [32] W.A. Kasim, M.E. Osman, M.N. Omar, I.A. Abd El-Daim, S. Bejai and J. Meijer, "Control of drought stress in wheat using plant-growth-promoting bacteria", *Journal of Plant Growth Regulation*, 32, 122–130, 2013.
- [33] S.K. Thind, "Effects of a long chain aliphatic alcohol mixture on growth and solute accumulation in water stressed wheat seedlings under laboratory conditions", *Plant Growth Regulation*, 10, 223–234, 1991.
- [34] Tilottama, N. Raghava and R.P. Raghava, "Effect of miraculan of seed germination parameters in cowpea under water stress." *Biosciences Biotechnology Research Asia*, 7, 353–358, 2016.
- [35] D. Sanadhya, E. Kathuria and C. Malik, "Effect of drought stress and its interaction with two phytohormones on *Vigna radiata* seed germination and seedling growth", *International Journal of*

- Life Sciences*, 1, 201–207, 2012.
- [36] K. Suman, R. Kondamudi, Y.V. Rao, T.V. Kiran, K.N. Swamy, P.R. Rao, D. Subramanyam and S.R. Voleti, "Effect of triacontanol on rice seed germination, seedling growth and some antioxidant enzyme status under PEG induced drought stress", *The Andhra Agricultural Journal*, 60, 132–137, 2013.
- [37] S. Nag, R. Dutta and K.K. Pal, "Chromosomal aberrations induced by acetamiprid in *Allium cepa* L. root meristem cells", *Indian Journal of Fundamental and Applied Life Sciences*, 3, 1-5, 2013.
- [38] R. Kontek, R. Osiecka and B. Kontek, "Clastogenic and mitodepressive effects of the insecticide dichlorvos on root meristems of *Vicia faba*", *Journal of Applied Genetics*, 48(5), 359-361, 2007.
- [39] C.H. Briand and B.M. Kapoor, "The cytogenetic effects of sodium salicylate on the root meristem cells of *Allium sativum* L.", *Cytologia*, 54, 203–209, 1989.
- [40] J.M. Kim, T.K. To, T. Nishioka and M. Seki, "Chromatin regulation functions in plant abiotic stress responses", *Plant Cell and Environment*, 33, 604–611, 2010.
- [41] M.A. Asensi-Fabado, A. Amtmann and G. Perrella, "Plant responses to abiotic stress: The chromatin context of transcriptional regulation", *Biochimica et Biophysica Acta*, 1860, 106-122, 2017.
- [42] M. Sun, M. Jia, H. Ren, B. Yang, W. Chi, G. Xin, Q. Jiang, and C. Zhang, "NuMA regulates mitotic spindle assembly, structural dynamics and function via phase separation", *Nature Communications*, 12, 7157, 2021.
- [43] A. Merdes and D.W. Cleveland, "The role of NuMA in the interphase nucleus", *Journal of Cell Science*, 111, 71–79, 1998.
- [44] A.O. Asita and M.M. Mokhobo, "Clastogenic and cytotoxic effects of four pesticides used to control insect pests of stored products on root meristems of *Allium cepa*", *Environmental and Natural Resources Research*, 3(2), 133–145, 2013.
- [45] I. Klášterská, A.T. Natarajan and C. Ramel, "An interpretation of the origin of subchromatid aberrations and chromosome stickiness as a category of chromatid aberrations", *Hereditas*, 83, 153-162, 1976.
- [46] G. Fiskesjö and A. Levan, "Evaluation of the first ten MEIC chemicals in the *Allium* test", *Alternatives to Laboratory Animals*, 21, 139–149, 1993.
- [47] S. Türkoğlu "Genotoxicity of five food preservatives tested on root tips of *Allium cepa* L.", *Mutation Research*, 626, 4-14, 2007.
- [48] G.L. Silveira, M.G.F. Lima, G.B. dos Reis, M.J. Palmieri and L.F. Andrade-Vieira, "Toxic effects of environmental pollutants: Comparative investigation using *Allium cepa* L. and *Lactuca sativa* L.", *Chemosphere*, 178, 359-367, 2017.
- [49] A. Banerjee, N. Adames, J. Peccoud and J.J. Tyson, "A stochastic model for error correction of kinetochore-microtubule attachments in budding yeast", *Plos One*, 15(8), e0236293, 2020.
- [50] S. Tabur and K. Demir, "Protective roles of exogenous polyamines on chromosomal aberrations in *Hordeum vulgare* exposed to salinity", *Biologia*, 65, 947-953, 2010.
- [51] E. Bonciu, P. Firbas, C.S. Fontanetti, J. Wusheng, M.C. Karaismailoğlu, D. Liu, F. Menicucci, D.S. Pesnya, A. Popescu, A.V. Romanovsky, S. Schi, J. Ślusarczyk, C.P. Souza, A. Srivastava, A. Sutan and A. Papini, "An evaluation for the standardization of the *Allium cepa* test as cytotoxicity and genotoxicity assay", *Caryologia*, 71(3), 191-209, 2018
- [52] G. Fiskesjö, "Allium test for screening chemicals; evaluation of cytological parameters", In W. Wang, W.R. Lower, J.W. Gorsuch and J.S. Hughes (Eds.), *Plants for Environmental Studies* (pp. 308-333). Lewis Publishers, New York, 1997.
- [53] B.C. Patil and G.I. Bhat, "A comparative study of MH and EMS in the induction of chromosomal aberrations on lateral root meristem in *Clitoria ternatea* L.", *Cytologia*, 57, 259–264, 1992.
- [54] D.M. Leme and M.A. Marin-Morales, "Allium cepa test in environmental monitoring: A review on its application", *Mutation Research/Reviews in Mutation Research*, 682, 71–81, 2009.
- [55] S. Tabur and K. Demir, "Tuz stresi altındaki mitotik indeks ve kromozom anormallikleri üzerine triakontanol ön uygulamasının etkileri", *Research Journal of Biological Sciences*. 1, 11–15, 2008.
- [56] S. Tabur and N. Öney, "Comparison of cytogenetic antagonism between abscisic acid and plant growth regulators", *Pakistan Journal of Botany*, 44, 1581-1586, 2012.
- [57] S. Tabur, N.B. Bayraktar, and S. Özmen, "L-Ascorbic acid modulates the cytotoxic and genotoxic effects of salinity in barley meristem cells by regulating mitotic activity and chromosomal aberrations", *Caryologia*, 75(3), 19–29, 2022.

Energy Loss and Range Calculations for Alpha Particles in B-100 Bone and C-552 Air-Equivalent Plastic Materials

Metin Usta^{1,*}

¹Department of Physics, Faculty of Arts and Sciences, Hatay Mustafa Kemal University, 31034, Hatay, TURKEY

<http://orcid.org/0000-0002-7896-397X>

*corresponding author: musta@mku.edu.tr

(Received: 27.07.2024, Accepted: 07.11.2024, Published: 25.11.2024)

Abstract: The type of radiation that harms humans and living organisms is the ionizing type. In this type of radiation, radiation passing through the cell transfers energy to biological tissues and causes harmful biological effects along with chemical changes. Therefore, radiation exposure doses should be kept as low as possible and appropriate shielding materials should be used between radiation and living tissue. In this study, stopping power and range calculations of B-100 bone and C-552 air-equivalent plastic materials, which are International Commission on Radiation Units & Measurement (ICRU) materials, were performed for alpha particles in the energy range of 0.1 MeV - 10 MeV. The effective charge approach within the scope of Bethe-Bloch theory and Bohr stripping criterion was used in collision stopping power calculations. The Continuous Slowing-Down Approximation (CSDA) method and the 3/8 Simpson approximation were chosen for range calculations. The error rates were found to be less than 10% when the results were compared with the available literature data.

Key words: Stopping power, CSDA range, Radiation, Alpha particles, Phantom

1. Introduction

Radiation can be divided into two groups: ionizing and non-ionizing. The type of radiation that harms humans and living organisms is the ionizing type. Ionizing radiation has cumulative effects on living organisms, especially humans, throughout their lives and increases the risk of developing cancer. In this type of radiation, radiation passing through the cell transfers energy to biological tissues and causes harmful biological effects along with chemical changes. Therefore, doses to be exposed to radiation should be kept as low as possible and appropriate shielding materials should be used between radiation and living tissue. In this respect, the energy loss (stopping power) per path taken by the charged particles in the target and the path they take (range) are significant in the interaction of radiation with matter [1].

In radiotherapy, dose accumulation and the interaction of radiation with target tissues must be understood before the patient is exposed to radiation. These interactions and dose accumulations can be investigated using phantom materials equivalent to the target of interest. Therefore, the study presented here is aimed at examining the interaction of radiation with bones and air. Although some studies have been carried out on bone and air-equivalent plastic materials so far, stopping power and range calculations of these targets have not been made for alpha particles other than ICRU [2] and the Stopping and Range of Ions in Matter (SRIM) [3].

SRIM is a group of programs that quantum mechanically describes atom and ion collisions and can perform stopping power, range and straggling calculations up to 2 GeV energy. These calculations use a statistical algorithm that consider bulk electronic

excitations and bond structures between atoms. The ICRU 49 report contains tables of electronic, nuclear and total stopping power, CSDA range and deflection factors for 73 target materials for protons and alpha particles with energies between 1 keV and 1 GeV. Collision stopping powers at low energies (about 0.5 MeV for protons and below 2 MeV for alpha particles) are based on experimental data, while at energies higher than these energies they are based on Bethe stopping power theory, including quasi-empirical average excitation energies, shell corrections and the 1st Born approximation. SRIM program and ICRU report data are internationally valid and globally accepted reference databases on the interaction of radiation with matter.

In this study, stopping power and range calculations were made analytically for B-100 bone and C-552 air-equivalent plastic materials, which are ICRU materials, for alpha particles in the 0.1 MeV-10 MeV energy range. Effective charge approach within the scope of Bethe-Bloch theory and Bohr stripping criterion was used in collision stopping power calculations. Sapporo QZP functions [4] from Gaussian basis sets were preferred for the electronic potential energy functions of the targets. The CSDA method and the 3/8 Simpson approximation were chosen for range calculations. When the results obtained were compared with the available literature data, it was determined that the error rates were less than 10%. Therefore, stopping power and CSDA range calculations were performed with an innovative approach by using a new electronic potential energy function, taking into account the effective charge, stripping distance and effective average excitation energy of these targets.

2. Material and Method

2.1. Target materials

The materials selected in this study were B-100 bone-equivalent plastic (ICRU card 112) and C-552 air-equivalent plastic (ICRU card 116) targets, which are generally used in radiotherapy and are ICRU materials. The atomic number fraction by weight, average excitation energies (I), and densities (ρ) of the materials are given in Table 1.

Table 1. Density, composition, and mean excitation energy of B-100 and C-552 materials

Materials	Atomic number fraction by weight							I (eV)	ρ (g/cm ³)
	H	C	N	O	F	Si	Ca		
B-100*	0.065	0.536	0.021	0.032	0.167		0.176	85.971	1.452
C-552*	0.024	0.501		0.004	0.465	0.003		86.863	1.765

* ICRU 49

2.2. Stopping power calculations

In this study, collision stopping power and CSDA range calculations were made for alpha particles in the energy range of 0.1 MeV-10 MeV in bone and water equivalent materials. As it is known, stopping power calculations of heavy charged particles consist of collision and nuclear parts. However, the contribution from the nuclear stopping power calculation to the total stopping power is negligible in the energy range of interest. Therefore, only the contributions from collision stopping power were considered here.

Collision stopping power calculations were performed within the framework of the effective charge approach [5], which includes the first Born approximation and takes into

account the Bethe-Bloch theory [6]. Accordingly, the energy loss per unit length when alpha particles with velocity v arrive at the target is given by

$$S_{coll}(v) = \frac{4\pi e^4}{m_e c^2 \beta^2} Z_1^2 Z_2^* \ln\left(\frac{q_{max}}{q_{min}}\right) \quad (1)$$

Where, e is the elementary charge, m_e is the mass of the electron, c is the speed of light, $\beta = v/c$, Z_2^* is the effective charge of the target, q_{max} and q_{min} are momentum transfers. The effective charge and momentum transfers of the target can be found from the following relation:

$$Z_2^* = \int_{r_s}^{\infty} 4\pi r^2 \rho(r) dr \quad (2)$$

$$q_{max} = \frac{2m_e v}{\hbar}, \quad q_{min} = \frac{2I^*}{\hbar v} \quad (3)$$

Here $\rho(r)$ is the electron density of the target material, r is the distance from the nucleus, r_s is the stripping distance, and I^* is the effective mean excitation energy of target material.

$$\ln I^* = \frac{1}{Z_2^*} \int_{r_s}^{\infty} \ln[\gamma \hbar \omega_p(r)] 4\pi r^2 \rho(r) dr \quad (4)$$

ω_p is the plasma frequency, and γ is the a constant that can be set to $\sqrt{2}$. The electronic potential energy function

$$U(r_s) = [-\pi \rho(r) r^4] / 5 + C \quad (5)$$

obtained from the solution of Poisson's equation and the Bohr stripping criterion [7] expression were used [8]. and C is a constant. In this study, the charge density of the target materials was calculated using the expression

$$\rho(r) = \sum_{\mu} |u_{\mu}(\mathbf{r})|^2 \quad (6)$$

2.3. Gaussian basis sets

Sapporo QZP functions [9] from Gaussian basis sets were preferred to calculate the electronic charge density. This function, which consists of radial and angular parts, is as follows:

$$g(r, \theta, \phi) = N(l, \alpha) r^l e^{-\alpha r^2} Y_{l,m}(\theta, \phi) \quad (7)$$

Where l is angular momentum quantum number, $Y_{l,m}$, is spherical harmonics, α , is exponential coefficient, and $N(l, \alpha)$ is the normalization constant and is given as follows:

$$N(l, \alpha) = \frac{2(2\alpha_{n,l})^{3/4}}{\pi^{1/4}} \sqrt{\frac{2^l}{(2l+1)!!}} (2\alpha_{n,l})^l \quad (8)$$

Here, atomic orbitals are considered to be spherical ($l = 0$) and spin interactions are ignored.

2.4. CSDA range calculations

The range calculations of alpha particles were based on the continuous slowing down approximation (CSDA), which describes the path taken by these particles as they lose energy until they continuously slow down and run out of energy:

$$R = \rho_t \int_{E_i}^{E_f} \frac{dE}{S_{coll}} \quad (9)$$

Here ρ_t is the density of the target, E_i and E_f are the initial and final energies of the alpha particles, respectively. Since this integral is very difficult to calculate analytically for range calculations, the more convenient Simpson 3/8 method, known as the four-point approximation, was used:

$$\int_{E_i}^{E_f} \frac{dE}{S_{coll}} \cong \frac{3}{8} \Delta E \left[\frac{1}{S_{coll}}(E_i) + \frac{1}{S_{coll}}(E_f) + 3 \sum_{\substack{j=1 \\ 1,2,4,5}}^{n-1} \frac{1}{S_{coll}}(E_i + j \cdot \Delta E) + 2 \sum_{\substack{j=3 \\ 3,6,9}}^{n-3} \frac{1}{S_{coll}}(E_i + j \cdot \Delta E) \right] \quad (10)$$

3. Results and Discussion

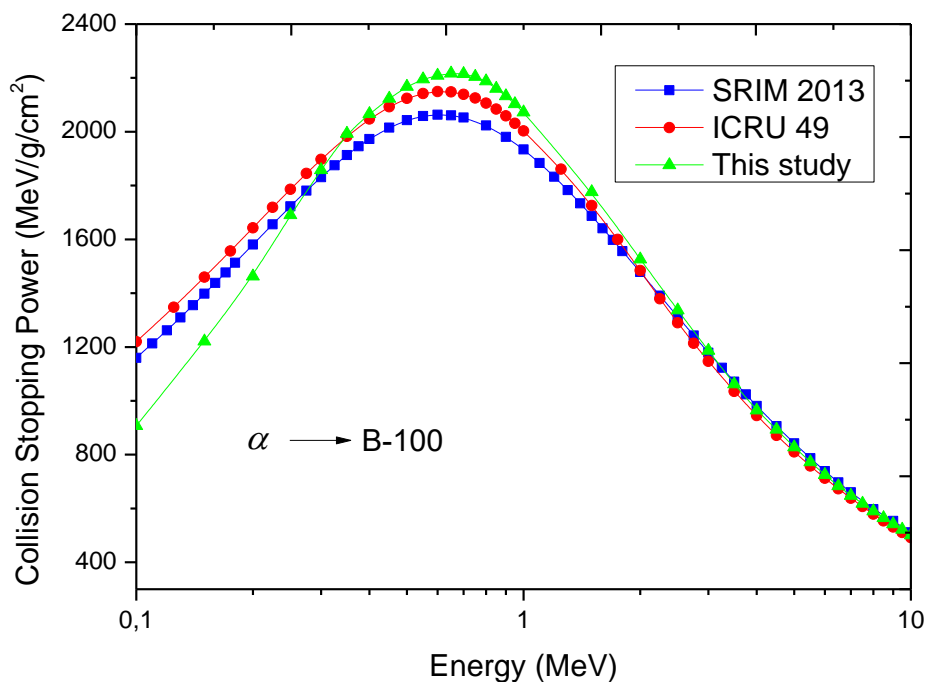


Figure 1. The collision stopping power results of B-100 bone-equivalent plastic material for alpha particles

Figure 1 shows the collision stopping power results of B-100 bone-equivalent plastic material for alpha particles with 0.1-10 MeV energy. It is understood that the values approach each other at energies of 2 MeV and above, but there are significant differences at energies lower than 2 MeV. It is particularly noteworthy that the calculated values suddenly decrease at low energies. The peaks of the curves are localized in the 600-700 keV interval, and the peak values obtained here differ from the available data. The error rates of the calculated stopping power values with the ICRU data are 2.25% in the 2-10 MeV energy range and 2.74% in the 0.1-2 MeV energy range.

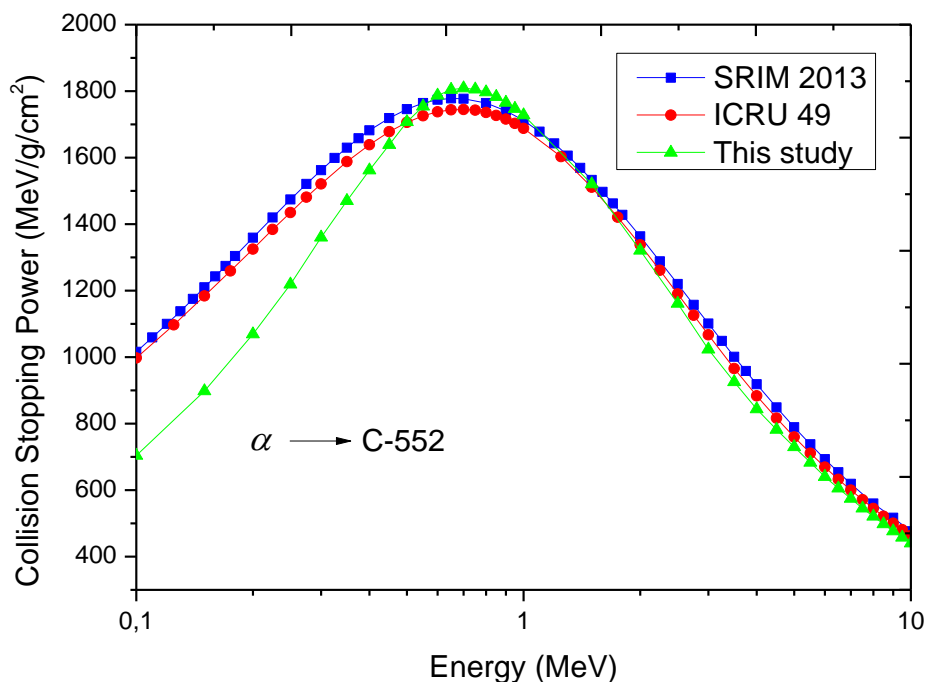


Figure 2. The collision stopping power values of the C-552 air equivalent plastic material for alpha particles

Figure 2 indicates the collision stopping power values of the C-552 air-equivalent plastic material for alpha particles in the energy range from 0.1 MeV to 10 MeV. At energies of about 1.5 MeV and above, the values are close to each other, but at energies lower than 1.5 MeV there are differences in the data. In particular, the stopping power values obtained in this study differ significantly from the existing values. The values are localized in the range of 650 keV-700 keV, with the peaks of the data being at 650 keV for SRIM and 700 keV for ICRU and this study. The error rates of the collision stopping power values calculated here with the ICRU data are 3.48% for alphas with 2-10 MeV energies and 4.08% for alphas with 0.1-2 MeV energies.

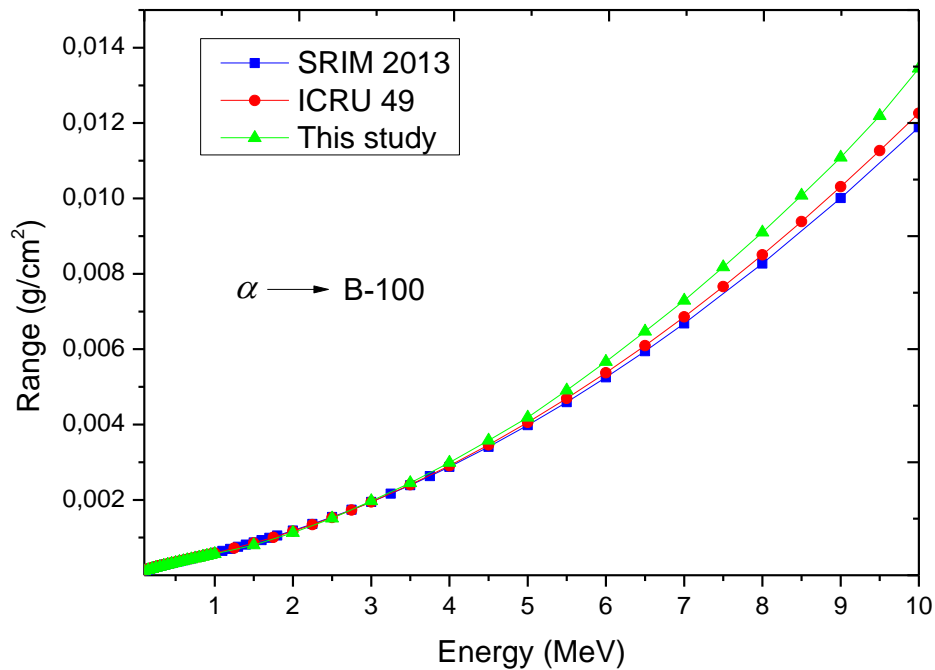


Figure 3. The CSDA range of alpha particles in B-100 bone-equivalent plastic material.

Figure 3 represents the CSDA range of alpha particles with energies of 0.1-10 MeV in B-100 bone-equivalent plastic material. The figure displays that the range values increase with the energy of the alpha particles. The envelope of the curves generally depicts the shape of a parabola. Although the SRIM values are quite close to the ICRU data, there are significant differences in the values obtained in this study. These differences become more noticeable with increasing energies, especially from 4 MeV onwards. The error rates of the CSDA range values calculated in this study with the ICRU data are 5.40% in the 0.1-2 MeV energy range, while they are at 5.14% in the 2-10 MeV energy range.

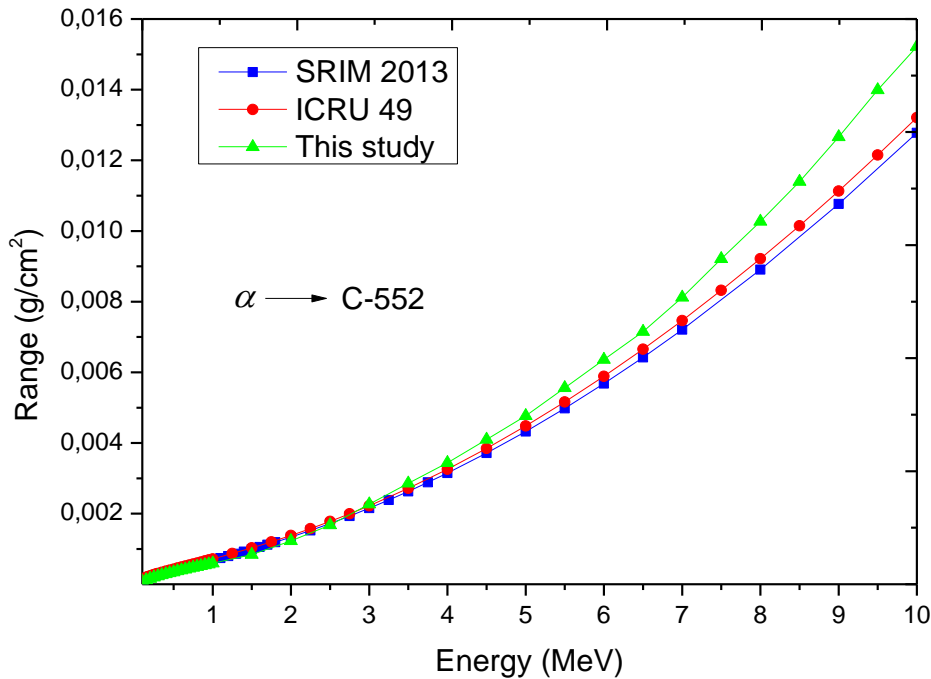


Figure 4. The CSDA range of alpha particles in C-552 air-equivalent plastic material.

Figure 4 demonstrates the CSDA range values in the C-552 air-equivalent plastic target of alpha particles with energies of 0.1-10 MeV. As expected, the range values increase proportionally with the energy of the incoming alpha particles. The amount of increase is non-linear and more in line with a parabolic curve. Again, SRIM values and ICRU data are close to each other, and the values calculated here show significant changes. The error rates of the calculated CSDA range values with the ICRU data are 6.12% in the 0.1-2 MeV range, while they are around 5.86% in the 2-10 MeV range.

In this study, collision stopping power and, indirectly, range calculations were performed using the effective charge approach within the Bethe-Bloch framework. In this approach, the 1st Born approximation is used for high-speed charged particles. So, the speeds of the incoming charged particles are greater than the orbital speeds of the electrons in the target atom. Thus, the Bohr stripping criterion and the potential energy function including the electronic charge density of the target were used to calculate the excitation cross section.

CSDA range calculations were based on the 3/8 Simpson rule. This rule approximates the function of interest, the inverse stopping power function, by a parabola, hence a 3rd-order polynomial. This further reduces the probability of error. Error rates of 5-6% in range calculations are due to the use of higher-order polynomials to connect the points and thus more accurate integral calculations. Although this method gives more accurate results than the Trapezoidal method, it would be useful to apply different integration methods such as Gaussian quadrature and Romberg method to the calculations and compare the results.

So far, many studies have been conducted using the effective charge approximation [5, 8, 10-14]. In these studies, parameters such as the atomic charge, average excitation energy, and stripping distance of different target materials were used at their effective values. In the present study, a new electronic potential energy function with the effective values of the target materials of interest was constructed and calculations based on these functions

were performed. Therefore, due to these effective parameters, this method outperforms the SRIM data at energies above 2 MeV because it does not require Bloch, Barkas and shell corrections. However, the high error rates at energies lower than 2 MeV are due to the fact that the 1st Born approximation is not valid at low energies. Because additional events such as electron capture occur at these energy levels. In this region, the distorted wave Born approximation or the Coulomb wave Born approximation should be used instead of the plane wave Born approximation.

4. Conclusion

In this work, collision stopping power and CSDA range data of bone and air-equivalent plastic materials were calculated for alpha particles. Both stopping power and range values were found to be more consistent with literature data at energies above 2 MeV. In general, when averaged, it was observed that the values obtained were compatible with the ICRU data with an error rate of less than 10%. These predicted values based on the study showed good agreement with the stopping power and range values of alpha particle in SRIM code and ICRU. The data calculated in this study will provide important contributions to studies involving the interaction of radiation with matter.

Authorship contribution statement

M. Usta: Data Curation, Original Draft Writing, Visualization.

Declaration of competing interest

The authors declare that they have no known competing financial interests or personal relationships that could have appeared to influence the work reported in this paper.

Ethics Committee Approval and/or Informed Consent Information

As the authors of this study, we declare that we do not have any ethics committee approval and/or informed consent statement.

References

- [1] J. Man, Y. Shen, Y. Song, K. Yang, P. Pei and L. Hu, "Biomaterials-mediated radiation-induced diseases treatment and radiation protection", *Journal of Controlled Release*, 370, 318-338, 2024.
- [2] ICRU, *Stopping Powers and Ranges for Protons and Alpha Particles*, in *ICRU Report 49*, 1993.
- [3] J. F. Ziegler, J. P. Biersack and M. D. Ziegler, *SRIM, the Stopping and Range of Ions in Matter*. 2013: SRIM Company.
- [4] T. Koga, S. Yamamoto, T. Shimazaki and H. Tatewaki, "Contracted Gaussian-type basis functions revisited. IV. Atoms Rb to Xe", *Theoretical Chemistry Accounts*, 108(1), 41-45, 2002.
- [5] M. Usta, M. Ç. Tufan, G. Aydın and A. Bozkurt, "Stopping power and dose calculations with analytical and Monte Carlo methods for protons and prompt gamma range verification", *Nuclear Instruments and Methods in Physics Research Section A: Accelerators, Spectrometers, Detectors and Associated Equipment*, 897, 106-113, 2018.
- [6] H. Bethe, "Zur theorie des durchgangs schneller korpuskularstrahlen durch materie", *Annalen der Physik*, 397(3), 325-400, 1930.
- [7] N. Bohr, "Scattering and stopping of fission fragments", *Physical Review*, 58(7), 654-655, 1940.
- [8] M. Usta, "The calculation of stopping power and range for radium, thorium and uranium using new electronic potential energy function", *Applied Radiation and Isotopes*, 152, 193-199, 2019.
- [9] R. Weber, B. Hovda, G. Schoendorff and A. K. Wilson, "Behavior of the Sapporo-nZP-2012 basis set family", *Chemical Physics Letters*, 637, 120-126, 2015.
- [10] R. Cabrera-Trujillo, S. A. Cruz, J. Oddershede and J. R. Sabin, "Bethe theory of stopping incorporating electronic excitations of partially stripped projectiles", *Physical Review A*, 55(4), 2864-2872, 1997.
- [11] M. C. Tufan, A. Koroglu and H. Gumus, "Stopping power calculations for partially stripped projectiles in high energy region", *Acta Physica Polonica A*, 107(3), 459-472, 2005.

-
- [12] M. Ç. Tufan, Ö. Kabadayı and H. Gümüş, “Stopping power calculations of molecules for swift projectiles”, *Radiation Physics and Chemistry*, 76(3), 631-635, 2007.
- [13] M. Usta and M. Ç. Tufan, “Stopping power and range calculations in human tissues by using the Hartree-Fock-Roothaan wave functions”, *Radiation Physics and Chemistry*, 140(Supplement C), 43-50, 2017.
- [14] M. Usta, “Continuous slowing-down approximation ranges of biological materials for 0.05–10 MeV alpha particles by using different approach methods”, *Applied Radiation and Isotopes*, 178, 109951, 2021.